FOR FURTHER TRAN ~~DT~~ - 1

ADsE300723

DNA 4404F-1

AD A055885

TITANIUM RESPONSE TO SIMULATED NUCLEAR CLOUD PARTICLE ENVIRONMENTS

Volume I—Analytical and Experimental Results

Science Applications, Inc.

101 Continental Blvd.

El Segundo, California 90245

②
85

31 August 1977

Final Report for Period September 1976—August 1977

CONTRACT No. DNA 001-76-C-0366

AU No.
DDC FILE COPY

Prepared for

Director

DEFENSE NUCLEAR AGENCY

Washington, D. C. 20305

D D C
RECEIVED
JUL 5 1978
B

Destroy this report when it is no longer needed. Do not return to sender.

UNCLASSIFIED

SECURITY CLASSIFICATION OF THIS PAGE (When Data Entered)

(19) REPORT DOCUMENTATION PAGE	READ INSTRUCTIONS BEFORE COMPLETING FORM

1. REPORT NUMBER	2. GOVT ACCESSION NO.	3. RECIPIENT'S CATALOG NUMBER
DNA 4404F-1, AD-E300 223		

4. TITLE (and Subtitle)

TITANIUM RESPONSE TO SIMULATED NUCLEAR CLOUD PARTICLE ENVIRONMENTS.
Volume I. Analytical and Experimental Results

VOL. II. AD55888

5. TYPE OF REPORT & PERIOD COVERED

Final Report, No Period
Sep 76—Aug 77

6. PERFORMING ORG. REPORT NUMBER

SAI-78-561-LA—VOL-1

7. AUTHOR(s)

L. E. Dunbar   G. H. Burghart
R. M. Clever   A. F. Mills

8. CONTRACT OR GRANT NUMBER(s)

DNA 001-76-C-0366

9. PERFORMING ORGANIZATION NAME AND ADDRESS

Science Applications, Inc.   62704H
101 Continental Blvd.
El Segundo, California 90245

10. PROGRAM ELEMENT, PROJECT, TASK AREA & WORK UNIT NUMBERS

NWED Subtask
N99QAXAA129-42

11. CONTROLLING OFFICE NAME AND ADDRESS

Director
Defense Nuclear Agency
Washington, D.C. 20305

12. REPORT DATE

31 August 1977

13. NUMBER OF PAGES

154

14. MONITORING AGENCY NAME & ADDRESS(if different from Controlling Office)

(10) Lyle/Dunbar, Richard M.
Clever, G.H./Burghart A.F./Mills

15. SECURITY CLASS (of this report)

UNCLASSIFIED

15a. DECLASSIFICATION/DOWNGRADING SCHEDULE

16. DISTRIBUTION STATEMENT (of this Report)

Approved for public release; distribution unlimited.

(12) 151 p.

17. DISTRIBUTION STATEMENT (of the abstract entered in Block 20, if different from Report)

18. SUPPLEMENTARY NOTES

This work sponsored by the Defense Nuclear Agency under
RDT&E RMSS Code B342077464 N99QAXAA12942 H2590D.

19. KEY WORDS (Continue on reverse side if necessary and identify by block number)

Titanium   Erosion
Nuclear Cloud   Heat Transfer
Oxidation

20. ABSTRACT (Continue on reverse side if necessary and identify by block number)

The response of titanium alloy (6Al-4V) to simulated nuclear
cloud particle environments is addressed in this combined experi-
mental and analytical study. The results are applicable for
ascent vehicles with hot titanium structures flying through
nuclear burst ice or dust clouds. A three-phase exploratory
program was conducted: An initial oxidation test series using
an SAI-designed test fixture, a test series using the AEDC Dust — (over)

DD FORM 1473 1 JAN 73   EDITION OF 1 NOV 65 IS OBSOLETE

UNCLASSIFIED

SECURITY CLASSIFICATION OF THIS PAGE (When Data Entered)

20.   ABSTRACT (Continued)

Erosion Tunnel (DET), and a particle impact test series using
the SAI hypervelocity impact facility. Analytical modeling
of titanium oxidation produced results in close agreement with
experiment. Although increased oxidation of titanium was con-
firmed in H_2O vapor versus O_2 environment tests, no net effect
of liquid H_2O and O_2 oxidation under combined particle erosion
conditions was observed in the AEDC DET. This is believed to be
the result of the heat of vaporization of H_2O exceeding the heat
of oxidation of H_2O vapor.

PREFACE

This final report documents the work completed by Science Applications, Inc. (SAI), under DNA contract DNA001-76-C-0366. This work was sponsored by the Aerospace Systems Division of the Shock Physics Directorate of the Defense Nuclear Agency. The program was conducted during the period September 1976 through August 1977. The DNA technical monitor was Major Don Anderson. The SAI Principal Investigator was Mr. Lyle Dunbar who also directed the AEDC Dust Erosion Tunnel testing. The oxidation and impact tests were performed in the SAI Electro-optics and Impact Laboratory at Santa Ana, California under the direction of Mr. George Burghart. Analytical modeling was performed by Dr. Richard Clever and SAI consultant Dr. A. F. Mills.

1

TABLE OF CONTENTS

LIST OF FIGURES

LIST OF FIGURES (CONTINUED)

LIST OF FIGURES (CONTINUED)

7

LIST OF TABLES

NOMENCLATURE

Symbol	Definition

Alphabetical

A	reaction rate constant
B	constant
C	oxygen concentration
C_s	oxygen concentration
D	diffusion coefficient
d_p	particle diameter
E	reaction activation energy
H_r	recovery enthalpy
ΔH_s	heat of reaction
K	oxygen consumption
$\dot{m}_{O_z}$	mass flux of oxygen
M_{O_z}	total oxygen
Q_{cw}	cold wall convection
Q_{vap}	rate at which heat is absorbed
$\dot{q}_{react}$	rate of chemical heat release
R	gas constant
t	time
V	velocity

Symbol	Definition
Greek	
γ	constant in parabolic oxidation model
ε	oxide scale thickness
ζ	titanium thickness
η	fraction of particle energy transferred
ρ	material specific gravity
ρ_p	particle specific gravity
ρ_{cl}	cloud density
τ	obscuration time
χ	material depth
α	ratio of projected crater surface area to particle cross-sectional area
α_H	depth of kinetic energy deposition
ΔW	titanium oxidation weight gain

1.0   INTRODUCTION AND SUMMARY

Extensive testing and analyses (1-5)* have been
conducted to develop a response model (erosion and heating)
for titanium subjected to dust impacts. This model has been
successful in a broad range of ground test facilities in
predicting titanium response. However, consideration has
not been given to the combined effects of nuclear cloud
ice/water particle and dust particle impacts on titanium.
In general, dust particle impacts would be expected to be an
over-simulation of ice impacts and thus, a design to a dust
environment of equivalent mass concentration would be con-
servative. However, there remains some uncertainty relative
to the effect of ice/water impacts on titanium surface
chemistry heating augmentation. This document describes a
combined analytical and experimental program to bound the
effects of ice/water on titanium surface chemical reaction
heating augmentation and to develop an improved heat transfer
model to describe these effects, if necessary, for design
applications.

1.1   Technical Background

Extensive studies of titanium oxidation have shown
the dominant surface chemistry heating augmentation mech-
anism to be the result of the formation of solid state
oxides (3, 4). Oxygen available at the surface of the
titanium diffuses through a protective oxide coating and
releases energy in the form of a heat of solution. As the
temperature of the titanium or the oxygen concentration
increases, the oxygen diffuses faster and energy is released
at an increased rate. Titanium ignition occurs when the
heat released due to the chemical reaction exceeds the heat
losses due to convection, conduction, and radiation. Titanium
nosetips must be designed to stay well below this ignition

---

* Refers to reference numbers in Section 6.0.

temperature threshold. Particle impacts complicate the oxidation/heat release process since they remove the protective oxide coating and increase the temperature locally, thus increasing the local rate of oxygen diffusion and chemical heat release. Figure 1-1 describes this process schematically.

Past studies (4) have produced models for the chemical heat release in titanium. Figure 1-2 shows schematically that the rate of oxygen diffusion into titanium (and thus rate of chemical heat release $\dot{q}_{react}$) is controlled by the mass flux of oxygen at the surface $(\dot{m}_{O_2})_{gas}$ (in the boundary layer flow field) and by the rate of oxygen diffusion in the solid titanium $(\dot{m}_{O_2})_{solid}$. The dominating rate process is a function of the time between impacts τ (obscuration time). The chemical reaction heat release can be written:

$$\dot{q}_{react} = 2 \left[\left(\dot{m}_{O_2} \right)_{solid} \right]_{t=\tau} \left[1 - \left(\frac{1}{2} \right) \frac{\left[\left(\dot{m}_{O_2} \right)_{solid} \right]_{t=\tau}}{\left(\dot{m}_{O_2} \right)_{gas}} \right] \Delta H_s$$

where ΔH_s is the heat of solution. For typical dust cloud conditions, the process is dominated by solid phase diffusion (this must be reexamined for nuclear ice cloud conditions). The oxygen diffusion into the solid can be written:

$$\left(\dot{m}_{O_2} \right)_{solid} = C_s \sqrt{\frac{A \exp (-E/RT)}{\pi t}}$$

where A and E are constants related to diffusion of oxygen in titanium, T is the titanium temperature, t is the time, and C_s is the oxygen concentration at the surface. Combining the above expressions yields the functional form
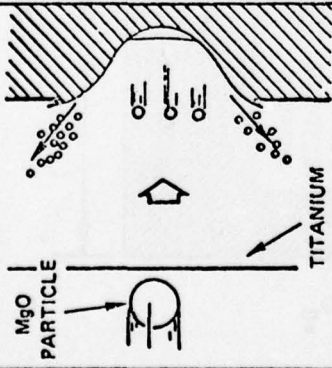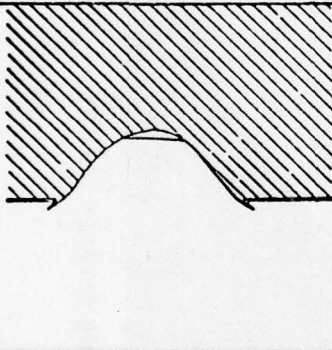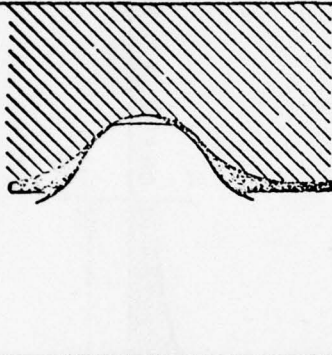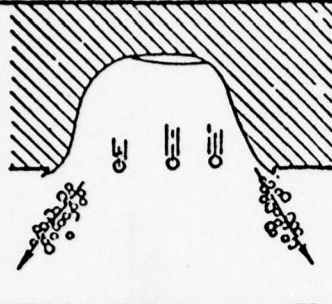
EVENT	PARTICLE IMPACT AND ENERGY PARTITIONING	TRANSIENT OXIDATION AND SCALE FORMATION	DIFFUSION THROUGH SCALE	NEXT PARTICLE IMPACT
SCHEMATIC	MgO PARTICLE / TITANIUM			
PROCESSES OCCURRING	• PARTICLE BREAKUP • KINETIC → POTENTIAL ENERGY TRANSFER • CRATER FORMATION/ EJECTION OF TARGET MATERIAL AND PARTICLE DEBRIS • DEPOSITION OF PARTICLE "SLAG"	• DIFFUSION OF O_2 THROUGH CRATER WALLS WITH HEAT RELEASE • RADIATIVE/CONDUCTIVE COOLING OF CRATER WALLS • BUILDUP OF O_2 CONCENTRATION IN SOLID TO SATURATED SOLUTION	• REDUCED O_2 DIFFUSION RATES • CONTINUED WALL COOLING • POTENTIAL CHANGE IN Ti-O CRYSTAL STRUCTURE	• REPEAT OF INITIAL IMPACT • TARGET EJECTA CONSISTS OF "SCALE" AND "VIRGIN" Ti
ELAPSED TIME	(0) 1 μ SEC	(0) 1 MSEC	(0) 1/3 SEC	

FIGURE 1-1. SCHEMATIC OF TITANIUM SURFACE REACTION PROCESS
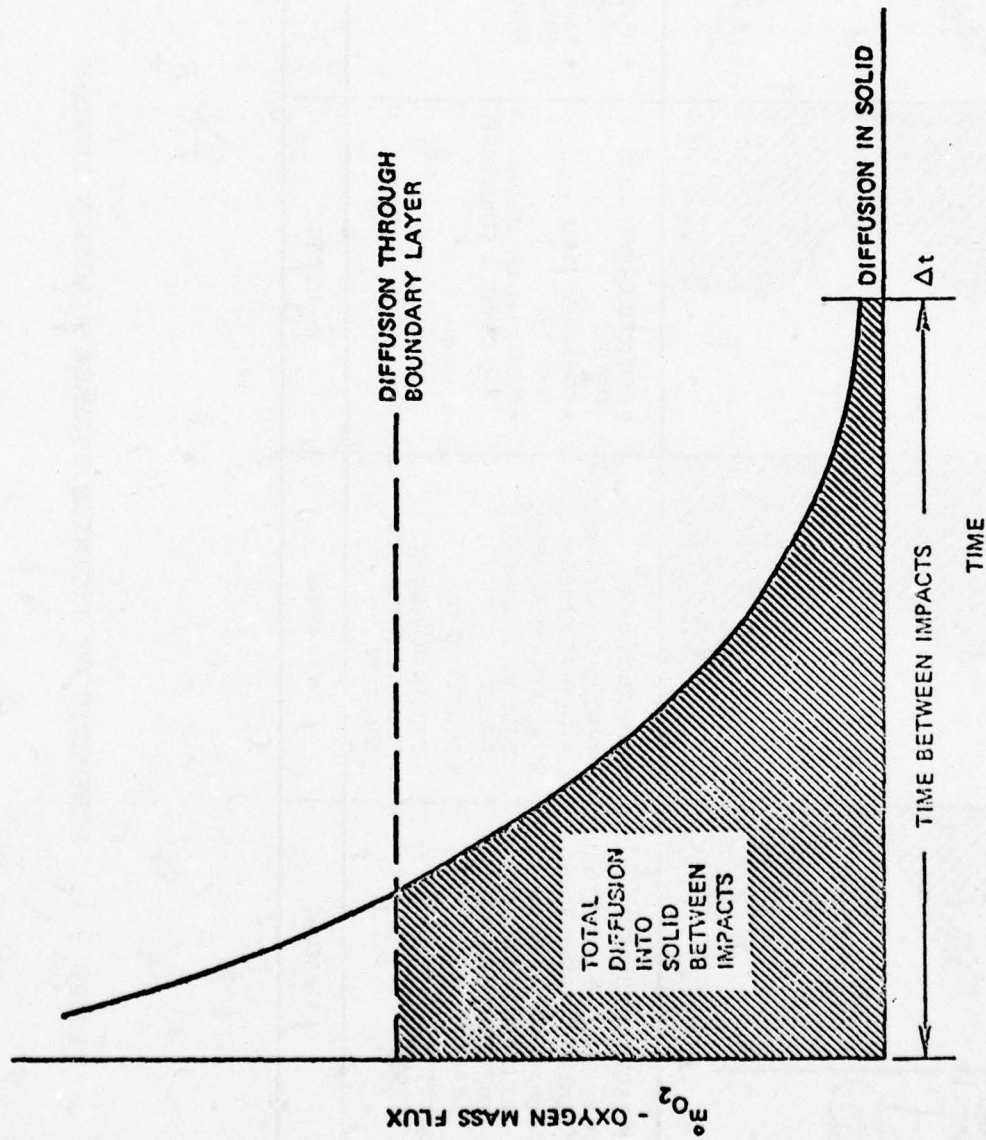
FIGURE 1-2. SCHEMATIC OF CONSTRAINTS ON OXYGEN MASS FLUX INTO SOLID TITANIUM

$$\dot{q}_{react} \sim C_s \Delta H_s \frac{1}{\sqrt{\tau}} \exp(-B/T)$$

where B is a constant and $\tau = \frac{2}{3} \frac{\rho_p d_p}{\rho_{CL} V \alpha}$ where α is the ratio of projected crater surface area to particle cross-sectional area (order of 1), ρ_p is the particle density, d_p is the diameter, V is velocity and ρ_{CL} is the cloud concentration. This model is generally applicable for impacts of any particle type for oxygen diffusion into titanium from any oxygen source. The constants in the above relation must be determined for specific cases. For dust impacts on titanium in air environments, a suitable empirical relation was derived to be

$$\dot{q}_{react} = 47700 \frac{1}{\sqrt{\tau}} \exp(-23085/T(°R)) \; Btu/ft^2\text{-sec}$$

where T is assumed to be the local titanium surface temperature. A comparison of past AEDC DET data (4) with this model, shown in Figure 1-3, shows excellent agreement. The more generalized model for dust particle-titanium chemistry coupling provides a framework for considering the additional effects of ice impacts on titanium surface chemistry.

There are several unique differences between ice and dust impact conditions which could alter the titanium surface chemistry heating augmentation. Specific parameters affected include τ (particle density, diameter and cloud density differences); T (different kinetic energy transfer and thus local crater temperature on impact); C_s (available concentration of oxygen in the boundary layer at the titanium surface); B (activation energy) and the rate constant for diffusion of water species into titanium.
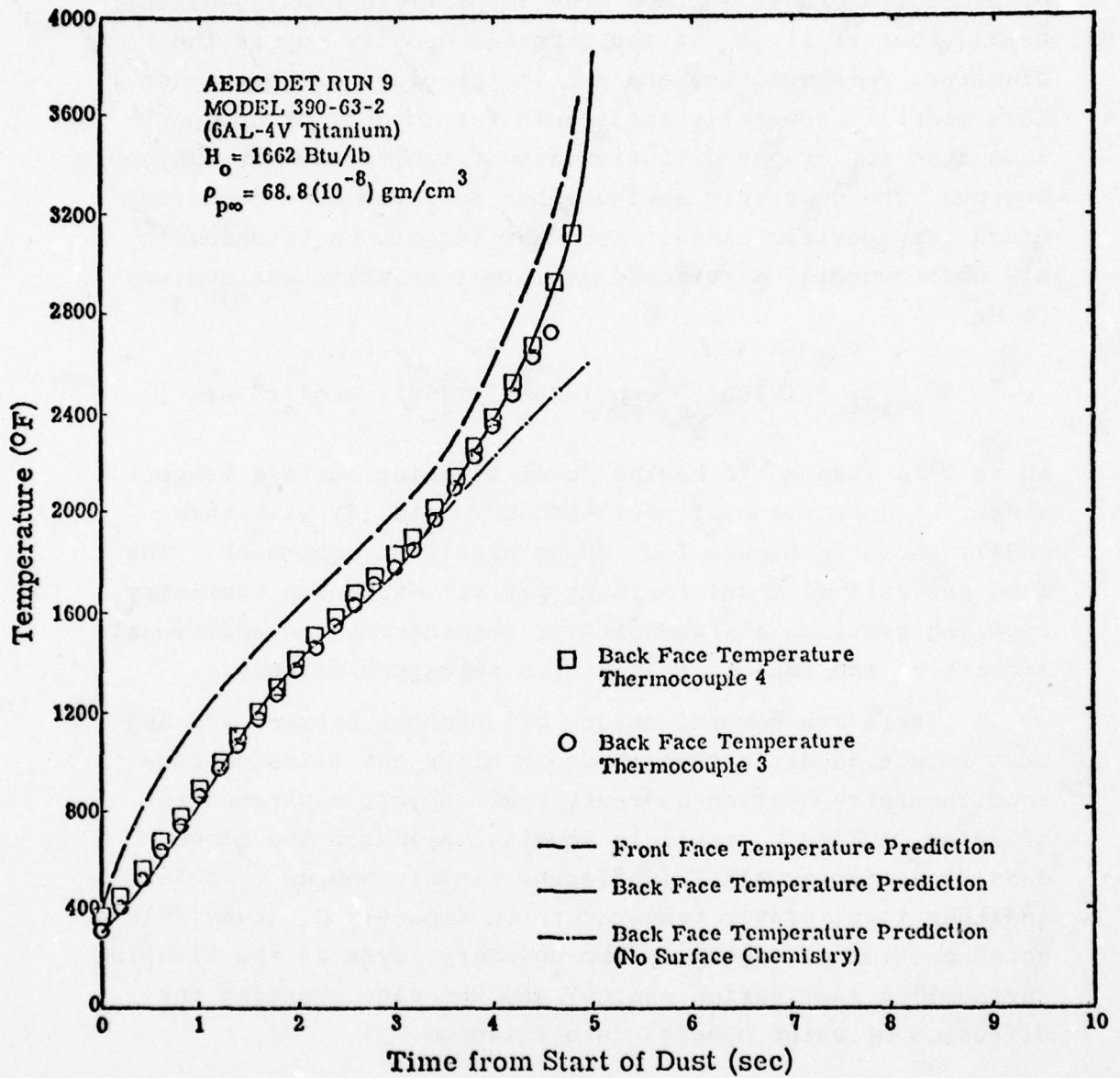
FIGURE 1-3. APPLICATION OF THE HEATING AUGMENTATION MODEL FOR
AEDC DET RUN 9 (FROM REFERENCE 4)

The objective in this program was to obtain oxidation and impact test data for titanium at elevated temperatures in oxidizing environments to determine if the presence of ice or water significantly altered the response characteristics of titanium under dust impact conditions which were successfully modeled in previous studies. Test facilities selected were as follows:

1. SAI Oxidation Test Facility
2. SAI Ice Impact Test Facility
3. AEDC Dust Erosion Tunnel

No facility currently exists which can simulate multiple ice erosion on titanium in an oxidizing environment for time periods greater than a few milliseconds in order to evaluate chemistry effects. The above facilities simulate critical elements of the nuclear cloud ice/water and dust environment for evaluating a missile titanium component response. In addition to the test program, an improved analytical model was formulated for titanium oxidation based on data in the literature including limited data on the effect of steam oxidation of titanium. This model was used to analyze test data and evaluate the combined effects of ice/water and dust particle environments on titanium.

1.2   Summary of Results

The results of this exploratory program show no significant overall degradation in titanium performance for combined ice/water and dust environments versus dust environments. Previous studies of titanium response to dust showed surface chemical reactions becoming important at temperatures in excess of 2000°F and eventually causing ignition at higher temperatures. This temperature of 2000°F remains a valid criteria for ice/water and dust below which

surface chemistry effects are unimportant. Ignition
is _not_ expected where the bulk temperature of the
titanium is always below 2000°F.

Specific results from this program contributing to
the above general conclusion include:

1. Titanium Oxidation Results

The SAI Phase I tests of titanium in non-erosive
oxidizing environments (H_2O vapor and O_2) showed an apparent
increase in oxidation rate in H_2O vapor compared to O_2 for
temperatures of 1200-1500°K. At the 1700°K condition, this
trend was not evident with O_2 and H_2O vapor giving similar
oxidation rates. Figure 1-4 shows a comparison of the Phase
I experimental results with the oxidation model derived from
the literature. The nominal model suggests a parabolic-type
weight gain law ($\Delta W/\sqrt{t}$) where ΔW is the total weight gain
and t is the total test time. The bulk of the test data
(both H_2O vapor and O_2) fall within the $\pm$ factor of 2 un-
certainty band for the O_2 oxidation model based on data in
the literature. The exception is the 1.0 atm data at 1400°K
where a pressure effect is suggested. This was unexpected
based on a solid-phase diffusion-controlled model and sug-
gests the possibility that the SAI oxidation tests may have
been gas-phase rate-limited although this was not confirmed
during the testing. Although the H_2O vapor data from this
program falls within the uncertainty band of the total
experimental data base for O_2 oxidation data from the litera-
ture, the current H_2O vapor data does indicate a general
increase in oxidation compared to the current O_2 data up to
the 1700°K condition.
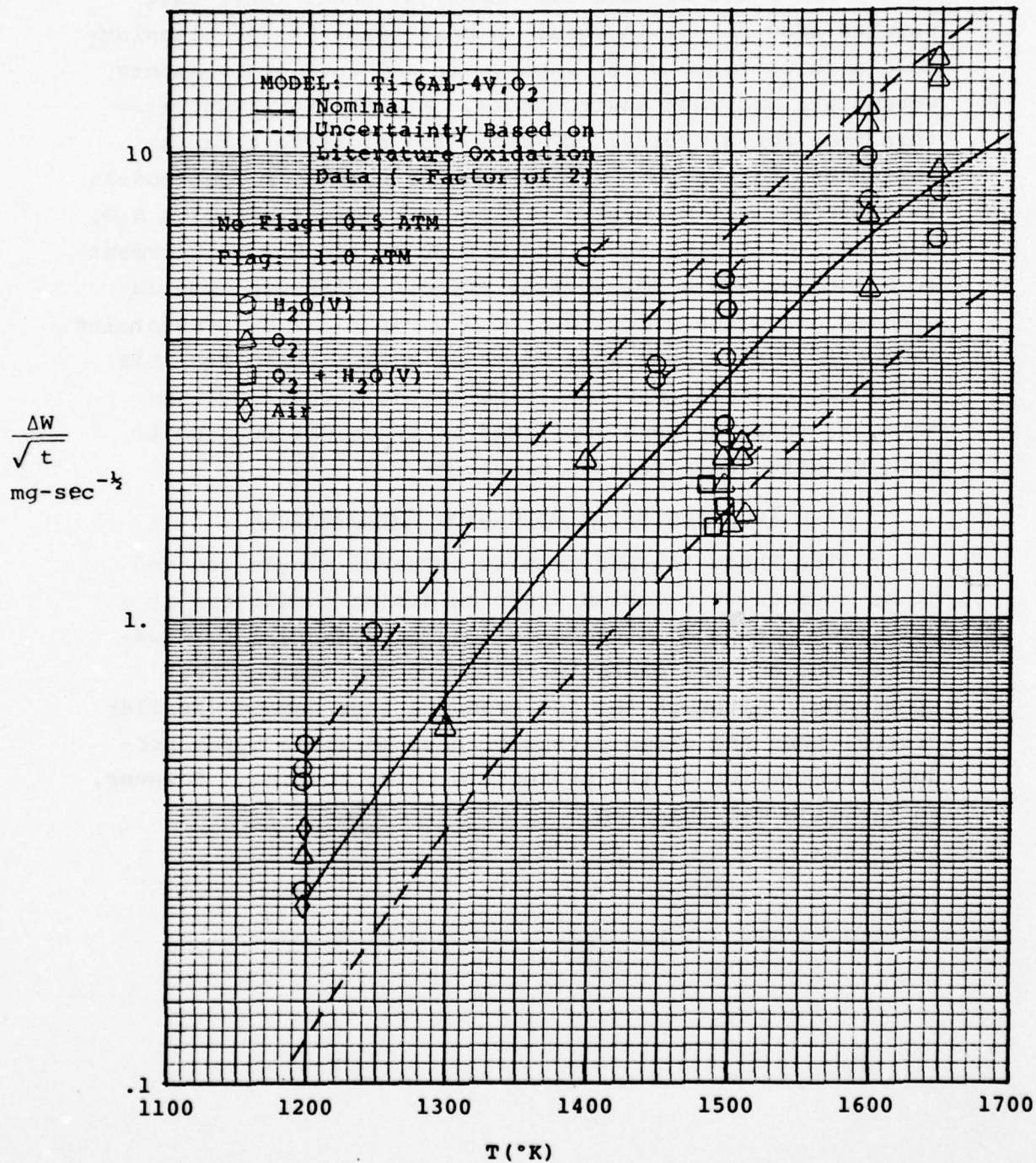
FIGURE 1-4. COMPARISON OF EXPERIMENTAL AND ANALYTICAL
TITANIUM OXIDATION RESULTS

2. Combined Erosion and Oxidation

The Phase II AEDC Dust Erosion Tunnel (DET) test results show no <u>net</u> increase in heat transfer for titanium models in combined water vapor, air and dust environments versus air and dust environments. Figure 1-5 illustrates this fact for a typical DET run. The backface titanium hemisphere temperature versus time is shown for four models in different environments -- clear air, clear air plus H_2O, dust, and dust plus H_2O. The effect of the H_2O environment in all cases was a <u>net</u> cooling effect. Although some increased oxidation effect due to H_2O vapor may be present (as indicated above), the heat of vaporization dominates this oxidation heat release resulting in the overall cooling effect. This has been confirmed in other DET runs up to bulk titanium temperatures of 2500°F.

3. Ice Impacts in Oxidizing Environments

The Phase III SAI results compared single ice and glass impacts on titanium under oxidizing conditions at a bulk temperature of ∿1700°F (∿1200°F). Figure 1-6 illustrates the surface characteristics of two typical test specimens. Although the ice produced less damage (smaller crater) than the glass particle, both particle types produced spallation of the protective oxide coating. However, <u>no</u> ignition was observed.
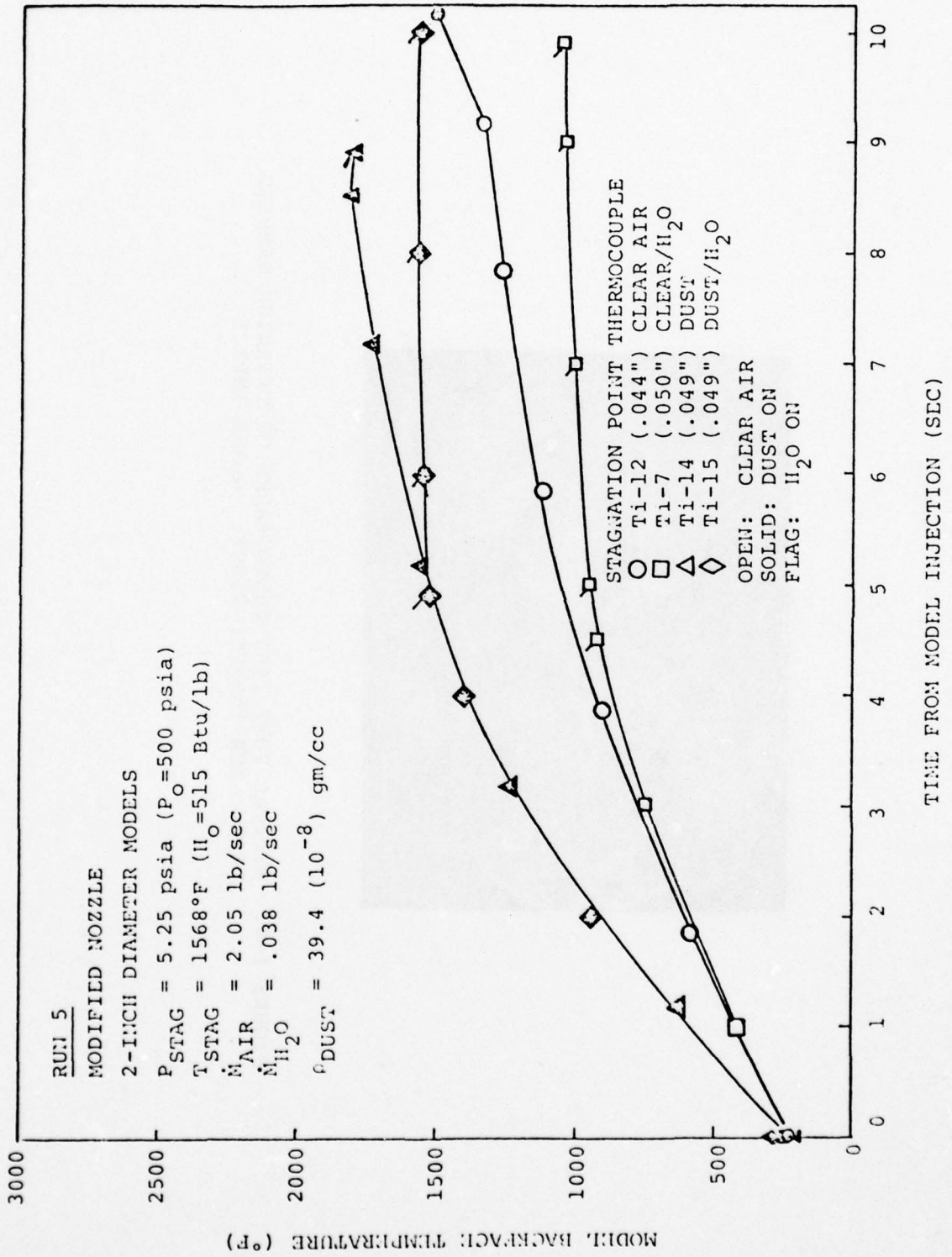
FIGURE 1-5.   RESULTS FROM AEDC DET RUN 5

1-11
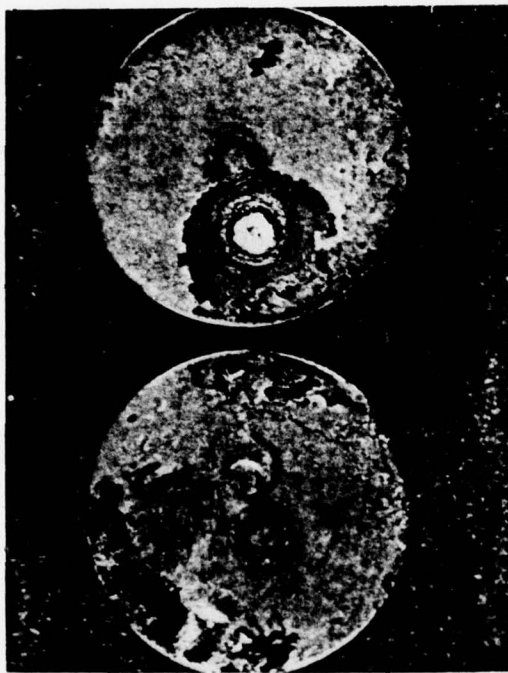
FIGURE 1-6. TYPICAL POST TEST PHOTOGRAPHS OF TITANIUM SAMPLES
LEFT: ICE IMPACT, RIGHT: GLASS IMPACT

2.0   SAI OXIDATION AND IMPACT TEST SERIES

2.1   Test Objectives and Scope

The objectives of the Phase I oxidation tests were to evaluate the effect of water vapor and pressure on the oxidation characteristics of titanium (6AL-4V) at elevated temperatures. The scope of Phase I included three test series with a total of 36 tests using the oxidation test fixture at the SAI Santa Ana, California laboratory.

The objective of the Phase III impact tests was to evaluate titanium response to ice and glass impacts in oxidizing environments to determine if ignition occurs from single impacts. The scope of Phase III included six tests in the SAI impact facility at Santa Ana, California on 6AL-4V titanium at elevated temperature comparing glass and ice impact results.

2.2   Oxidation Test Program

The Phase I oxidation tests were conducted at the SAI Santa Ana, California laboratory in a test rig especially designed for this DNA program. The test rig is shown in Figure 2-1. The test specimen (see Figure 2-2) is suspended by thermocouple wires welded to the specimen in a vicor cylinder. An induction coil attached to the 25KW induction heater surrounds the vicor tube. The environment (O_2, air, argon, H_2O vapor, or mixtures) is controlled by admitting the respective gases to the test chamber via a control panel equipped with solenoid on-off valves and manually operated flow regulating valves.

The insitu instrumentation consisted of type E and type S thermocouples and an optical pyrometer to measure specimen temperature history. Pre-test and post-test weight measurements of the test sample and its thermocouple were performed to determine oxidation weight gain.

THERMOCOUPLE LEADS

FLOW METER

INDUCTION COIL

VICOR CYLINDER
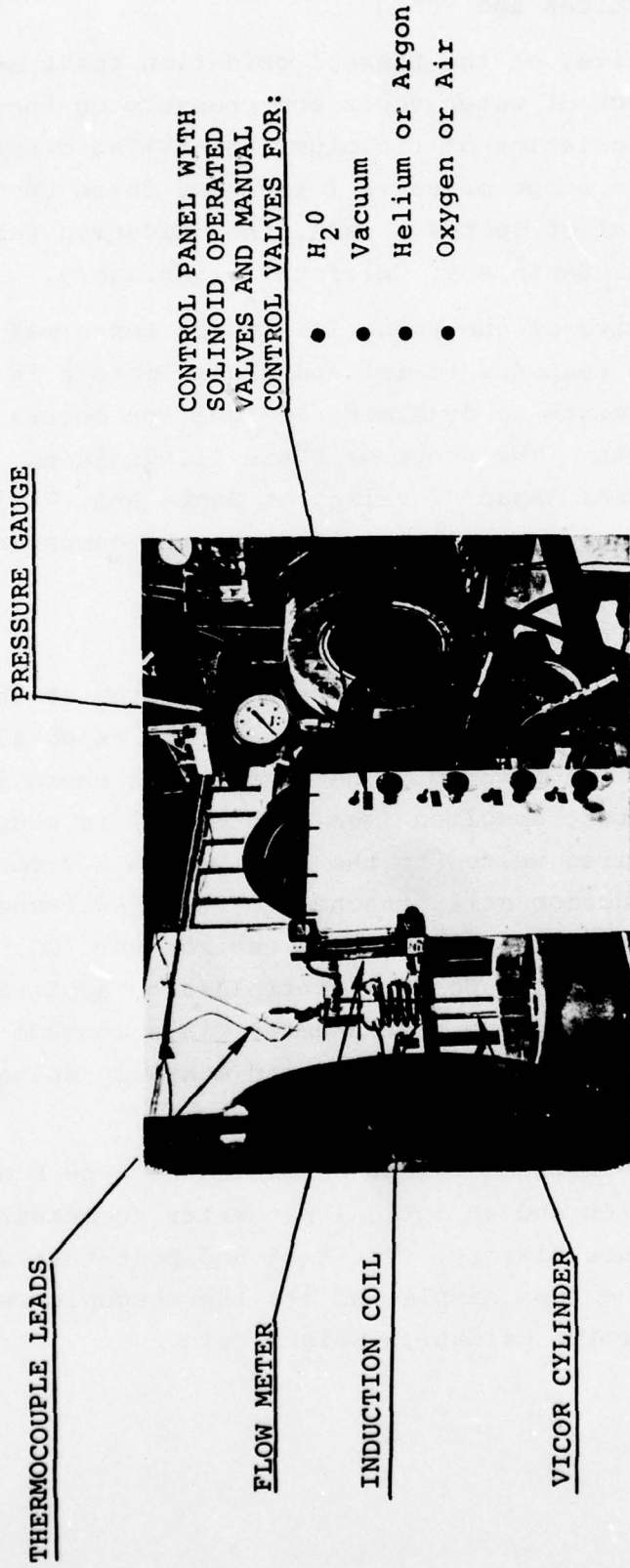
PRESSURE GAUGE

CONTROL PANEL WITH
SOLINOID OPERATED
VALVES AND MANUAL
CONTROL VALVES FOR:

- H_2O
- Vacuum
- Helium or Argon
- Oxygen or Air

FIGURE 2-1a. OXIDATION TEST STAND - FRONT VIEW

VICOR CYLINDER
IN INDUCTION COIL

THERMOCOUPLE
LEADS

BACKSIDE OF CONTROL
PANEL SHOWING VALVES
AND PLUMBING

OPTICAL
PYROMETER

WATER BATH
FOR COOLING EXHAUST
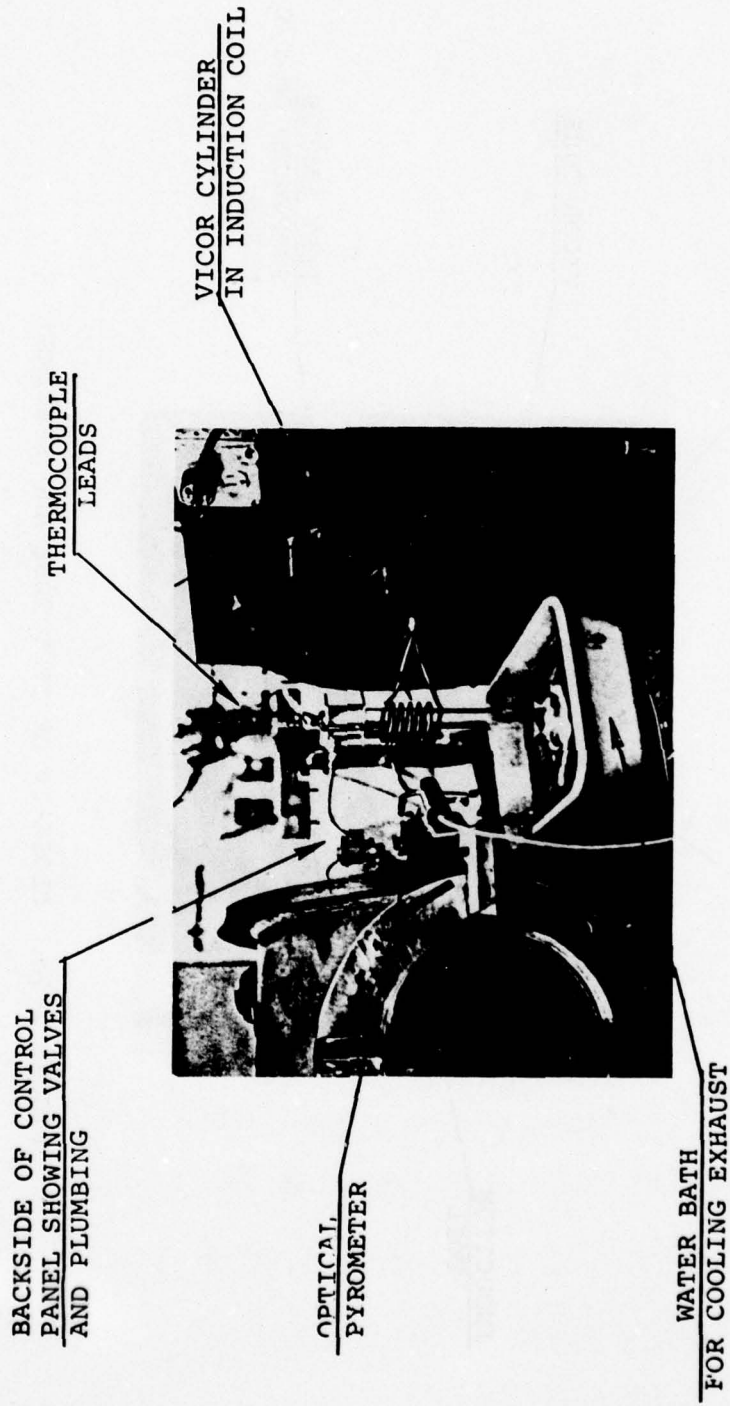
FIGURE 2-1b. OXIDATION TEST STAND - REAR VIEW

2-3
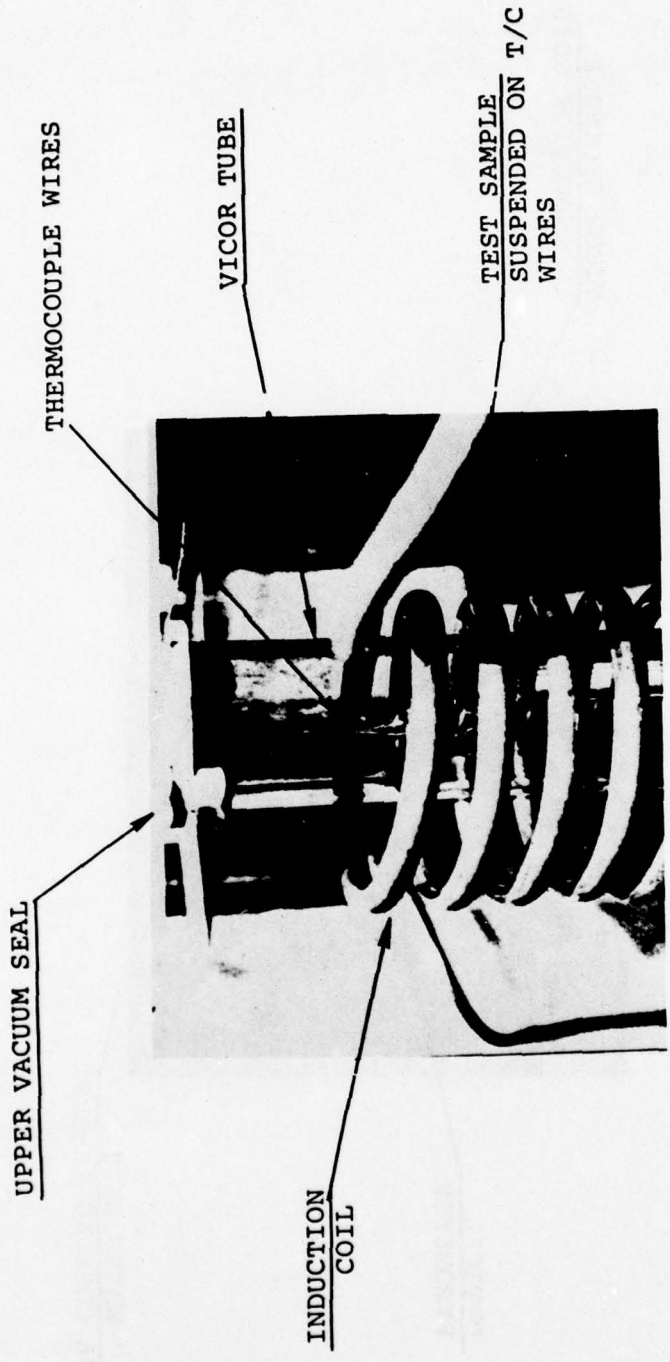
FIGURE 2-1c. CLOSE-UP OF TEST TUBE AND SPECIMEN

THERMOCOUPLE WIRES

VICOR TUBE

TEST SAMPLE
SUSPENDED ON T/C
WIRES

UPPER VACUUM SEAL

INDUCTION
COIL

The test specimen configurations are shown in Figure 2-2. The disc configuration with a Type E thermocouple welded to the backface was used for check-out and the Phase III impact tests. The rectangular specimens with a Type S thermocouple welded to the end were used exclusively for the oxygen weight gain tests.

The test procedure followed to obtain approximately isothermal weight gain data consisted of the following steps: 1) a pre-test weighing of the test specimen; 2) installing the test specimen and instrumentation; 3) establishing the desired pressure of the oxidizing environment with a continuous flow of the same gas through a test fixture; 4) initiating the induction heater and adjusting the power to attain the desired temperature level based on real-time observation of the specimen temperature history; 5) maintaining constant temperature for the prescribed test time; 6) cut-off of oxidizing environment and power; and, 7) post-test weighing of the test specimen plus any oxide spall (captured in a catcher at the bottom of the test rig).

Figure 2-3 shows thermocouple and pyrometer test results for a typical low and high temperature test run. The thermocouple measurements constitute the primary data with the pyrometer as back-up. Although a comparison of the temperatures indicated by the thermocouple and the pyrometer is not possible without emissivity data, confidence in the data can be gained by comparing the temperature changes indicated by the two independent instruments during the "constant" temperature period of the test. To this end, the relative sensitivities of the two instruments are indicated.

The results of the Phase I oxidation tests are tabulated in Table 2-1 for three series of tests. Appendix B provides detailed tabulated temperature-time data.

(MTL. T$_I$-6A$_L$-4V)

0.125"

0.750"

DISC CONF.

THERMOCOUPLE TYPES

Type S - Platinum vs Platinum-
10% Rhodium

Type E - Nickel-Chromium vs
Copper-Nickel

0.079"

0.807"

0.398"
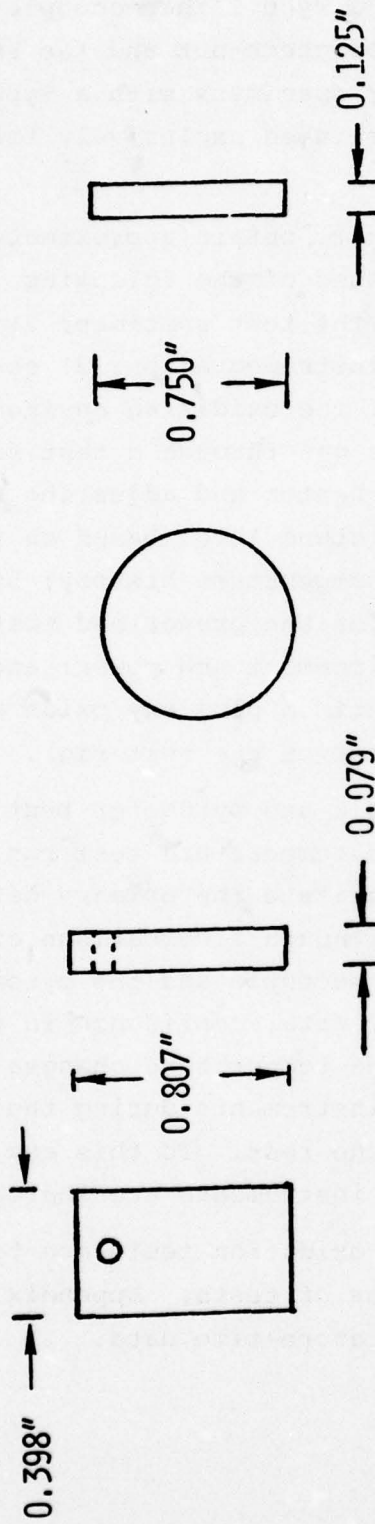
RECTANGULAR CONF.

THERMOCOUPLE
WIRES

SPOT WELDS

TYPICAL THERMOCOUPLE
INSTALLATION

FIGURE 2-2. TYPICAL TEST MODEL CONFIGURATIONS
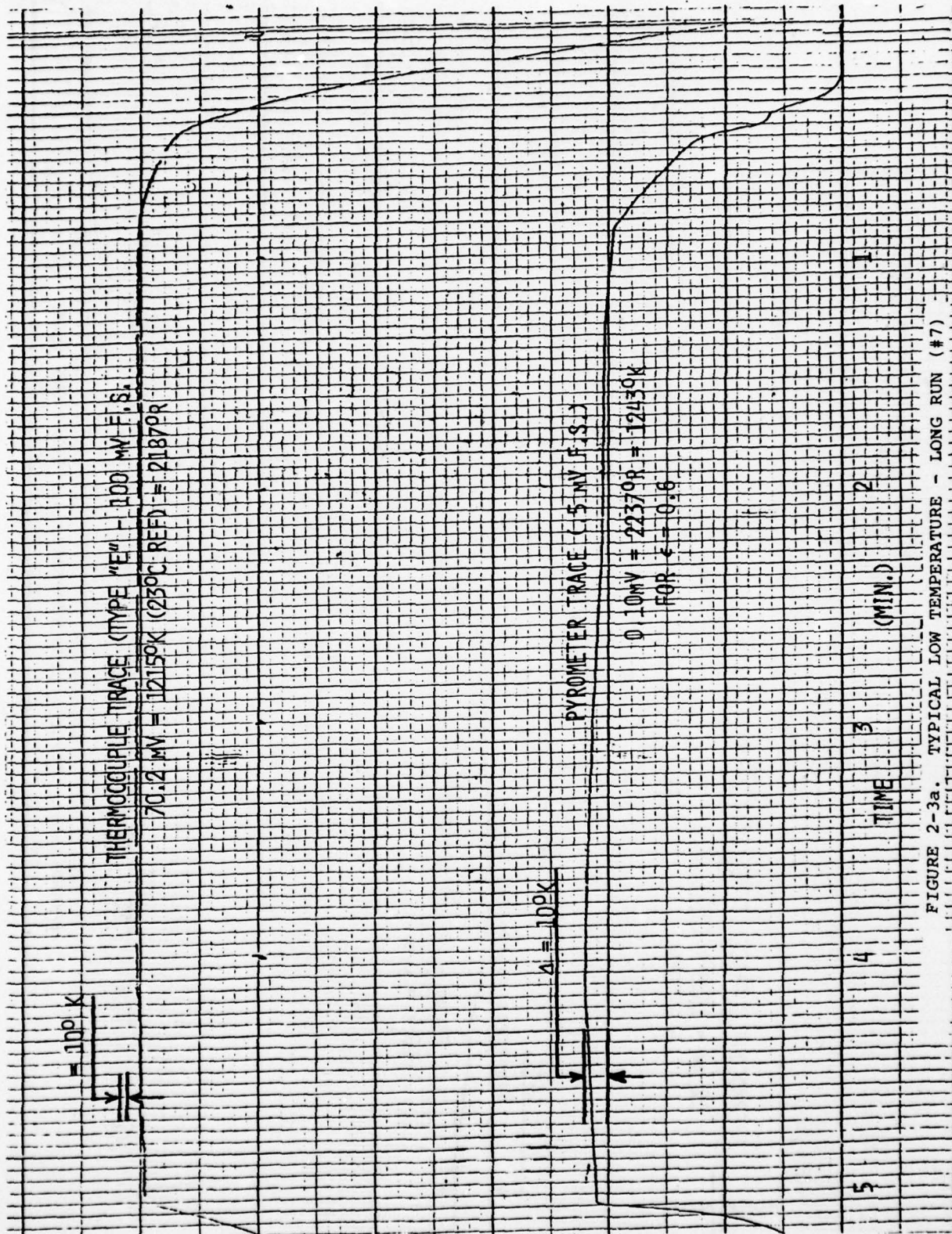
FIGURE 2-3a. TYPICAL LOW TEMPERATURE – LONG RUN (#7)
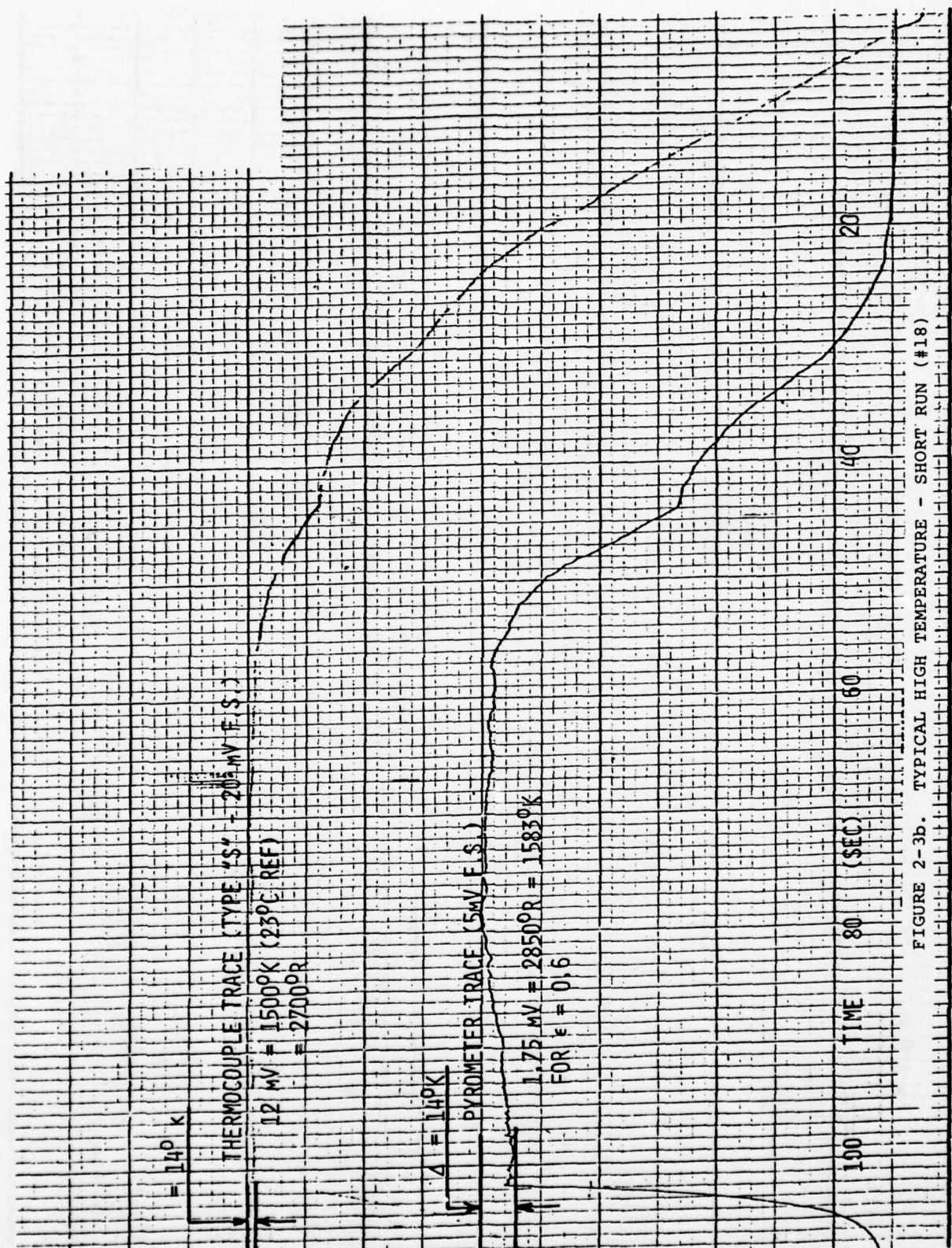
FIGURE 2-3b. TYPICAL HIGH TEMPERATURE – SHORT RUN (#18)

THERMOCOUPLE TRACE (TYPE "S" – 20 MV F.S.)

12 MV = 1500°K (23°C REF)
= 2700°R

PYROMETER TRACE (5 MV F.S.)

1.75 MV = 2850°R = 1583°K
FOR ε = 0.6

= 140° K

Δ = 140°K

TABLE 2-1A

TITANIUM OXIDATION RUN SUMMARY: SERIES 1, JANUARY 1977

RUN NO.	SAMPLE GEOMETRY	THERMOCOUPLE TYPE	NOMINAL TEMP (°K)	NOMINAL TIME (MIN)	PRESSURE (atm)	GAS COMPOSITION	WEIGHT GAIN (mg)	CHART SPEED	COMMENTS
4	Disc	E	1200	3	0.5	He	2.0	2"/m	
5	Disc	E	1200	3	0.5	He	1.4	2"/m	Good vacuum
6	Disc	E	1200	3	0.5	Arg.	2.0	2"/m	
7	Disc	E	1200	5	0.5	O_2	7.2	2"/m	Start heat in O_2
8	Disc	E	1200	1.5	0.5	O_2	1.6	2"/m	Noisy trace
9	Rect	S	1000	10	0.5	O_2	1.1	2"/m	Did not reach 1200 only 1000. Must re-set machine for high.
10	Rect	S	1200	5	0.5	O_2	5.4	2"/m	Had arc-over
11	Rect	S	1500	1.5	0.5	O_2	22.7	6"/m	Temp overshoot to ~1600
12	Rect	S	1500	1.5	0.5	H_2O	35 +	6"/m	Lost some flakes
15	Rect	S	1200	~7	0.5	H_2O	5.4	6"/m	
16	Rect	S	1200	5	0.5	Air	4.2	6"/m	Strip chart not available
17	Rect	S	1200	5	0.1	Air	6.2	6"/m	Strip chart not available
18	Rect	S	1500	1.5	0.5	50/50H_2O-Air	15	6"/m	Some flakes lost

TABLE 2-1B

TITANIUM OXIDATION RUN SUMMARY: SERIES 2, MAY 1977

RUN NO.	NOMINAL TEMP (°K)	NOMINAL TIME (SEC)	PRESSURE (atm)	GAS COMPOSITION	WEIGHT GAIN (mg)	COMMENTS
2	1500	100	0.5	O_2	16.15	No scale catcher in setup
3	1500	100	0.5	O_2	19.74	No scale catcher in setup
4	1600	100	0.5	O_2	73.75	
7	1650	50	0.5	O_2	101.76	
8	1500	100	0.5	$H_2O(v)$	46.57	Baked out weight less 1.7 mg
9	1500	100	0.5	O_2	22.34	
10	1450	100	0.5	$H_2O(v)$	35.22	Temp lower than 1500°K
11	1500	120	0.5	$O_2 H_2O(v)$	18.82	Mix of gases uncertain, significant pressure change
12	1500	100	0.5	$O_2 H_2O(v)$	19.66	Mix of gases uncertain, significant pressure change
15	1500	50	0.5	O_2	11.97	
17	1650	60	0.5	O_2	70.39	
18	1650	60	0.5	$H_2O(v)$	50.90	Temperature slightly low
19	1650	60	0.5	H_2O	63.20	Temperature too low
20	1200	300	0.5	$H_2O(v)$	8.56	Temperature too low
21	1200	300	0.5	$H_2O(v)$	8.10	
22	1500	35	1.0	O_2	-	Specimen ignited
24	1400	50	1.0	O_2	15.80	
25	1400	65	1.0	$H_2O(v)$	50.63	

NOTE: All specimens 1 cm x 2 cm x 0.2 cm, Mass = 1.8 gms. Thermocouples Type S.
Reference Temperature, 18°C. Chart speed 0.1 in/sec.

Table 2-1c
TITANIUM OXIDATION RUN SUMMARY: SERIES 3 JULY 1977

RUN NO.	NOMINAL TEMP (°K)	NOMINAL TIME (SEC)	PRESSURE (ATMOSPHERE)	GAS COMP.	WT. GAIN (mg)	COMMENTS
26	1500	60	0.5	H_2O	20.4	• time more like 58-63 sec but steady temp. - good run
27	1450	95	1.0	H_2O	31.2	• ~ 53 sec at $1500°K$ but additional 35 sec init at ~ $1400°K$! No good
28	1500	55	1.0	H_2O	40.0	• ~ 53-60 sec and steady good run.
29	1200	150	0.5	H_2O	6.8	• Temp overshot init ~ 40 sec
31	1600	70	0.5	H_2O	65.8	• Temp low most of run, more like ~ 70 sec @ $1600°K$
32	1600	80	0.5	H_2O	89.1	• Temp low-more like 80 sec @ $1600°K$ slightly higher levels to run 31 however higher pressure may cause high ΔW
33	1600	60	0.5	O_2	90.8	• Temp erratic (low) time about 60 sec @ ~ $1600°K$
34	1600	70	0.5	O_2	102.4	• Stable Temp not achieved, low temp ~ 70 sec @ $1600°K$
35	1650	60	0.5	O_2	120.7	• $1700°K$ maintained for only 10 sec -- ~60 sec total, most @ $1500°K+$, no good
36	1600	50	0.5	O_2	35.6	• Overshoot to nearly $1700°$ ~ 30 sec @ ~ $1400°K$, ~ 22 sec above $1500°K$ No good
37	1500	50	1.0	O_2	15.9	• Good run 50 sec @ ~$1500°K$
38	1500	50	1.0	O_2	16.7	• Slight overshoot for 1st 10 sec to ~$1550°K$ and undershoot for last 40 sec to ~$1450°K$, good
39	1300	300	0.5	O_2	10.8	• Temp overshoot ah ave. of ~$1300°K$ for entire 300 sec
40	1300	300	0.5	O_2	10.1	• Temp overshoot an ave. of ~$1300°K$ for entire 300 sec
41	1700	-	0.5	O_2	-	• Ignited at 5 sec, strange tc response above $1500°K$
42	1250	300	0.5	H_2O	17.0	• Temp $1200-1300°K$, good

The interpretation of the data and the identification of specific trends is deferred to Section 4 where the data is presented in light of predictive oxidation models. Two general observations which can be made from the raw data are depicted in Figure 2-4 where results obtained at 1500°K are presented. A significant increase in oxygen uptake is seen for tests in water over tests in pure oxygen at 1500°Kelvin. A similar trend was observed at 1200°K, however, no difference was measured at 1700°K. It is also surprising to note that data obtained with a 50 percent mixture of oxygen and water vapor agreed with data obtained in pure oxygen at all temperatures tested. Unfortunately, the limited data generated does not permit any conclusions to be drawn from these observations.

For the two pressure levels tested, namely 1/2 and 1 atmosphere, both water and oxygen data suggest an increase in oxygen uptake with increasing pressure. This trend was unexpected although reported once in Ref. 10 since gas phase diffusion cannot be important in a single component atmosphere. As will be discussed in Section 4.0, this pressure effect may result from gas phase rate-limiting processes as opposed to any basic change in the solid phase oxidation or dissolution processes.

During the Series 2 and 3 tests conducted under this program, two titanium samples ignited and were consumed. The conditions for these tests were 1500°K, 1 atm O_2 and 1700°K, .5 atm O_2. Examination of all available data on sample response and facility performance parameters revealed that in each case, the induction heater plate current, a measure of power delivered, increased spontaneously at the time the sample ignited. It cannot be stated with certainty if the ignition process proceeded and caused the abnormal induction heater response or if the induction heater
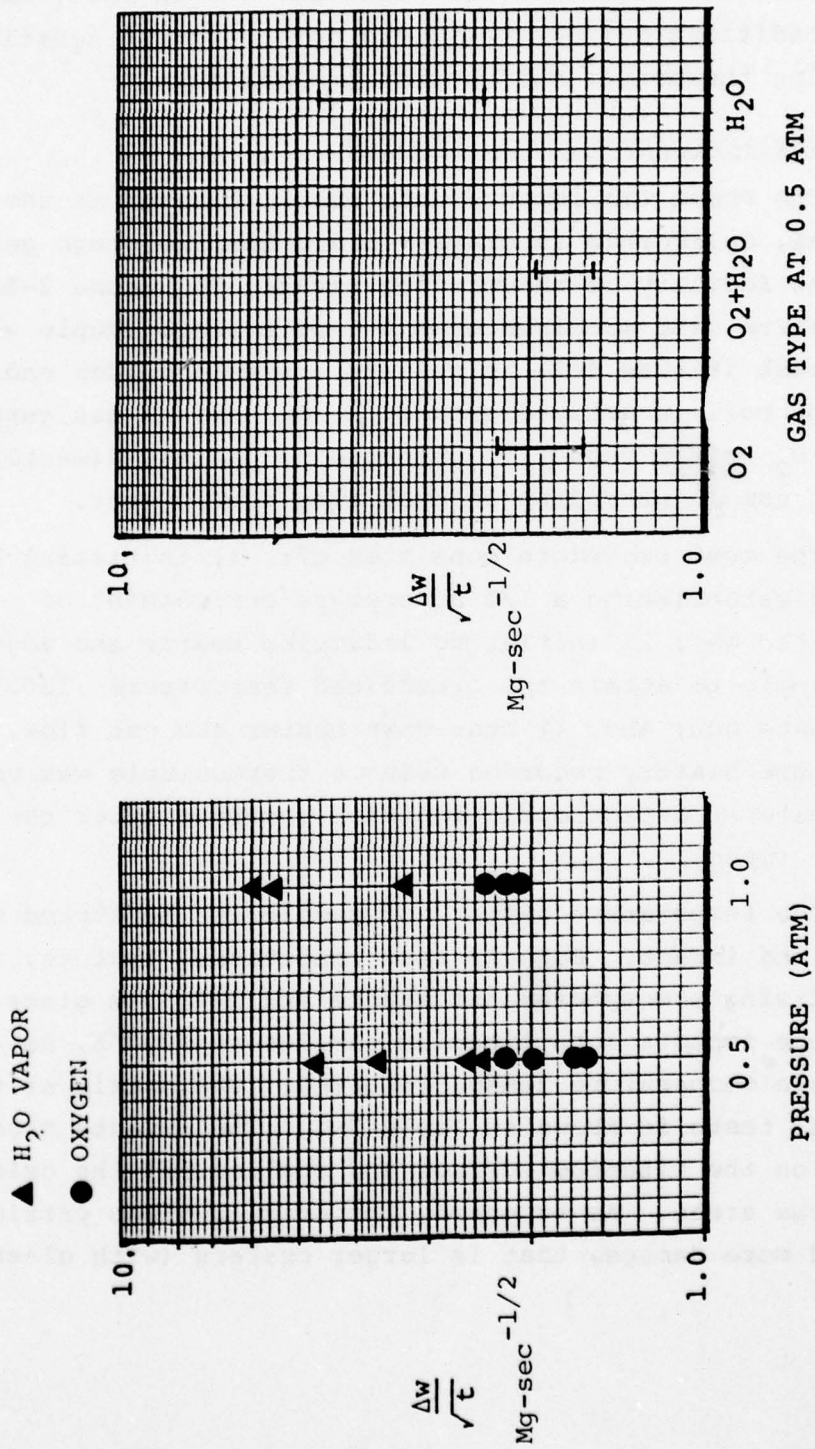
FIGURE 2-4. OXIDATION DATA TRENDS AT 1500°K

malfunctioned and caused the sample to ignite. Such heater malfunction is not likely but possible. Repeats of the test conditions where ignition was observed, and in fact, exceeding these conditions deliberately, did not result in ignition supporting the heater malfunction explanation.

2.3   Particle Impact Test Program

The Phase III impact tests were conducted at the SAI Santa Ana, California laboratory using the two-stage gas gun. The facility is shown schematically in Figure 2-5. The titanium disc specimen with a Type E thermocouple welded to the back (Figure 2-2) is held in a sample holder and the induction coil is wrapped around the holder. A gas supply line (either O_2 or H_2O vapor) is oriented to impinge directly on the test sample providing an oxidizing environment.

The test procedure consisted of: 1) initiating gas flow and establishing a 1/2 atmosphere environment of the desired gas; 2) initiating induction heater and adjusting power supply to attain the prescribed temperature (1200^OK); 3) initiate gun; and, 4) shut-down heater and gas flow. The temperature history recorded using a thermocouple was used to evaluate if catastrophic ignition occurred after the particle impact.

The temperature history of sample was monitored during heat-up and impact. For all test conditions, that is, inert and oxidizing atmospheres and single and multiple glass and single ice impacts into titanium samples at 1200^OK, no measurable temperature damage resulted. The matrix of the Phase III tests is shown in Table 2-2. The impacts produced craters on the titanium surface and spalled off the oxide layers over large areas. As expected, the heavier glass particles produced more damage, that is larger craters (with glass residue

2-14

SAMPLE HOLDER

T/C LEADS

TEST TANK

TEST SAMPLE

GAS SUPPLY

TO TEST TANK

GAS SUPPLY (O₂ & STEAM) TO IMPINGE ON SAMPLE

INDUCTION COIL

TWO-STAGE GAS GUN
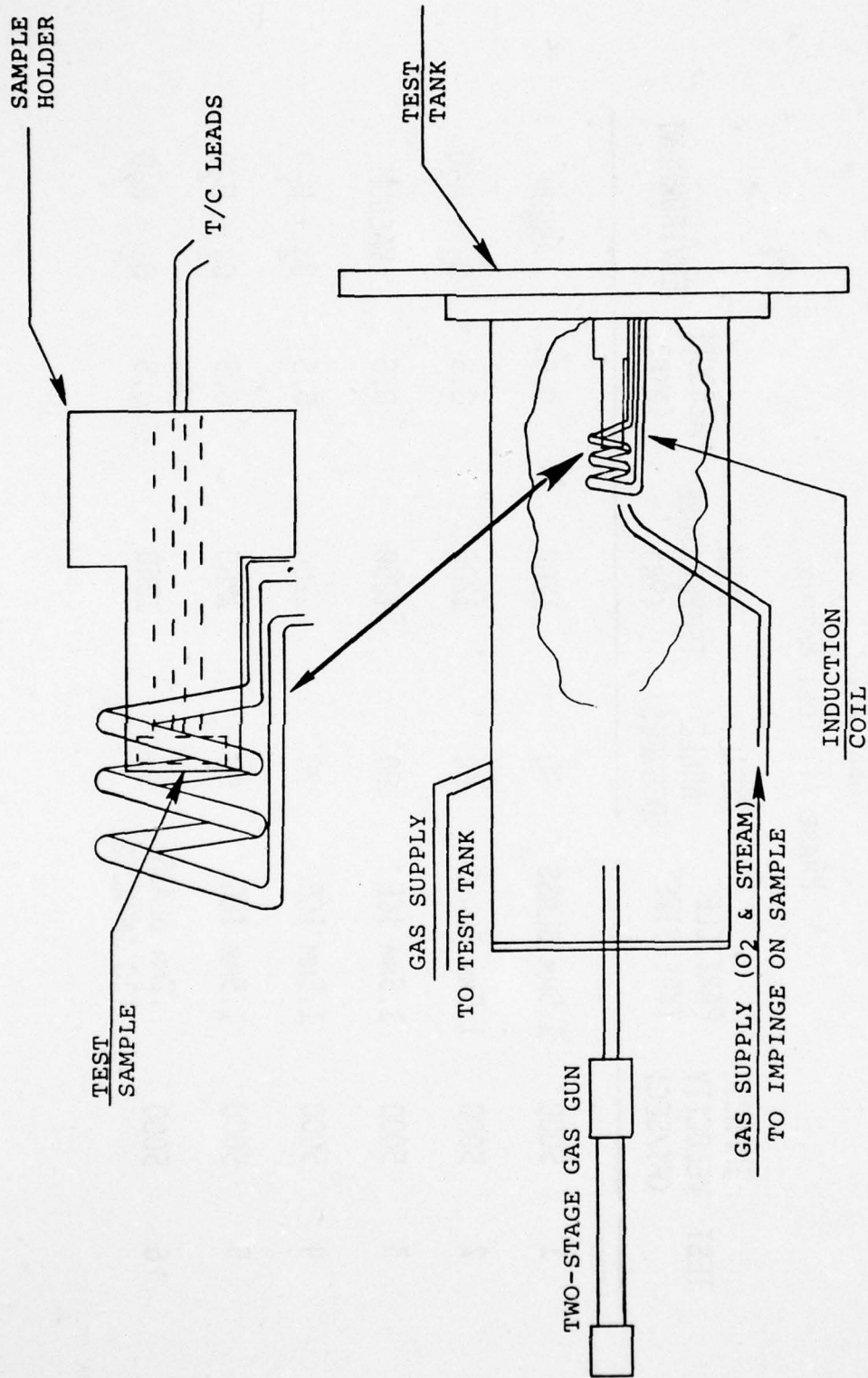
FIGURE 2-5. FACILITY SCHEMATIC FOR IMPACT/OXIDATION EXPERIMENTS

2-15

TABLE 2-2

PHASE III TEST MATRIX

TEST	IMPACT VELOCITY (FT/SEC)	PARTICLE TYPE/SIZE	IMPACT ANGLE (DEGREES)	BULK TEMPERATURE (°K)	PRESSURE (ATM)	ENVIRONMENT
1	5000	1.5MM GLASS	90	1200	0.5	ARGON
2	5000	1.5MM GLASS	90	1200	0.5	$O_2 + H_2O$
3	5000	1.5MM ICE	90	1200	0.5	VACUUM
4	5000	1.5MM ICE	90	1200	0.5	$O_2 + H_2O$
5	5000	1.5MM ICE	90	1200	0.5	$O_2 + H_2O$
6	5000	.2MM GLASS (20 IMPACTS)	90	1200	0.5	$O_2 + H_2O$

in the crater bottom) and larger spall regions than the ice
particle.   A comparison of two typical craters resulting
from ice and glass impact is shown in the post test photograph
of Figure 2.6.
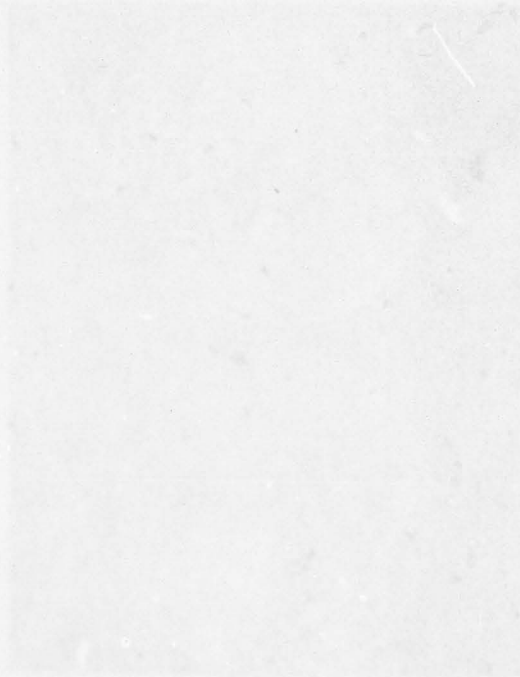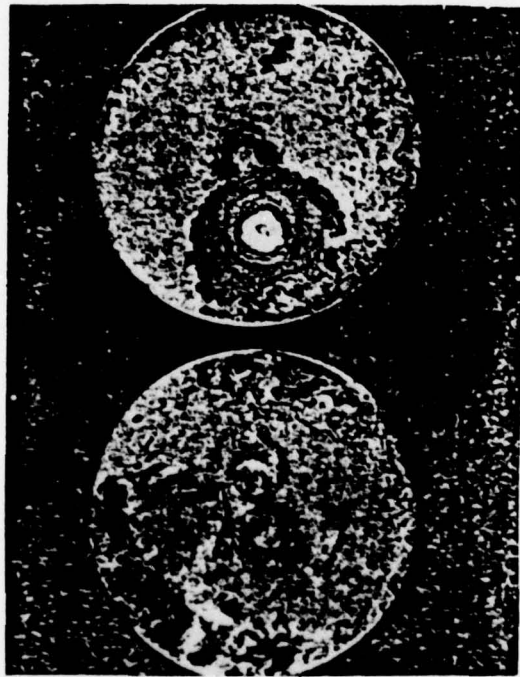
FIGURE 2-6. TYPICAL POST TEST PHOTOGRAPHS
OF TITANIUM SAMPLES
LEFT: ICE IMPACT, RIGHT: GLASS IMPACT

2-18

3.0   AEDC DET EROSION AND OXIDATION TEST SERIES

3.1   Background

The test results described in the preceding section show the effect of oxidizing environments (H_2O vapor and O_2) on titanium under both non-erosive and single impact test conditions using both non-reactive (glass) and reactive (ice) particles. This data is fundamental to the development of a predictive model for titanium response as will be discussed in Section 4.0. However, the test conditions are not representative of the multiple impact, hypersonic flow environment expected for a missile structure in-flight. Consequently, a test series was planned which would use the AEDC Dust Erosion Tunnel (DET) to evaluate titanium response to multiple particle impacts in a hypersonic flow environment. A facility modification was implemented to introduce liquid water simultaneously with dust (magnesium oxide) particles in an attempt to simulate the nuclear cloud water and dust environment.

Extensive tests of titanium nosetip models have been conducted in the DET in previous programs (References 1-5). These tests have been conducted to evaluate increased heat transfer in particle environments. Important mechanisms include particle kinetic energy transfer, particle-flowfield interaction convective heat transfer, and high temperature chemistry heating augmentation due to surface oxidation. These effects have been adequately modeled for dust part- icle/air environments. However, the effect of water, in the form of ice, liquid, or vapor in conjunction with a dust/air environment, on titanium has not been addressed. The con- cern was that water could increase the surface chemistry effect on titanium under erosive conditions and should be considered in the design of titanium missile structures. This AEDC DET test program was structured to evaluate this concern.

3.2 Test Objectives

A test program was planned for the AEDC DET to investigate the effects of water/air mixtures on the oxidation response of titanium under multiple dust particle conditions. Although the DET is used routinely for dust erosion testing, water had not been injected prior to this program. A facility modification was implemented to inject liquid water either separately or in combination with dust (MgO) particles. The goal was to achieve liquid water droplet impacts on the hemispherical titanium models which had been heated to high temperature by the hypersonic air and dust flow. This test program was the first such utilization of the AEDC DET and was necessarily exploratory in nature.

3.3 Test Program Description

3.3.1 Facility Description

The tests were conducted in the Arnold Engineering Development Center, Propulsion Wind Tunnel Facility, Dust Erosion Tunnel (DET). A description of the DET is given in Reference 6. All test runs were made at the 127.5-in. nozzle station, where the exit diameter is 8.3 in. and the nominal Mach number is M = 6.6 to 7.5, depending on operating conditions. A facility modification was designed and implemented to inject liquid water simultaneously with the dust particles. A schematic of the water/dust injection strut is shown in Figure 3-1. A separate water injection system was designed. The water injection line is shown in Figure 3-1 next to the dust injection line. Various orifices on the water injection line were evaluated to obtain the desired flow conditions.

3.3.2 Water Orifice Calibration

A series of bench tests were performed to calibrate the water orifice. Four designs for the orifice were evaluated. The objective of the calibration tests was to obtain

FIGURE 3-1. WATER/DUST INJECTION STRUT SCHEMATIC

a water jet with minimum divergence. This minimizes the tendency of the injected water to atomize in the throat region of the AEDC DET and maximizes the possibility of water impinging on the model at the test section. Test data includes photographic records of the water jet exiting the orifice and a calibration curve of injected water flow rate $\dot{M}_{H_2O}$ (gal/min) versus pressure differential ΔP (psia). The test procedure was as follows:

1) The water hopper was charged with a weighed amount of water (distilled).

2) The hopper was pressurized with N_2 and the orifice flow recorded on film for nominal ΔP's of 200, 500, and 800 psi.

3) After each flow period (1 minute for 0.062 orifice, and 2 minutes for the rest) at each ΔP, the water was carefully drained from the system and weighed.

4) The hopper was re-charged and the sequence was repeated for 12 data points.

Table 3-1 summarizes the 12 bench tests indicating ΔP, orifice design and measured $\dot{M}_{H_2O}$. Figure 3-2 is a schematic of the orifice design for scenes 4-9. The 0.02 inch counterbored design was ultimately chosen for testing in Runs 5-8. Scenes 1-3 and 10-12 correspond to an early straight-through design shown in Figure 3-3 and used in Runs 1-4, where, as indicated in Figures 3-4 - 3-7, significant divergence of the water jet was obtained. This may explain the reason for no apparent water impinging on models in early runs (1-3) for low injection rates (see discussion in Section 3.4).

TABLE 3-1

WATER ORIFICE CALIBRATION

SCENE	NOM. ΔP, PSI	ORIFICE DIA, in	COUNTER BORED EXIT	CONICAL INLET	FLOW RATE, GPM
1	200	.0625	NO	YES	1.34
2	500				2.07
3	800	↓	↓	↓	2.68
4	200	.040	YES	YES	0.56
5	500				0.88
6	800	↓	↓	↓	1.18
7	200	.020	YES	YES	0.16
8	500				0.25
9	800	↓	↓	↓	0.33
10	200	.020	NO	NO	0.15
11	500				0.22
12	800	↓	↓	↓	0.28

1. Not to scale.
2. All dimensions in inches.

0.062

Material: Brass

THREAD 12-28 x 0.25 D.P.

B

0.062

0.188

L

D

FLOW

60°

D	L	B
0.02	0.08	0.10
0.04	0.10	0.10
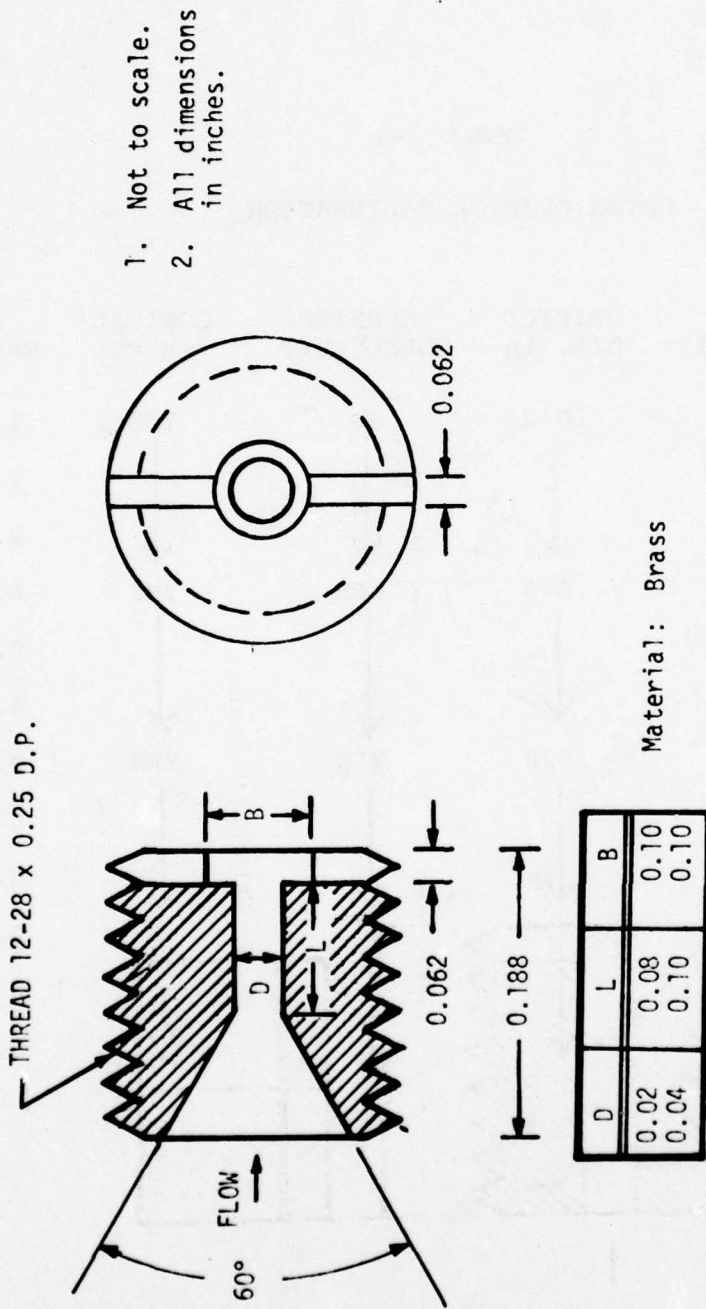
FIGURE 3-2. CONICAL INLET, COUNTERBORED EXIT DESIGN

NOTES:
1. Not to scale.
2. All dimensions in inches.

THREAD 12-28 x 0.25 D.P.

0.062

FLOW
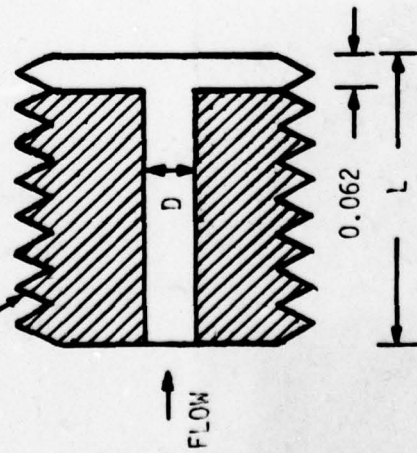
D	L
0.02	0.188
0.04	0.188
0.016	0.188
0.0625	0.188

Material: Brass
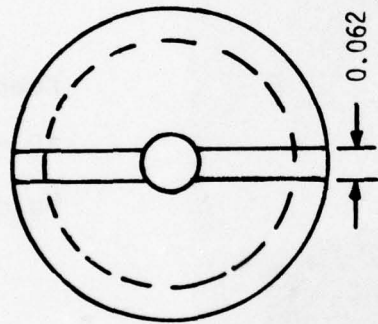
0.062

FIGURE 3-3. STRAIGHT THROUGH DESIGN
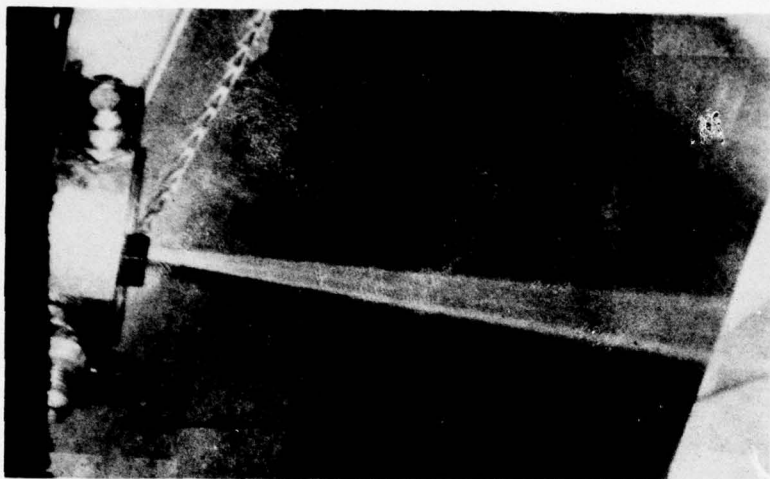
Scene 1

ΔP = 200 psi

$\dot{M}_{H_2O}$ = 1.34 gal/min

Scene 2

ΔP = 500 psi

$\dot{M}_{H_2O}$ = 2.07 gal/min

Scene 3

ΔP = 800 psi

$\dot{M}_{H_2O}$ = 2.68 gal/min

FIGURE 3-4.   WATER CALIBRATION FOR 0.062 IN. ORIFICE (SCENES 1-3)

3-8
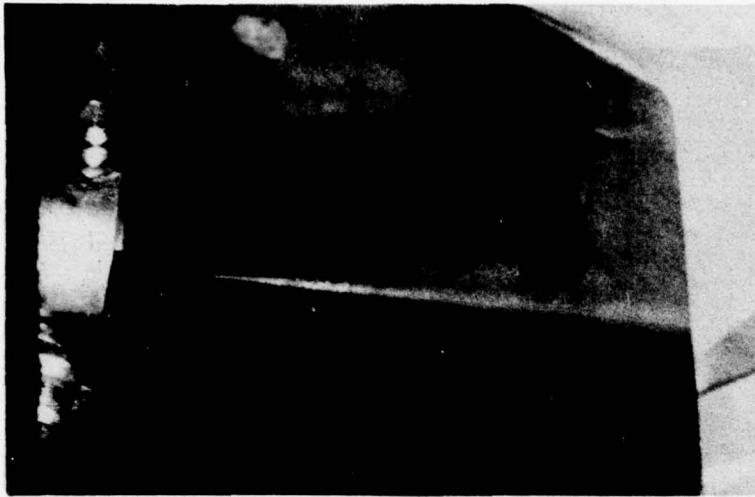
Scene 4

$\Delta P = 200$ psi

$\dot{M}_{H_2O} = 0.56$ gal/min
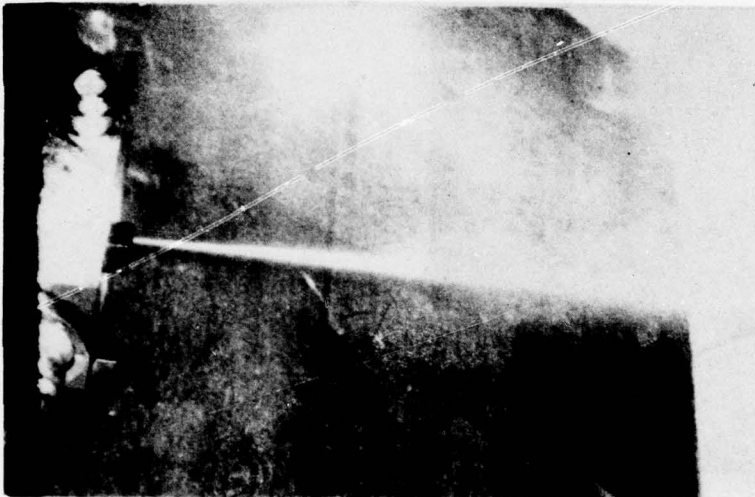
Scene 5

$\Delta P = 500$ psi

$\dot{M}_{H_2O} = 0.88$ gal/min
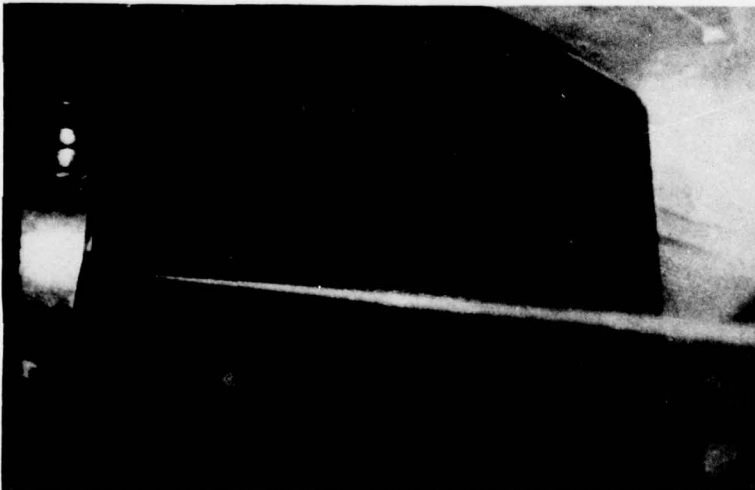
Scene 6

$\Delta P = 800$ psi

$\dot{M}_{H_2O} = 1.18$ gal/min

FIGURE 3-5.   WATER CALIBRATION TEST FOR 0.040 IN. ORIFICE (SCENES 4-6).
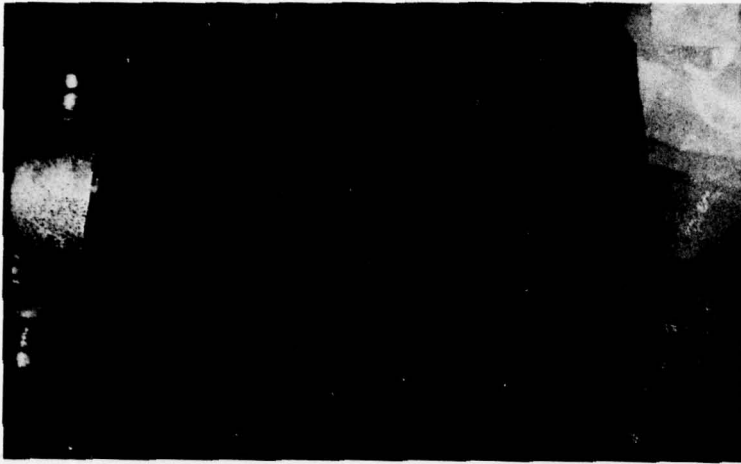
Scene 7

$\Delta P = 200$ psi

$\dot{M}_{H_2O} = 0.16$ gal/min
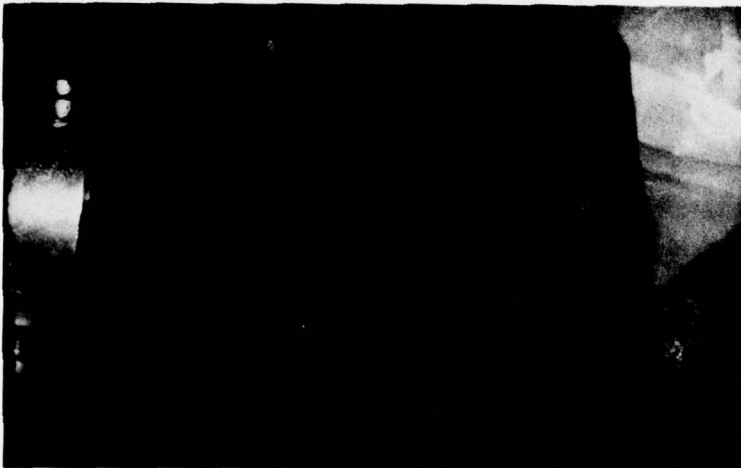
Scene 8

$\Delta P = 500$ psi

$\dot{M}_{H_2O} = 0.25$ gal/min
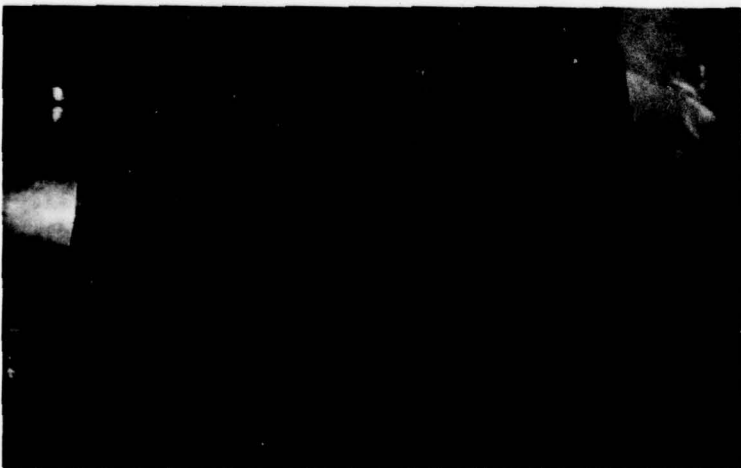
Scene 9

$\Delta P = 800$ psi

$\dot{M}_{H_2O} = 0.33$ gal/min

FIGURE 3-6.   WATER CALIBRATION TEST FOR 0.020 IN. ORIFICE (SCENES 7-9)
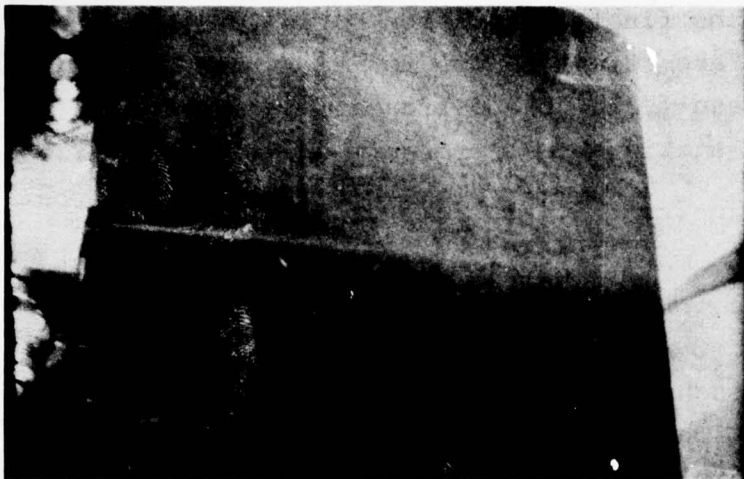
Scene 10
ΔP = 200 psi
$\dot{M}_{H_2O}$ = 0.15 gal/min

Scene 11
ΔP = 500 psi
$\dot{M}_{H_2O}$ = .22 gal/min

Scene 12
ΔP = 800 psi
$\dot{M}_{H_2O}$ = 0.28 gal/min

FIGURE 3-7.   WATER CALIBRATION FOR 0.02 IN. ORIFICE
(SCENES 10-12)

Figure 3-8 is the final calibration curve for each design. Also plotted are actual values for test runs. Differences apparently result due to a difference in exit orifice pressure from static throat pressure under dynamic flow conditions.

3.3.3 Models

The test models were 6Al-4V titanium consisting of eighteen 2.0 inch diameter (see Figure 3-9 for pre-test photos) and four 3.0 inch diameter models (see Figure 3-10 for pre-test photos). The hemispherical models all had a 0.25 inch skirt as shown in Figure 3-11 for attachment to the model holder shown in Figure 3-12. Each hemisphere was instrumented with eight platinum-platinum, 10 per cent rhodium thermocouples welded to the backside at the locations shown in Figure 3-11. Table 3-2 presents the pre-test skin thicknesses for each model and thermocouple location.

3.3.4 Instrumentation

In addition to the normal DET facility measurements, primary measurements on this program consisted of test section total pressure and total temperature, backface model temperatures, dust and water injection rates, water content in the test gas, and motion picture coverage.

A pressure probe was used to measure the pitot or normal shock recovery pressure. This probe was a hemisphere-cylinder with one inch diameter (Figure 3-13a) and a 1/16 inch diameter orifice at the sphere stagnation point. The total temperature probe, shown in Figure 3-13b, used a sheathed Pt-Pt, 13 per cent Rh thermocouple with a vapor-deposited junction shielded by a cylindrical tube made of magnesia-stabilized zirconia. The pressure probe and temperature probe outputs were recorded on conventional strip chart recorders. Model backside thermocouple outputs were
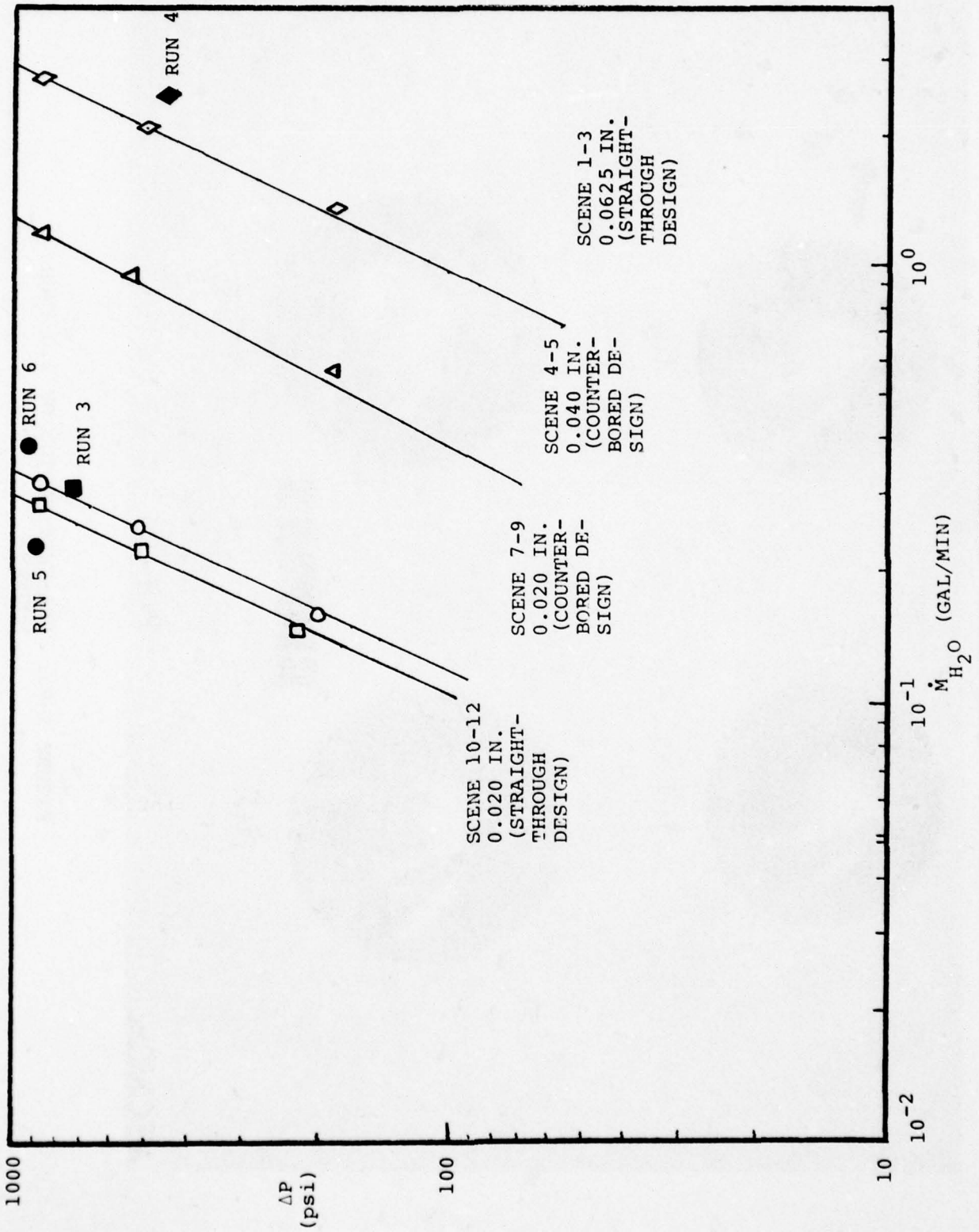
FIGURE 3-8. WATER ORIFICE CALIBRATION RESULTS

P41E-J7A
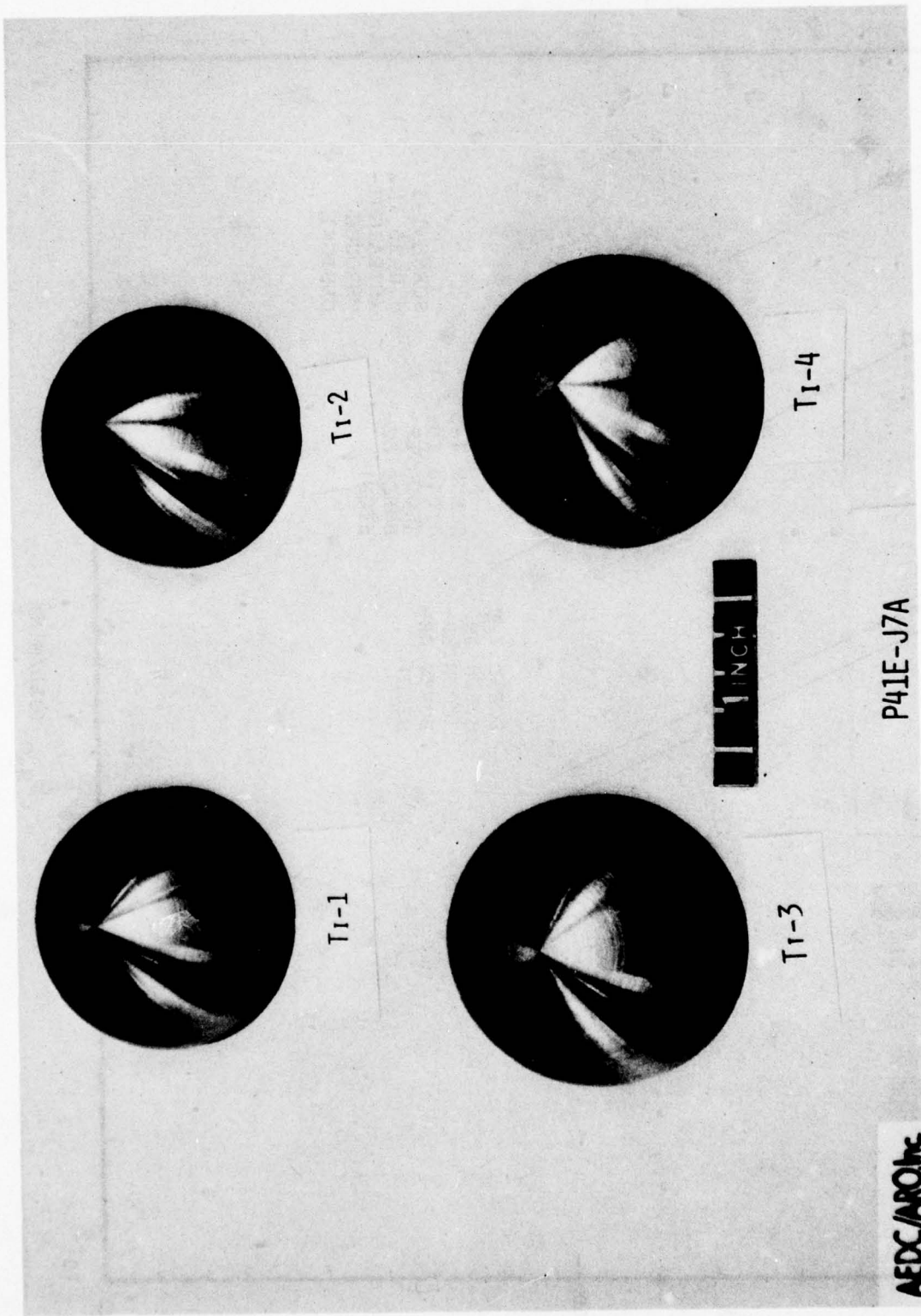
FIGURE 3-9a. PRE-TEST PHOTOS OF 2.0 INCH MODELS

T₁-6

T₁-8

1 INCH

P41E-J7A

T₁-5

T₁-7

AEDC/ARO,Inc.
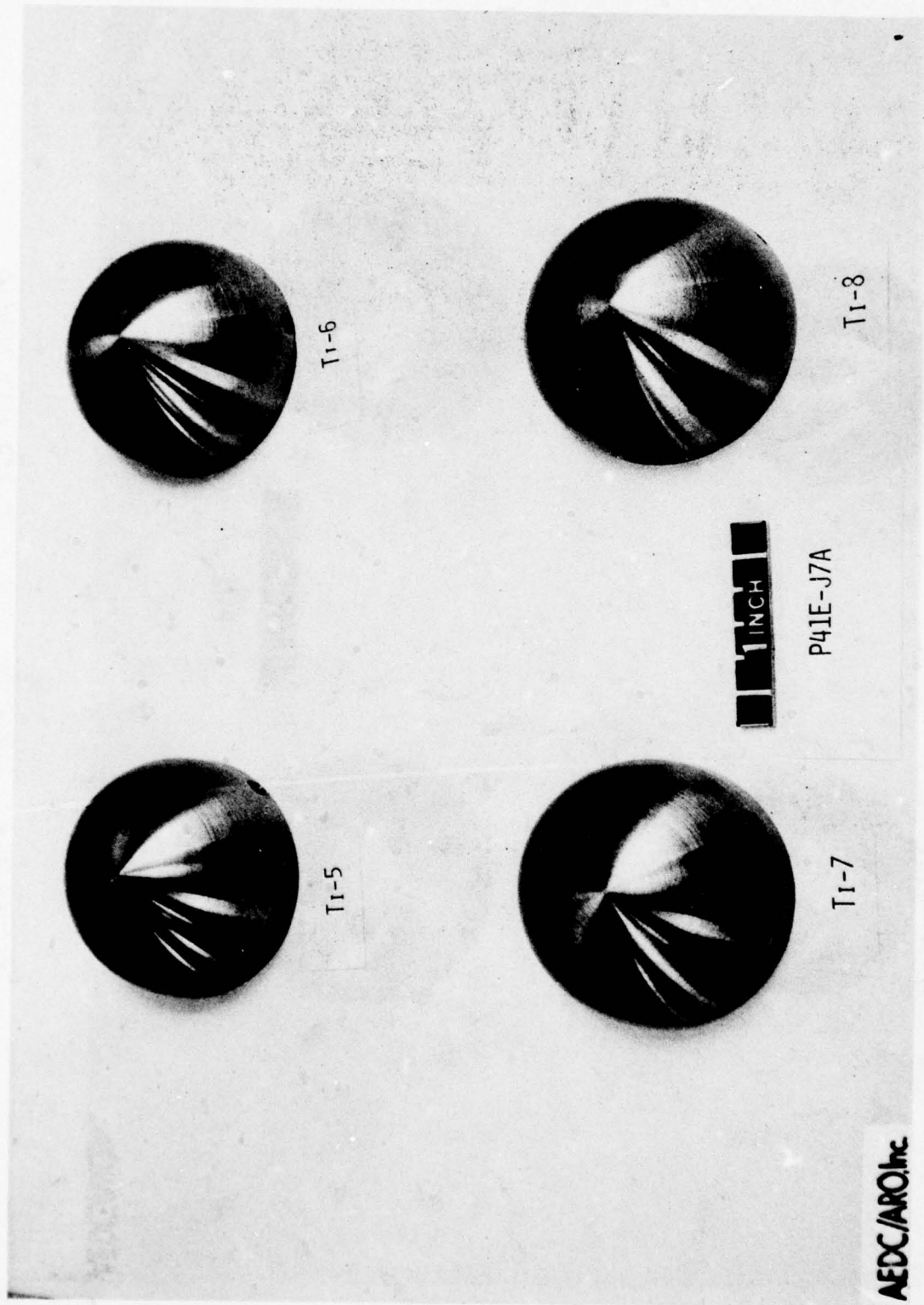
FIGURE 3-9b. PRE-TEST PHOTOS OF 2.0 INCH MODELS

T1-10

T1-12

P41E-J7A

T1-9

T1-1J

AEDC/ARO,Inc.
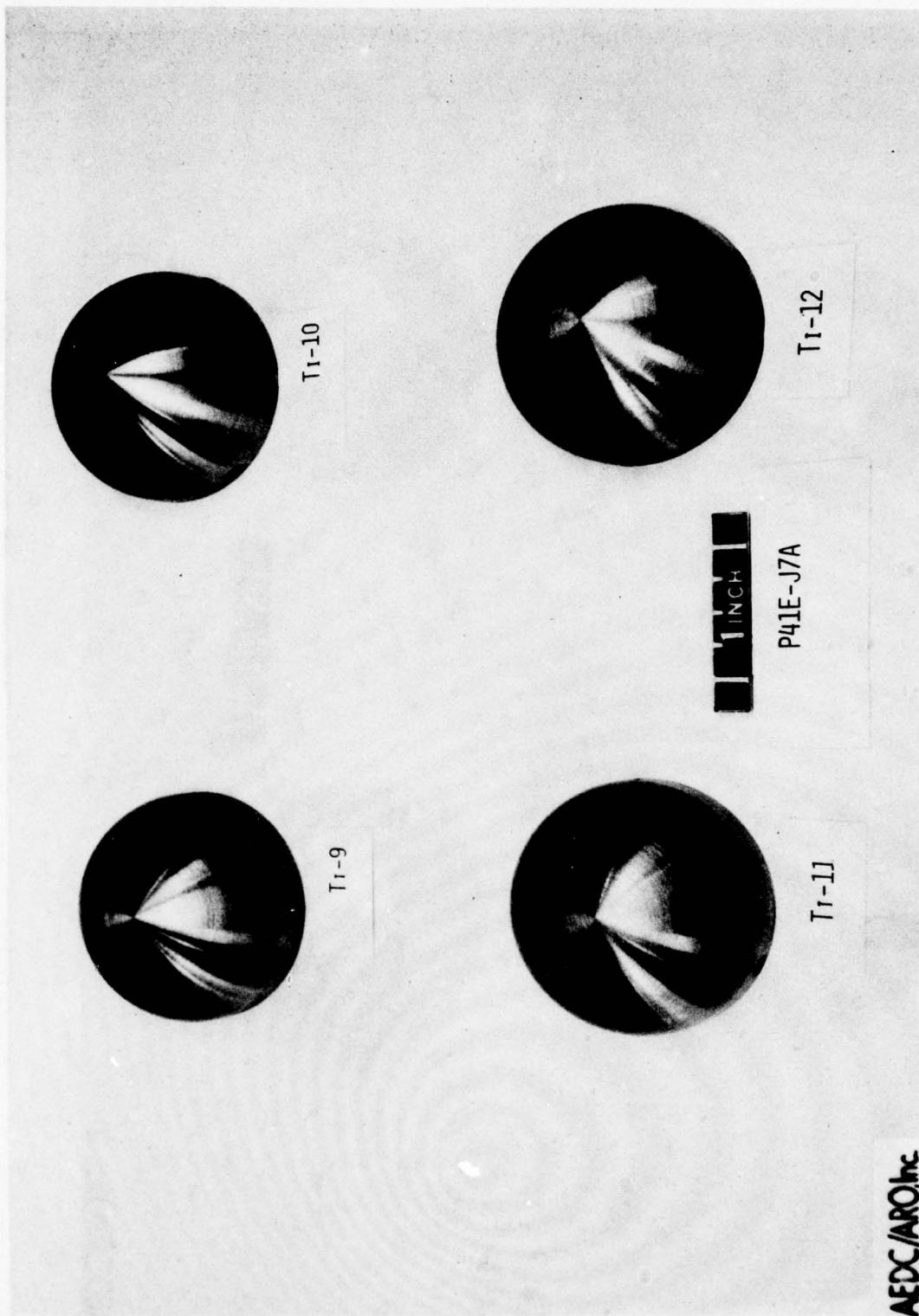
FIGURE 3-9c. PRE-TEST PHOTOS OF 2.0 INCH MODELS
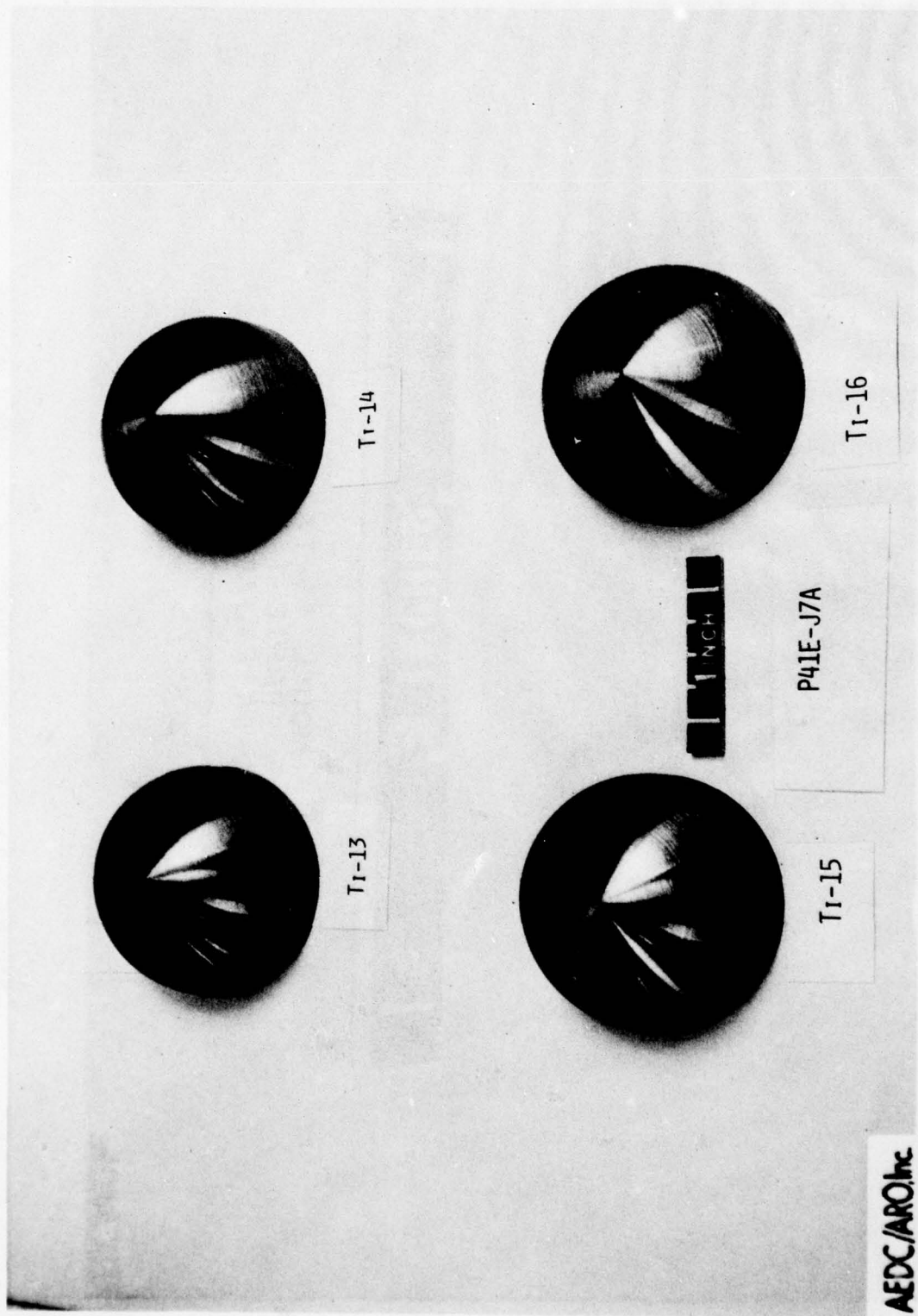
FIGURE 3-9d. PRE-TEST PHOTOS OF 2.0 INCH MODELS

3-17

MODEL Ti-17
PRETEST
P41E-J7A
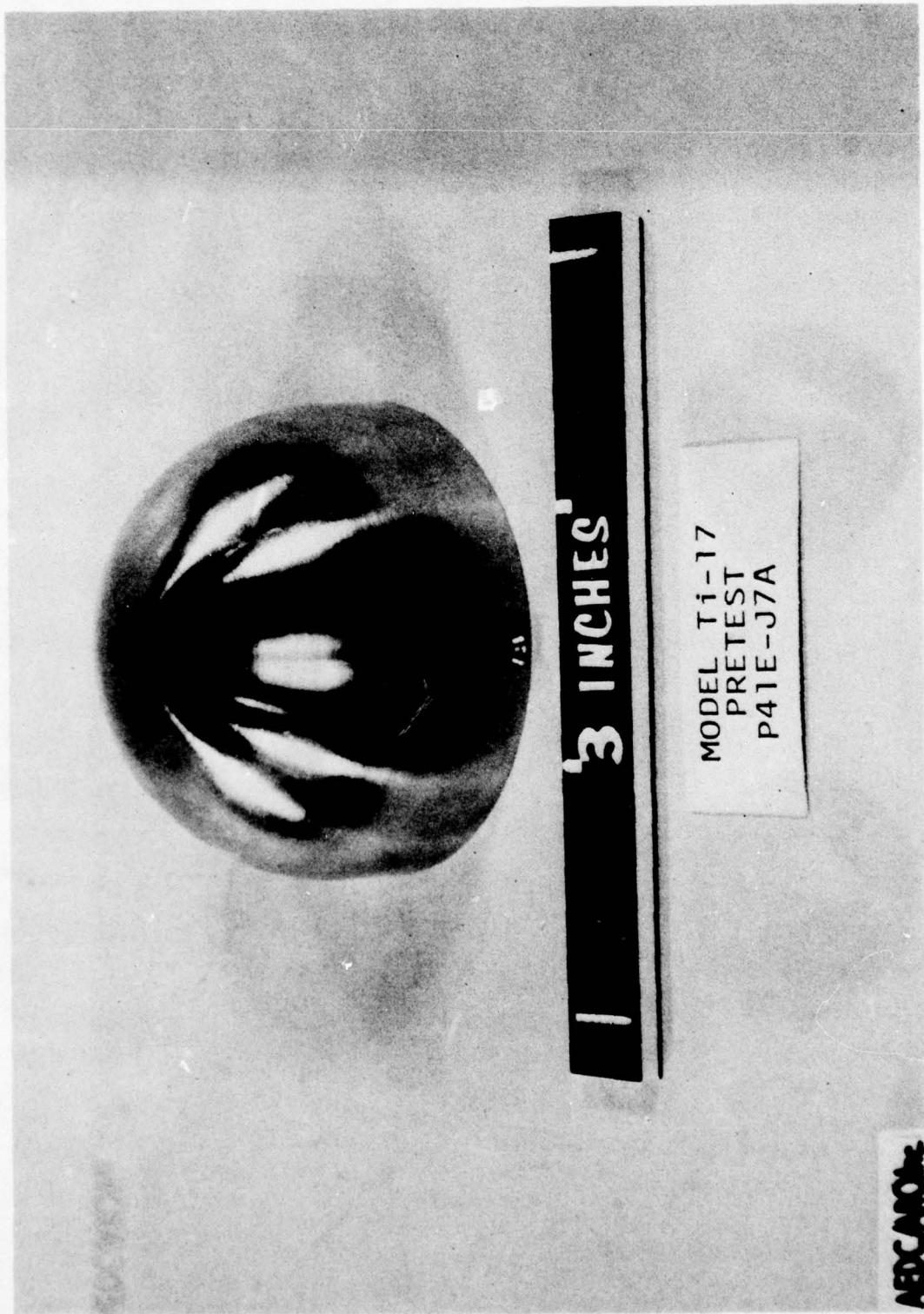
FIGURE 3-9e. PRE-TEST PHOTOS OF 2.0 INCH MODELS
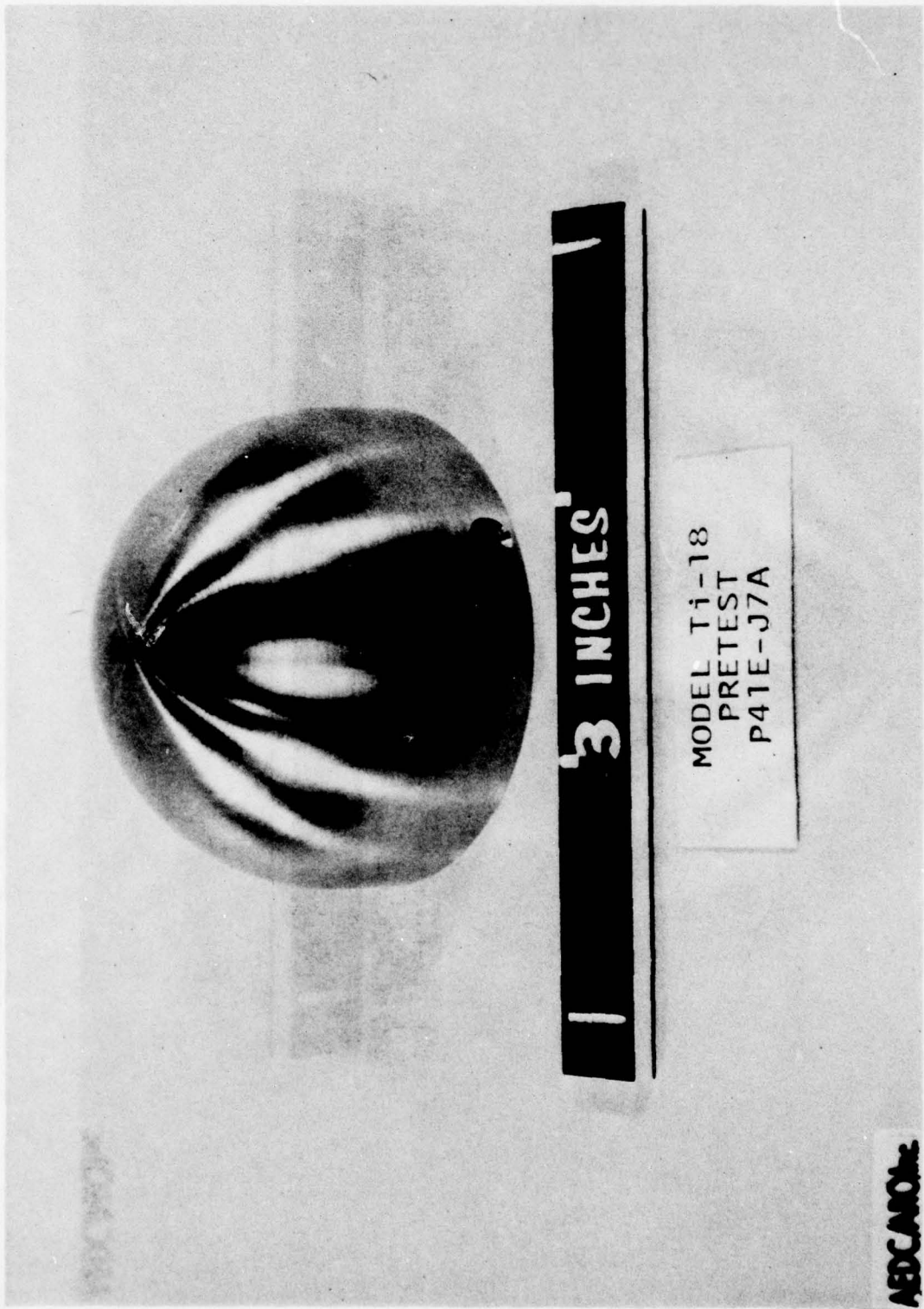
FIGURE 3-9f. PRE-TEST PHOTOS OF 2.0 INCH MODELS

3 INCHES

MODEL Ti-22
PRETEST
P41E-J7A

AEDC/AROInc
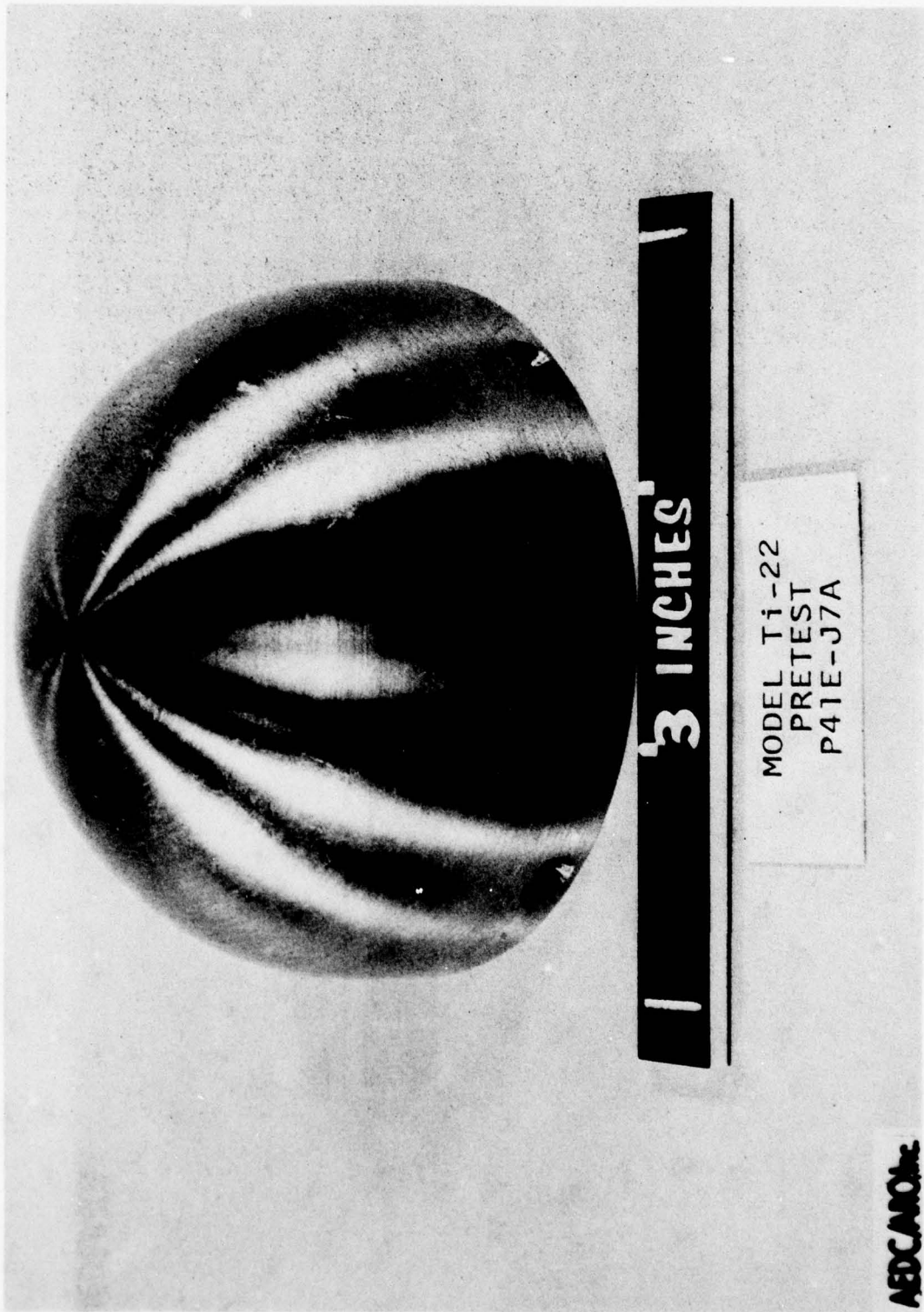
FIGURE 3-10a. PRE-TEST PHOTOS OF 3.0 INCH MODELS

MODEL Ti-23
PRETEST
P41E-J7A

3 INCHES
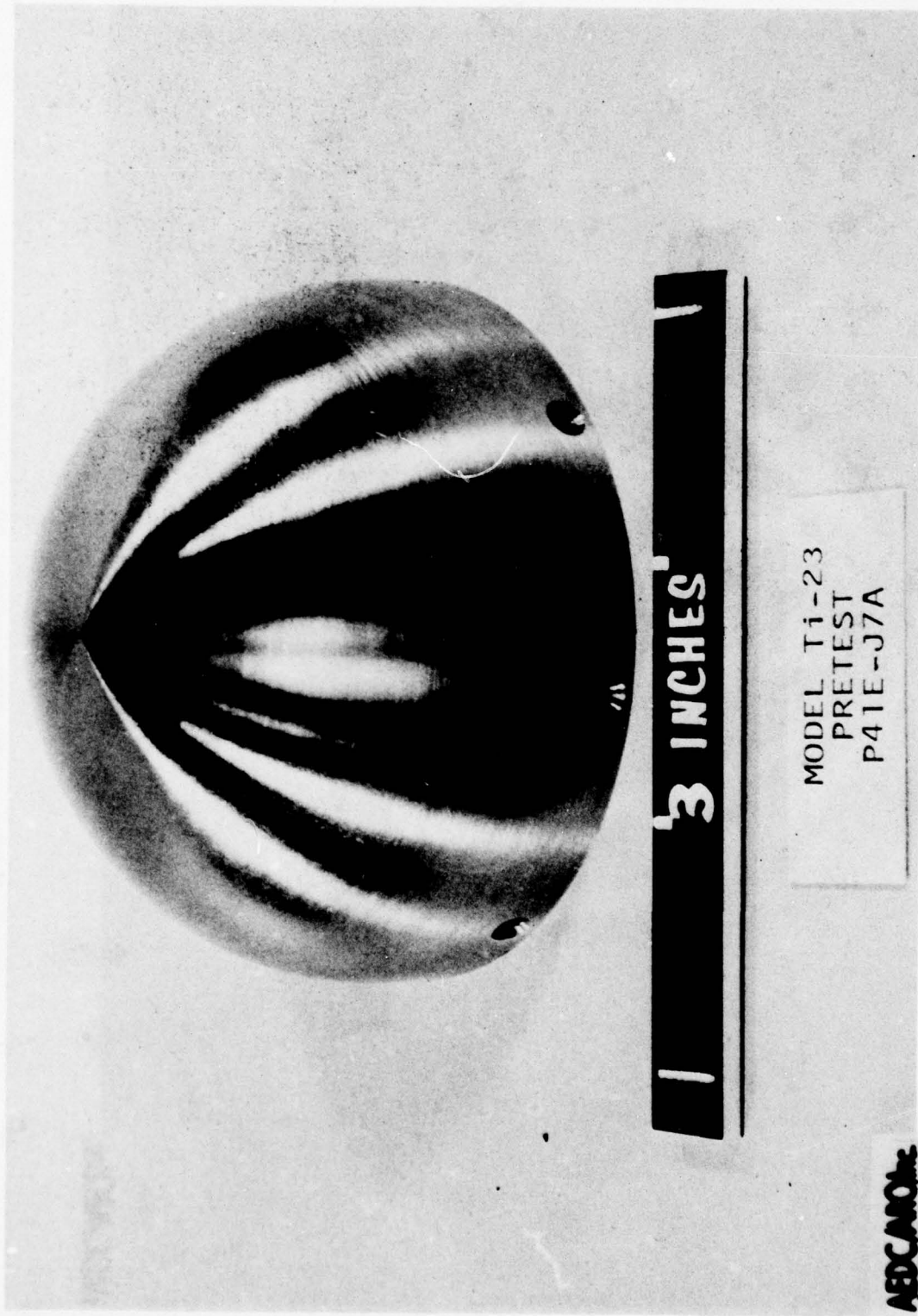
FIGURE 3-10b. PRE-TEST PHOTOS OF 3.0 INCH MODELS

MODEL Ti-53
PRETEST
P41E-J7A
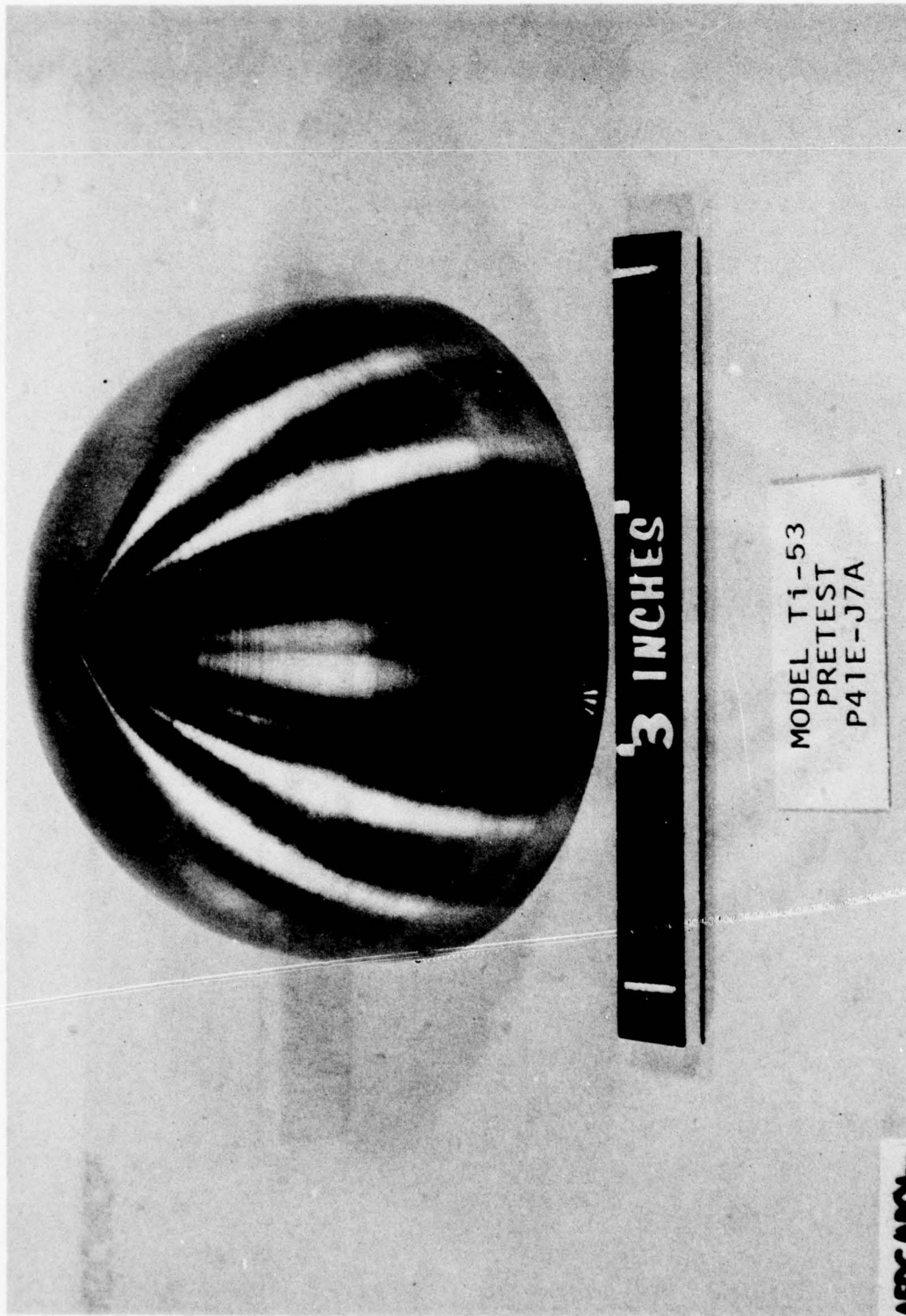
FIGURE 3-10c. PRE-TEST PHOTOS OF 3.0 INCH MODELS
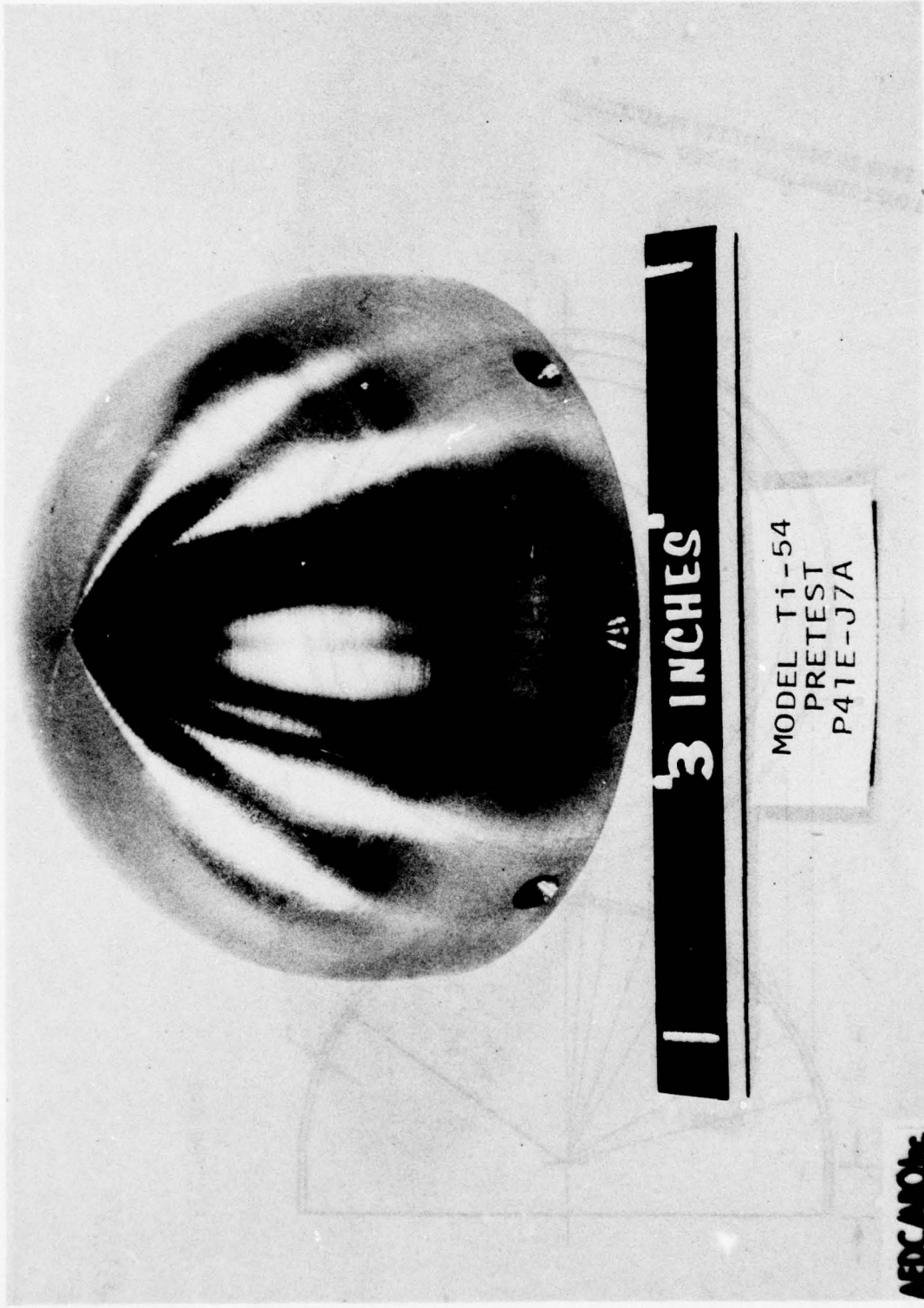
FIGURE 3-10d.   PRE-TEST PHOTOS OF 3.0 INCH MODELS

3-23

T/C LOCATION

Not to Scale.

BACK VIEW

75°
60°
30°
20°
10°
5°

0.25 in.

R_N = 1.0 in.
or 1.5 in.

t = 0.045 in. (Nominal)

SECTION A-A
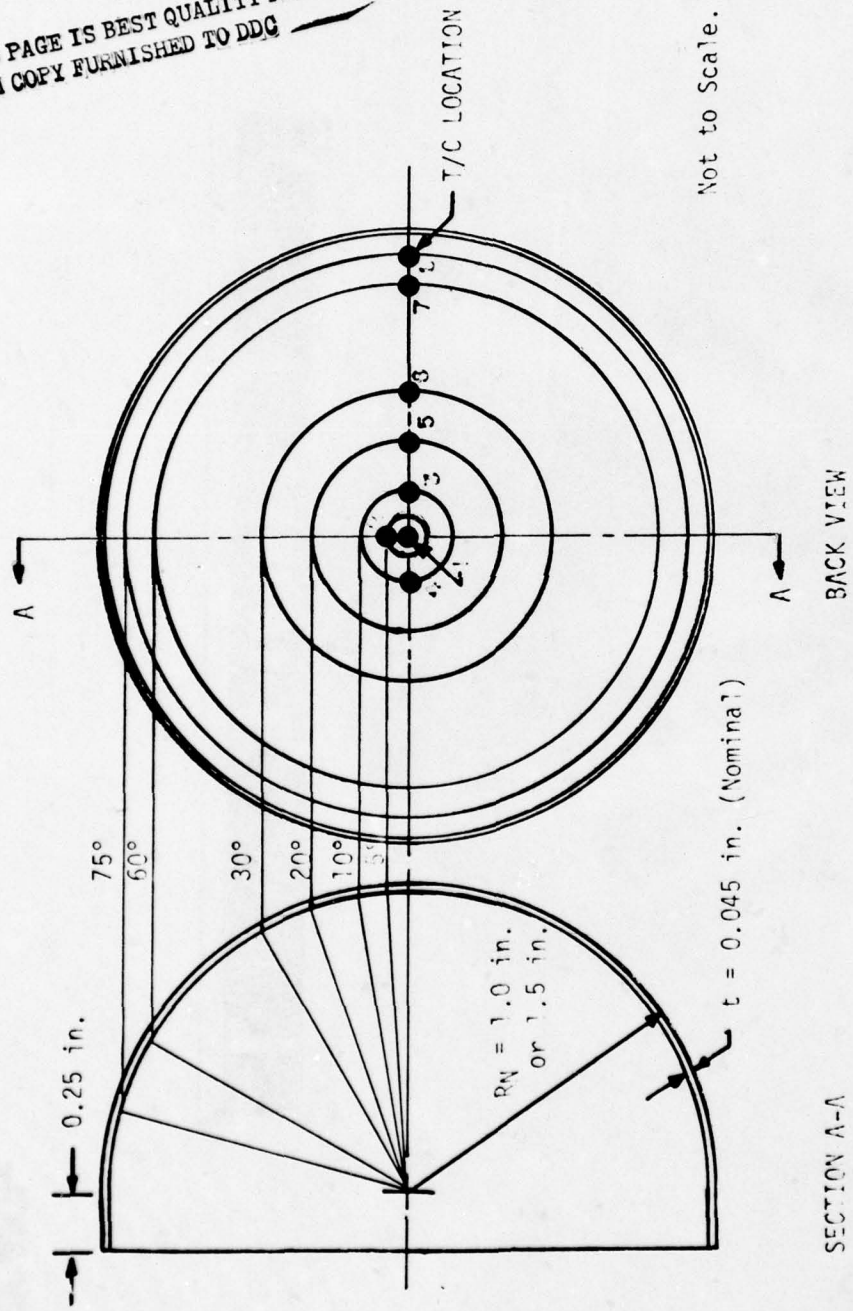
FIGURE 3-11. HEMISPHERE MODEL DESCRIPTION

3-24

TABLE 3-2. PRE-TEST TITANIUM HEMISPHERE THICKNESSES (INCHES)

MODEL NO.	LOCATION ON MODEL (POSITION/ANGLE)							
	1 0°	2 5°	3 10°	4 10°	5 20°	6 30°	7 60°	8 75°
Ti-1	.051	.049	.047	.047	.045	.042	.037	.036
Ti-2	.046	.045	.043	.043	.042	.037	.035	.035
Ti-3	.047	.045	.045	.044	.043	.042	.037	.037
Ti-4	.050	.048	.047	.047	.045	.042	.036	.035
Ti-5	.041	.039	.038	.037	.038	.036	.036	.037
Ti-6	.043	.042	.040	.039	.039	.038	.035	.038
Ti-7	.050	.048	.047	.048	.046	.044	.041	.041
Ti-8	.052	.051	.049	.049	.048	.044	.040	.037
Ti-9	.033	.032	.031	.032	.030	.031	.033	.037
Ti-10	.046	.044	.043	.043	.043	.038	.036	.035
Ti-11	.042	.040	.038	.038	.039	.037	.036	.036
Ti-12	.044	.042	.041	.041	.040	.038	.032	.033
Ti-13	.043	.040	.040	.038	.039	.037	.035	.036
Ti-14	.049	.047	.045	.046	.044	.040	.038	.037
Ti-15	.049	.047	.045	.046	.045	.042	.037	.037
Ti-16	.046	.044	.045	.045	.045	.046	.047	.047
Ti-17	.049	.049	.048	.047	.050	.046	.038	.036
Ti-18	.050	.049	.049	.048	.050	.046	.038	.037
Ti-22	.039	.038	.038	.039	.038	.034	.039	.042
Ti-23	.047	.044	.044	.043	.042	.042	.045	.048
Ti-53	.079	.078	.080	.079	.083	.082	.081	.075
Ti-54	.065	.066	.067	.066	.068	.070	.076	.079
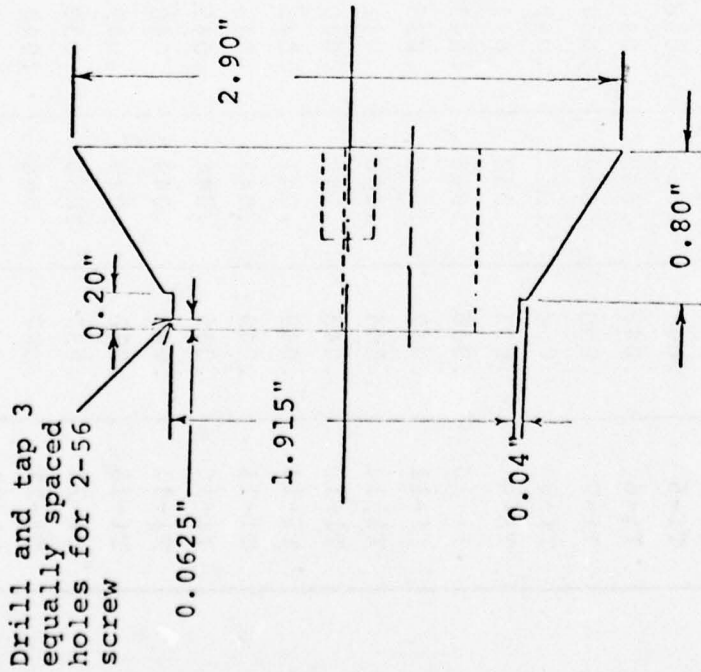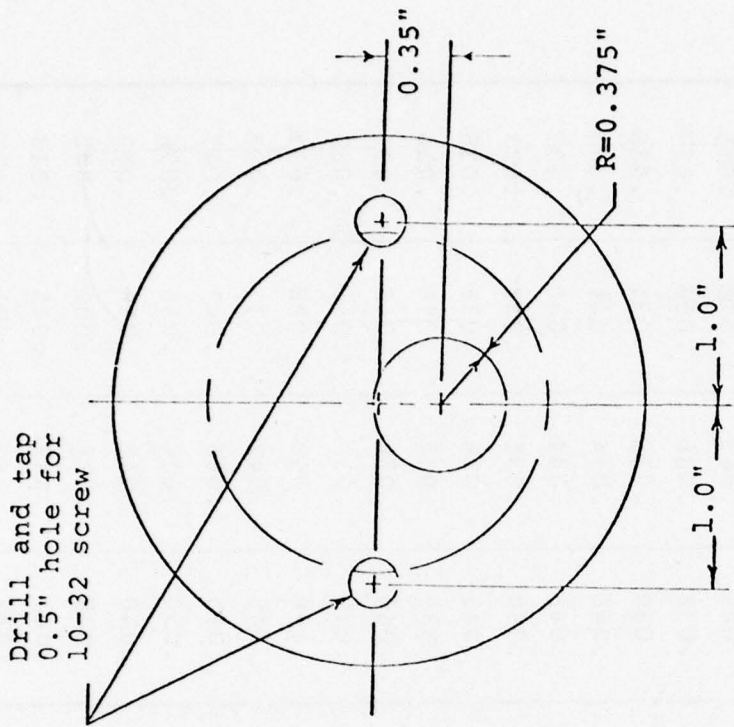
FIGURE 3-12. SKETCH OF MODEL HOLDER FOR THOSE MODELS
USING SPOT WELDED THERMOCOUPLES

1/16 OD Orifice Tube

R_N = 0.5 in.

1.0 in.

a. Pressure Probe

Type R Thermocouple (38 gauge wire) in 0.063 in. diam
Sheath. Sputtered Thin Film Junction

4 Holes 90 deg apart, 0.063 in. diam.

No. 78 Sauereisen Cement

Magnesia-Stabilized Zirconia,
1/4 OD x 3/16 ID

0.47

0.75

0.97

3.0
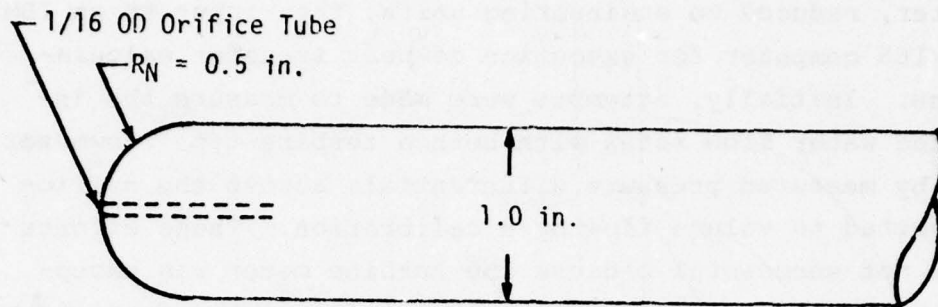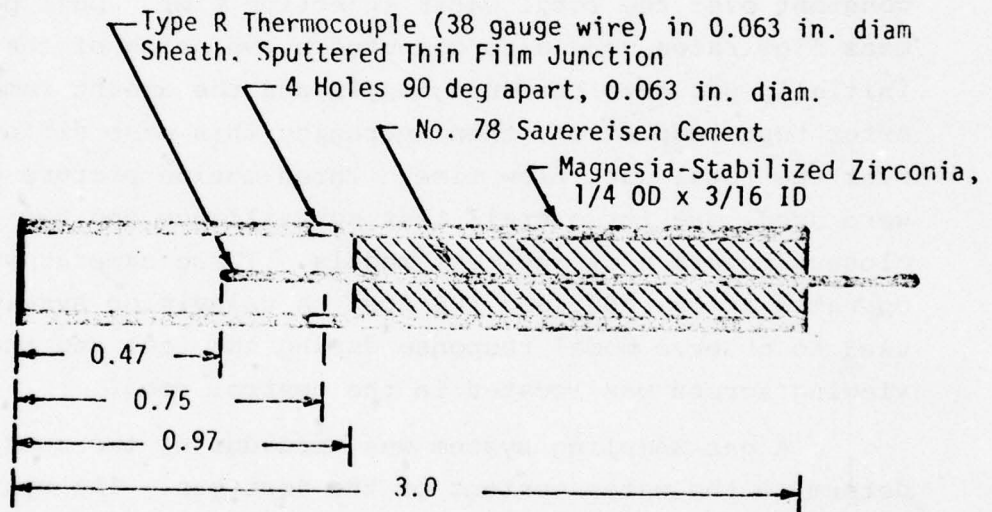
Not to Scale - All dimensions in inches.

b. Temperature Probe

FIGURE 3-13A&B. PRESSURE AND TEMPERATURE PROBES

recorded on magnetic tape using an analog-to-digital converter, reduced to engineering units, then input to an IBM 370/165 computer for execution of heat transfer calculations. Initially, attempts were made to measure the injected water flow rates with both a turbine-type flowmeter and by measured pressure differentials across the orifice converted to volume flow by a calibration. These efforts were not successful because the turbine meter was exceptionally susceptible in electrical noise pickup from the arc heater and the ΔP calibrations could not be performed under the same conditions as the orifices were subjected to during a test run. Beginning with Run 3, the water was weighed before and after the test run and the flow rate was assumed constant over the total water injection time. Dust particle mass flow rates were also computed by weighing of the dust initially put into the dust hopper and the amount remaining after test completion, then averaging this mass difference over the total dust flow time. Three motion picture cameras were used, one for overall test surveillance and two for closeup coverage of the test models. These cameras were operated at 50, 200, and 400 fps. A television system was used to observe model response during the test and the viewing screen was located in the control room.

A gas sampling system was used during two runs to determine the water content of the test gas. The system consisted of a 2 inch diameter stainless steel hemisphere with a 1/16 inch diameter sampling orifice at the stagnation point, two stainless steel bottles of 300 cc capacity each, and several valves and connecting stainless steel tubing (see Figure 3-14). The bottles were evacuated and dried prior to the tests. During operation, the sampling line from the model was purged, then the remotely operated valves were opened for about 10 seconds each. The remotely actuated

FIGURE 3-14. GAS SAMPLER MODEL
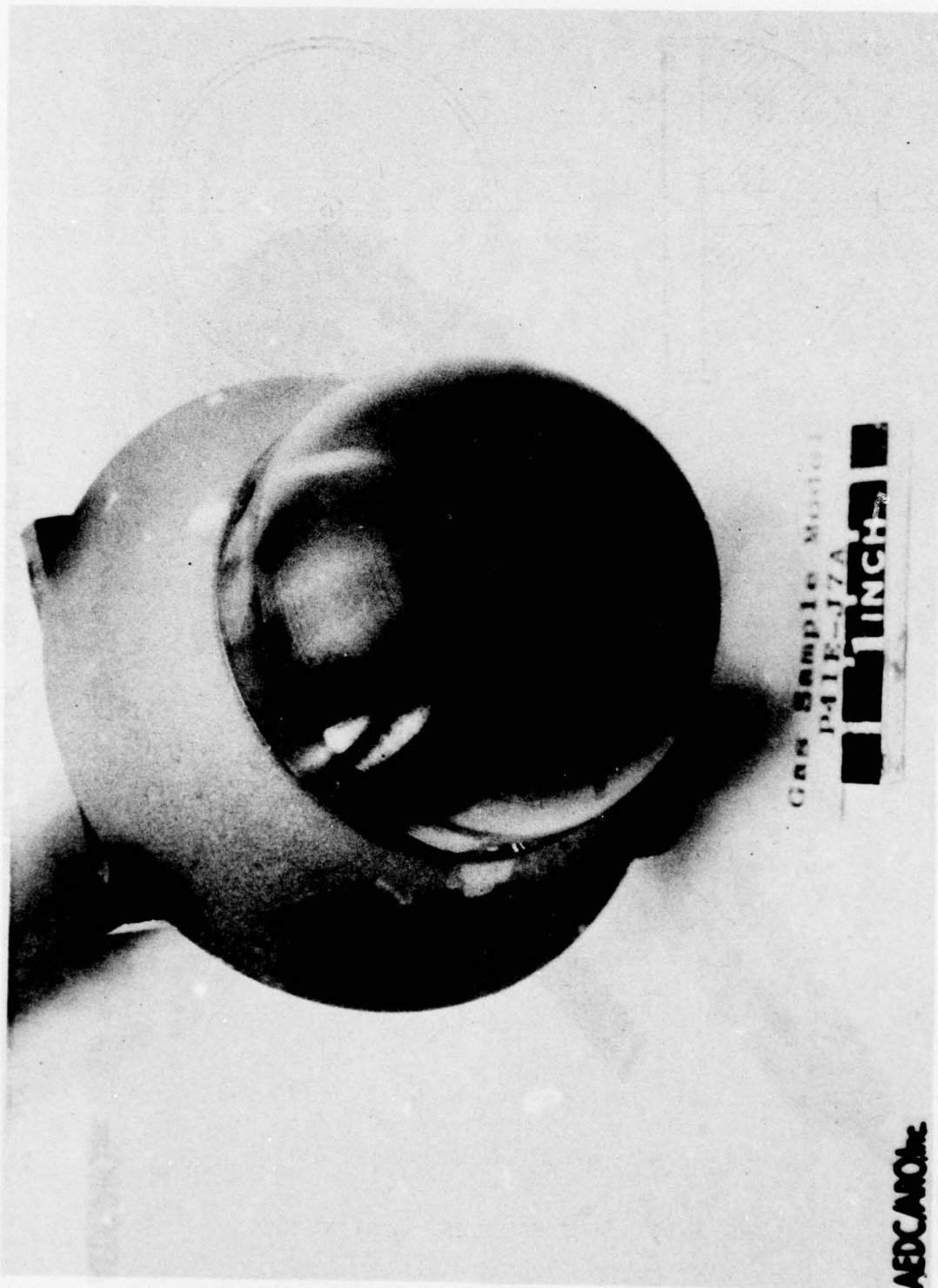
FIGURE 3-14. GAS SAMPLER MODEL (CONTINUED)
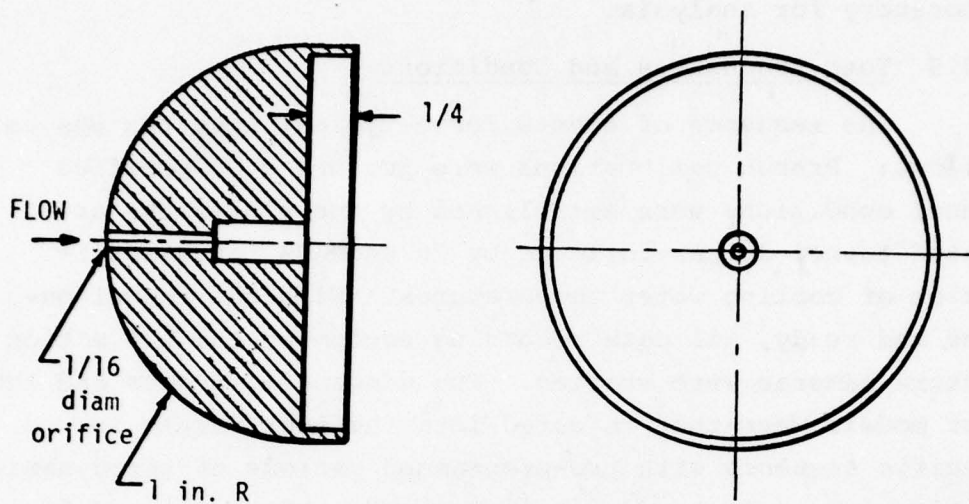
FIGURE 3-14. GAS SAMPLER (CONTINUED)
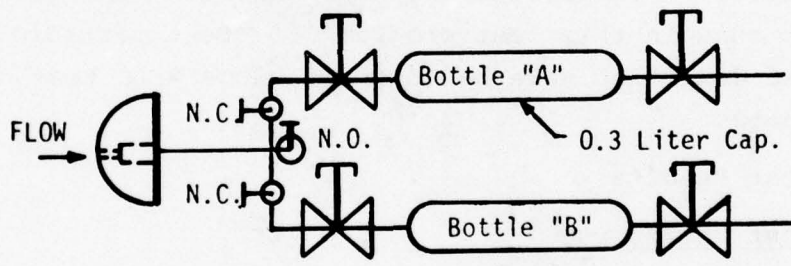
Hand Operated Valve

Electrically Operated,
Remotely Actuated Valve

N.O. - Normally Open

N.C. - Normally Closed

b. Schematic of Gas Sampling System

FIGURE 3-14. GAS SAMPLER (CONTINUED)

valves were then closed, and after the test run, the hand
valves were closed and the bottles sent to the AEDC Chemical
Laboratory for analysis.

3.3.5   Test Procedures and Conditions

The sequence of events for a typical test run was as
follows: Prerun calibrations were performed. Specified
tunnel conditions were established by energizing the arc-
heated tunnel driver followed by 20 seconds for stabili-
zation of cooling water temperatures. With the tunnel on-
line and ready, all data recording equipment and all motion
picture cameras were started. The diagnostic probes and the
test models were then injected into the test stream in
specific sequence with pre-programmed periods of aerodynamic
heating and/or dust and water exposure. After all models
had been cycled through the flow, the tunnel driver was de-
energized; then the postrun calibrations were performed.

Table 3-3 summarizes the AEDC DET test conditions for
the eight runs in this test program[7]. Dust particle velo-
cities and densities were based on previous AEDC test cali-
bration data.

3.4   Test Results

3.4.1   Test Philosophy

The objective of the DET tests was to demonstrate the
effects of water on titanium surface chemistry under particle
erosion conditions. The general approach to accomplish this
objective was to perform tests on titanium models under
varying conditions of clear air, dust, water and dust/water
environments. Comparisons of the performance of these model
responses were made to identify relative effects.

In each run, 9 stings were available for models or
instrumentation. Typically, these stings were occupied by
one pressure probe, one temperature probe, four models, and

TABLE 3-3. AEDC DET TEST CONDITIONS

RUN NO.	NO. MODELS	R_N (IN)	P_O (PSIA)	P_{stag} (PSIA)	H_O (BTU/LB)	T_{STAG} (°F)	$\dot{M}_{AIR}$ (LB/SEC)	$\dot{M}_{H_2O}$ (LB/SEC)	ρ_{DUST} (10^{-8} g/cc)	V_{DUST} (FT/SEC)	$\dot{e}_{DUST}$[†] (BTU/FT²-SEC)	GAS SAMPLER ΔM_{H_2O}[†] (mg)	GAS SAMPLER ΔM_{AIR} (mg)	Δt (SEC)
1						· · · · · CALIBRATION · · · · ·								
2	4	1.0	994	10	765	2430	2.9	.02	34	4600	41	—	—	—
3	4	1.0	1055	10	580	1809*	3.7	.04	45	4200	42	—	—	—
4	4	1.0	530	5.3	550	1702*	1.9	.35	34	4130	30	—	—	—
5	4	1.0	500	5.3	515	1568*	2.0	.04	39	4030	32	.76	116	25
6	4	1.0	994	9.4	780	2464*	2.7	.065	23	4560	27	4.0	194	20+
7	4	1.5	1002	9.8	1806	5440	1.7	.058	27	5530	57	—	—	—
8	4	1.0	1004	9.9	1865	5560	1.7	.048	18	5560	38	—	—	—

MODIFIED NOZZLE, STATION 127.5 INCHES, FOR ALL RUNS

* Temperature probe, all others based on mass-average enthalpy

† 100 μ MgO

witness bars or empty stings. For the high enthalpy runs,
no temperature probe was used since it would not survive.
In several runs, the gas sampler was used to measure water
content in the test gas.

Primary data was the model backface temperature
response. Attention was focused on the stagnation region
response. Comparisons of this temperature data and reduced
heat transfer data for the stagnation point were used to
determine the effect of water on the titanium response.

This test program encountered a number of problems in
the initial stages of testing related to facility cali-
bration and operation which were ultimately corrected. Part
of the difficulties were associated with the injection of
water which had never been attempted previously. It was
especially difficult to positively confirm the presence and
state of the water at the test section. Witness bars,
motion picture coverage, and ultimately the gas sampler
instrument were used to confirm the presence and/or amounts
of water at the test section. Originally, four runs were
planned with a required expansion to eight runs to accomp-
lish the objectives of the program.

The detailed test data results for Runs 2-8 are
presented in Appendix A. Run 1 was for calibration purposes
and is not discussed in this report. The basic data shown
in Appendix A includes: (1) post-test model photographs;
(2) total temperature probe trace (if available); (3) model
backface temperature measurements for all thermocouple loca-
tions; and, (4) reduced heat transfer data for all thermo-
couple locations. A discussion of the stagnation point
results of Runs 2-8 is presented in the following section.

3.4.2 Discussion of AEDC DET Runs

Figures 3-15 - 3-21 present the results of AEDC DET
Runs 2-8. The backface stagnation point thermocouple temper-
ature-time response and reduced heat transfer are shown for

each of the models tested. Runs 2-6 models were 2-inch
diameter and Runs 7-8 models were 3-inch diameter titanium
(6Al-4V) hemispheres of varying skin thicknesses -- model
numbers and stagnation point skin thicknesses are noted on
the figures. Test conditions including the dust and water
environments are shown. In most cases, stagnation pressure
and temperature were measured with probes except for Run 2,
where the temperature probe did not operate correctly and
the reported value is based on an energy balance and Runs 7
and 8 which were high enthalpy where the probe would not
survive.

Figures 3-15 and 3-16 show the results for the ini-
tial Run 2 with nominal flow conditions of 1000 psia total
pressure and 800 Btu/lb total enthalpy and a low water
injection rate. These results show the expected clear air
and dust response including the high temperature (>2200°R)
chemistry effect based on previous studies (Reference 4).
No increased effect of water is shown. The higher temper-
atures for the dust/water model Ti-6 compared to the dust
model Ti-1 result from a thinner skin only. In fact, no
effect of water, even a cooling effect, is shown. Figure 3-
16 shows the reduced heat transfer rate at the stagnation
point. This reduced data is characterized by: (1) an
initial transient increase to the ∿1000-1500°R regime; (2) a
decreasing heat transfer with increasing temperature char-
acteristic of a convective heating trend in the ∿1500-2000°R
regime; (3) an increasing heat transfer with increasing
temperature in the >2200°R regime characteristic of a dom-
inating surface chemistry effect; and, (4) periodic eratic
behavior due to electrical noise in the thermocouple output.
Typically, 2000°R is an excellent temperature to compare
relative heat transfer. Figure 3-16 shows no increased
effect of water and, in fact, possibly a reduced heat trans-
fer for the dust and water model. This run did not have the

FIGURE 3-15.   STAGNATION POINT RESULTS FOR AEDC DET RUN 2

MODEL TI-7 WATER
Time = 42.97 to 48.00 Sec

↓ 0 DEG TC #1

MODEL TI-6 DUST AND WATER
Time = 36.07 to 38.20 Sec

↓ 0 DEG TC #1

MODEL TI-5 CLEAR
Time = 16.06 to 22.60 Sec

↓ 0 DEG TC #1

MODEL TI-1 DUST
Time = 27.23 to 30.30 Sec

↓ 0 DEG TC #1
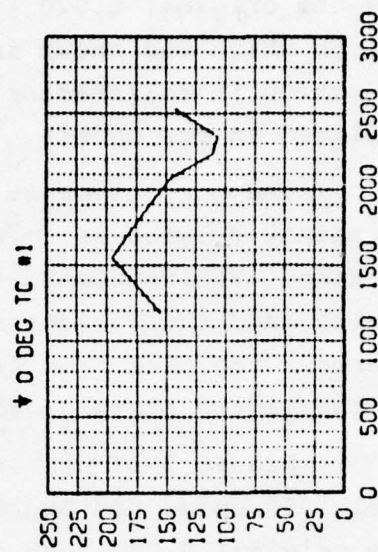
CORRECTED HEAT TRANSFER, BTU/FT² SEC

MODEL SURFACE TEMPERATURE (°R)

FIGURE 3-16. STAGNATION POINT (0 DEGREES, TC #1) HEAT TRANSFER FOR RUN 2

3-37

gas sampler in operation, so no direct evidence exists to prove that water actually impinged on the model. This run was the original 0.020 inch straight-through water orifice design which was shown in Section 3.3.2 to atomize water on injection in calibration tests; and thus, no water may have impinged on the model!

The conclusion at this point was that a large uncertainty existed as to the presence of water at the test section. The recommendation was to reduce the total enthalpy (and thus, the tendency for water vaporization) and increase the mass flow of H_2O to attempt to retain the water in the liquid state at the test section.

Figure 3-17 presents the results for the Run 3 nominal 1000 psia, 500 Btu/lb conditions. This run again used the original 0.020 inch straight-through orifice design but more water was injected than on Run 2. In this case, there is some evidence of a slight cooling effect of the water. The dust only model shows a chemistry effect above 2000°F as expected. No chemistry effect due to the water is evident up to 2000°F in this run. The conclusion at this point was again a lack of firm evidence that water was present in the test section. The recommendation was to increase the size of the orifice to obtain higher water mass flow rates and to reduce the total pressure to maximize the potential survival of the water during acceleration by the air flow.

Figure 3-18 presents the results for the Run 4 nominal 500 psia, 500 Btu/lb conditions. The 0.0625 inch straight-through orifice design was used to inject a larger quantity of water. The clear air and dust only response was as expected. However, the water only and dust/water models experienced massive quenching. These models did not reach temperatures where chemistry would be expected to be a factor.

STAGNATION POINT THERMOCOUPLE

○ Ti-10 (.046") CLEAR AIR
□ Ti-11 (.042") H_2O
△ Ti-5 (.041") DUST
◇ Ti-8 (.052") DUST/H_2O

OPEN: CLEAR
SOLID: DUST ON
FLAG: H_2O ON

.020" STRAIGHT-THROUGH ORIFICE
DESIGN

RUN 3

MODIFIED NOZZLE
2-INCH DIAMETER MODELS

P_{STAG}=10.07 psi (P_O=1055 psia)
T_{STAG}=1309°F (H_O=580 Btu/lb)
$\dot{M}_{AIR}$ =3.68 lb/sec
$\dot{M}_{H_2O}$ = .042 lb/sec
ρ_{DUST}=45(10^{-8}) g/cc
V_{DUST}=4200 fps

MODEL BACKFACE TEMPERATURE (°F)

TIME FROM MODEL INJECTION (SEC)
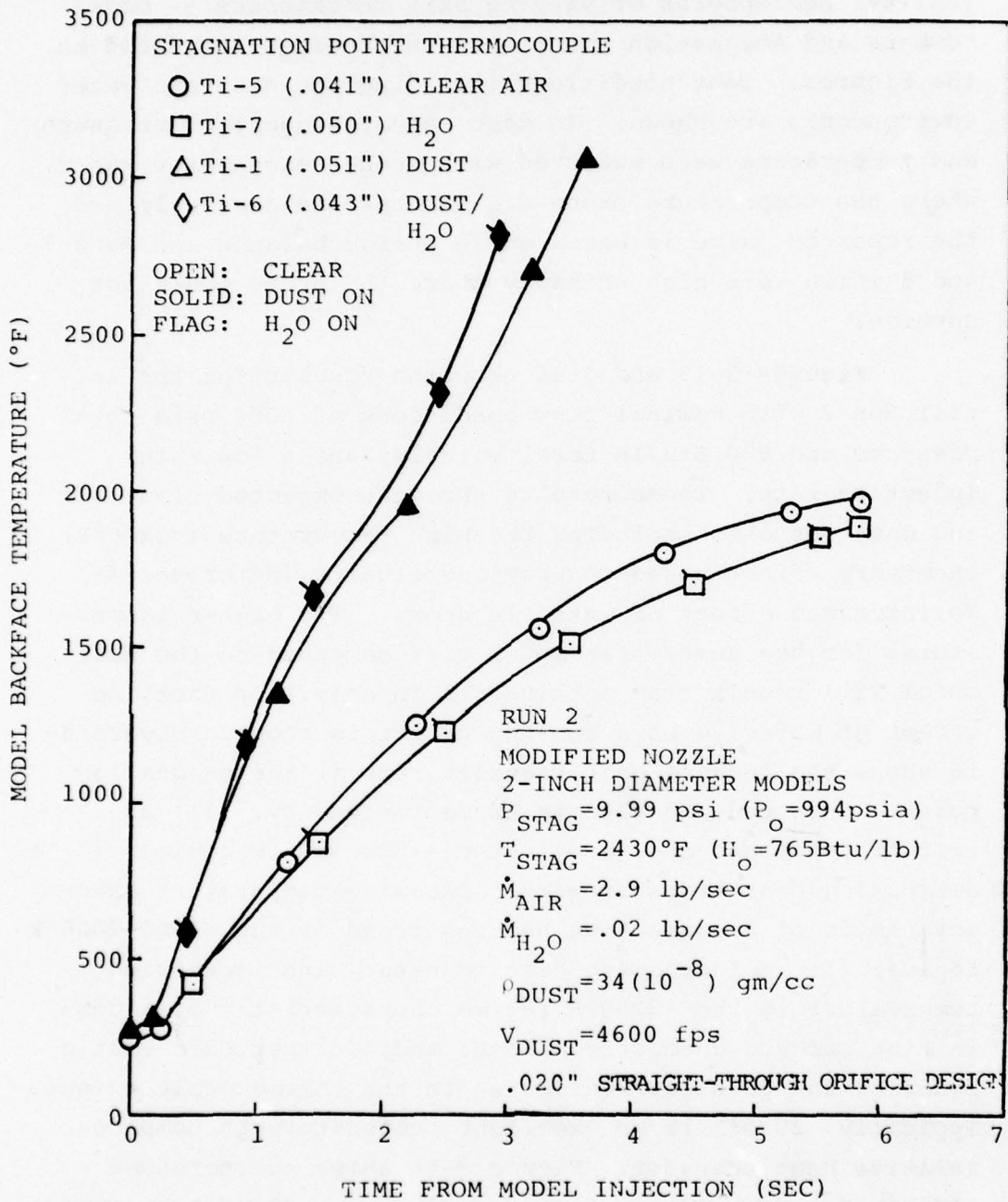
FIGURE 3-17. STAGNATION POINT RESULTS FOR AEDC DET RUN 3

3-39
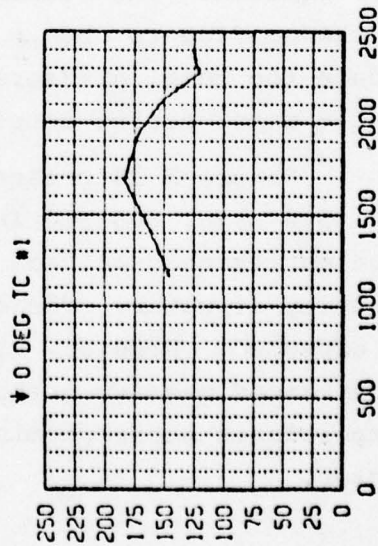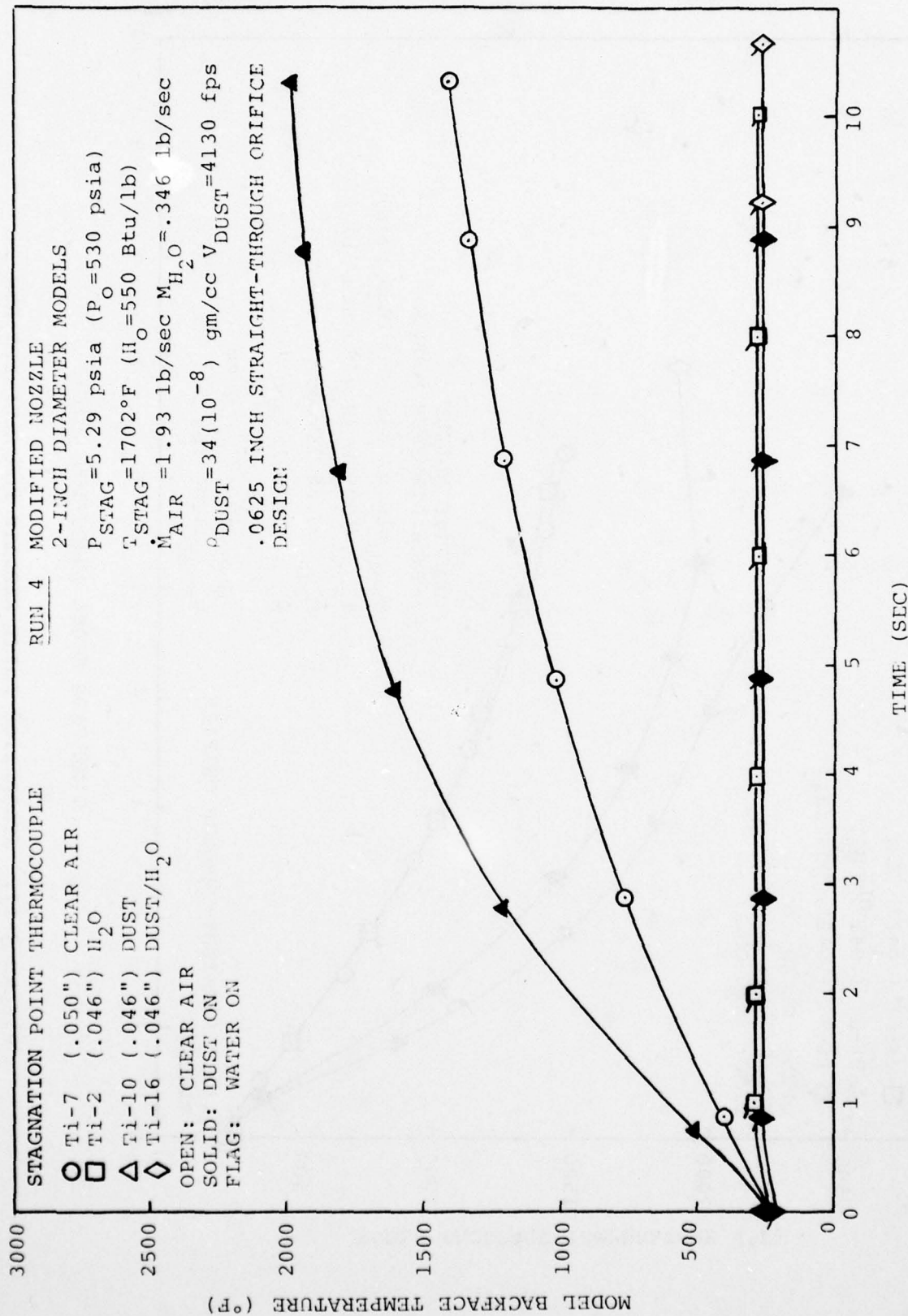
FIGURE 3-18. STAGNATION POINT RESULTS FOR AEDC DET RUN 4

The recommendation at this point was to perform the extensive bench calibration tests of the water orifice as described in Section 3.3.2 to arrive at a better orifice design prior to repeating the previous test conditions. In addition, the gas sampler was designed and implemented to quantify the water content of the gas.

Figures 3-19 and 3-20 present the results for the Run 5 nominal 500 psia, 500 Btu/lb conditions. This run used the 0.020 inch counterbored orifice design to attain a lower water injection rate and to reduce the dispersion of the water jet as it emerged from the orifice. This run used the gas sampler model. The primary purpose for collecting gas samples was to measure the total water content in the sample to allow a comparison of the water/air mass ratio of the sample to the water/air ratio determined by flow rate measurements. Two samples were collected during each run: one sample was analyzed for total water content and the other for species components. Water content was determined by Karl-Fisher titration and component analysis by use of a gas chromatograph. The results of the water content and component analyses are given in Table 3-4. For Run 5, the water/air mass ratio of injected water was 1.54×10^{-2}, and the water/air ratio of the sample was 6.54×10^{-3} or 42.5 percent of the injected value. The test procedure was also changed for Run 5 compared to preceding runs. Here, the models with water were preheated with clear air or dust to high temperature prior to water injection.

Figure 3-20 shows the heat transfer rate at 1500°R to be reduced from 20 Btu/ft^2 sec for clear air to 5 Btu/ft^2 sec for the water only model (water was introduced at ∿1300°R). Note that dust was inadvertently turned on and accounts for the high temperature "turn-around" in heat transfer rate for
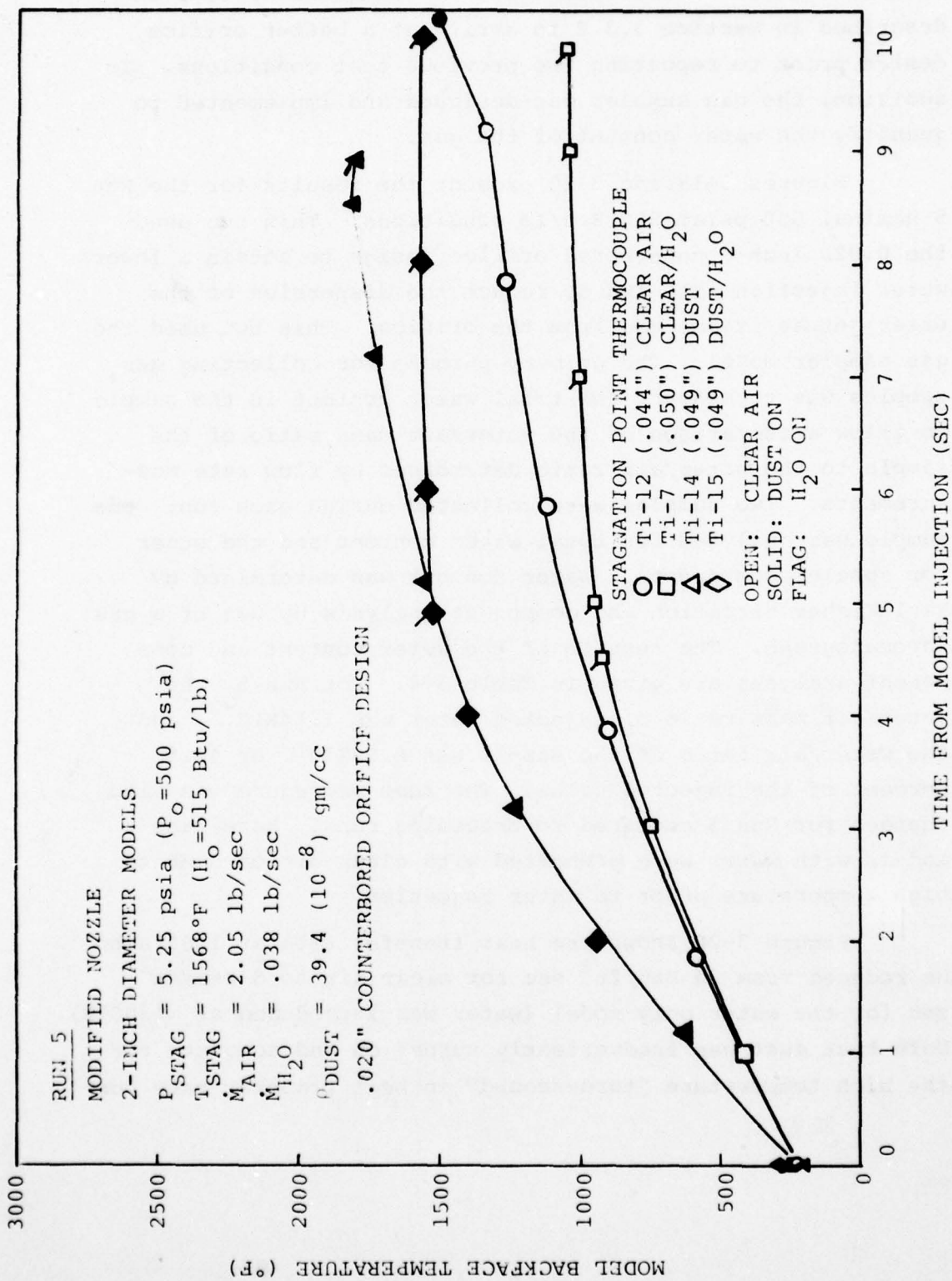
FIGURE 3-19. STAGNATION POINT RESULTS FOR AEDC DET RUN 5
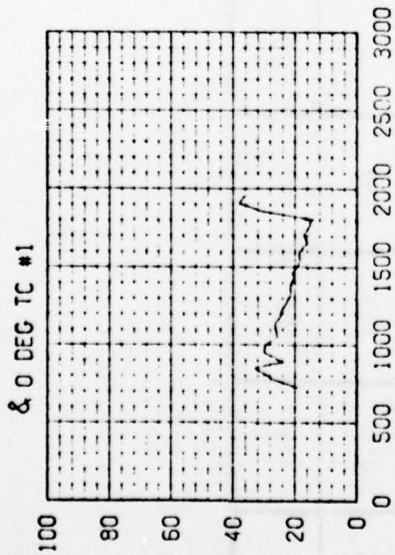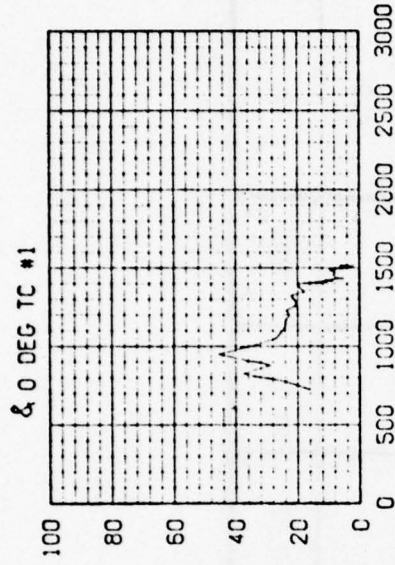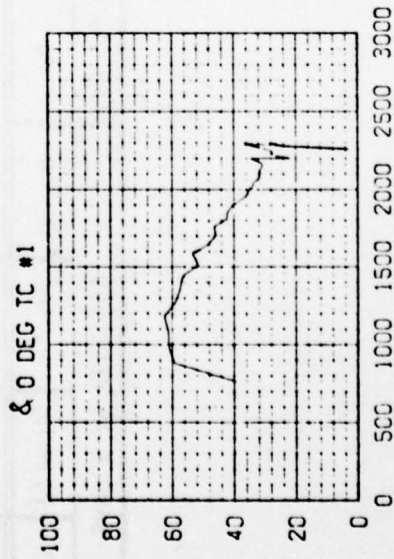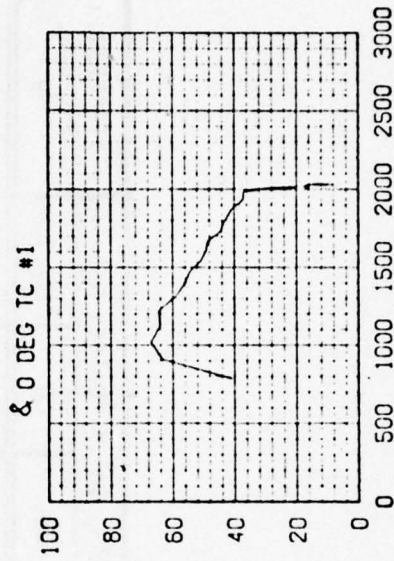
FIGURE 3-20. STAGNATION POINT HEAT TRANSFER FOR RUN 5

TABLE 3-4.

RESULTS OF GAS SAMPLE ANALYSIS

SAMPLE AS RECEIVED					GAS CHROMATOGRAPH CONSTITUENTS, Vol.% (Unless Noted)						TITRATION, TOTAL H_2O, mg
RUN	ID	P, mm Hg	V, cm³	T, °R	He	O_2 + Ar	N_2	CO_2	CO	NO_X, ppm	
5	A	237	300	534	0.02	20.08	78.08	0.07	0.01	2652	-
5	B	247	300	534	-	-	-	-	-	-	0.76
6	A	416	300	537	-	-	-	-	-	-	4.0
6	B	415	300	537	<0.01	19.89	80.15	0.07	<0.01	10323	-

the clear air model. Examination of the dust and the dust and water model responses also shows a cooling effect. Water was introduced at the end of the dust only model run and accounts for the significant heat transfer reduction at $\sim2200°R$. Water was introduced at $\sim2000°R$ on the dust and water model and accounts for the significant heat transfer reduction observed. No chemistry effect of water is observed for these models which experienced bulk temperatures to $\sim2000°R$.

The preliminary conclusion at this point was that, since water was confirmed at the test section, there is no net effect of water on titanium surface chemistry, at least up to $\sim2000°R$ temperatures. The recommendation was to simulate higher total enthalpies to confirm or deny this preliminary conclusion.

Figures 3-21 and 3-22 present the results for the Run 6 nominal 1000 psia, 800 Btu/lb conditions. The 0.020 inch counterbored orifice design was used. This run was a repeat of Run 2 except the dust concentration is lower and the water injection rate is higher. This run also had the gas sampler which showed that water was impinging on the model. For Run 6, the water/air ratio injected was 1.99×10^{-2}, and the water/air ratio for the sample was 2.06×10^{-2} or 103.4 percent of the injected value. These results for the 5 degree off-stagnation thermocouple location show the expected surface chemistry effect for the dust only model above $\sim2200°R$. The effect of adding water is shown to be a net cooling effect for both the water only and dust/water model. The preliminary conclusion was that water does not augment the surface chemistry for this intermediate total enthalpy flow condition. The recommendation was to conduct a high enthalpy flow run to further confirm or deny this preliminary conclusion.

NEAR STAGNATION POINT THERMOCOUPLE (5 DEGREE LOCATION)

- ○ Ti-12 (.042") CLEAR AIR
- □ Ti-2 (.046") CLEAR/H_2O
- △ Ti-13 (.043") DUST
- ◇ Ti-11 (.042") DUST/H_2O

OPEN: NO DUST

SOLID: DUST ON

FLAG: H_2O ON

RUN 6

MODIFIED NOZZLE
2-INCH DIAMETER MODELS

P_{STAG} = 9.43 psia (P_O=994 psia)

T_{STAG} = 2464°F (H_O=780 Btu/lb)

$\dot{M}_{AIR}$ = 2.72 lb/sec

$\dot{M}_{H_2O}$ = .065 lb/sec

ρ_{DUST} = 23.4 (10^{-8}) gm/cc

.020" COUNTERBORED ORIFICE DESIGN

FIGURE 3-21.   STAGNATION POINT RESULTS FOR AEDC DET RUN 6
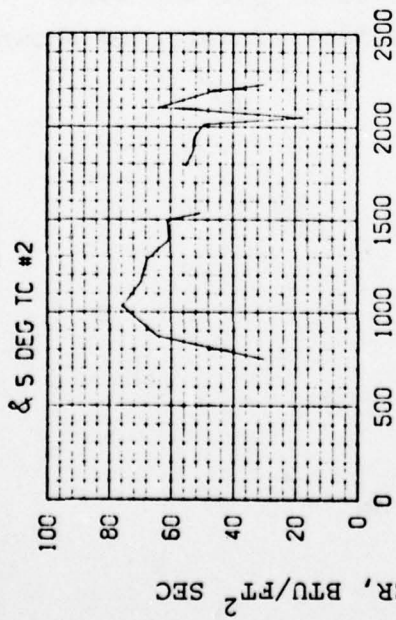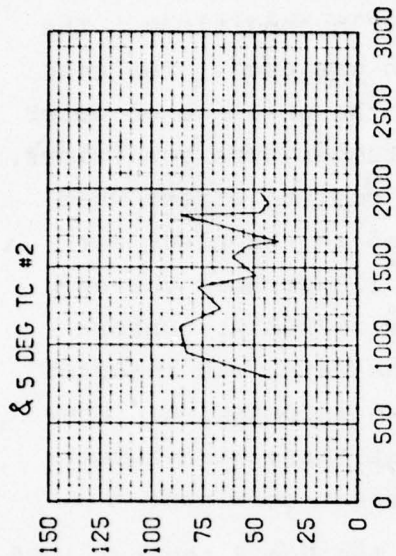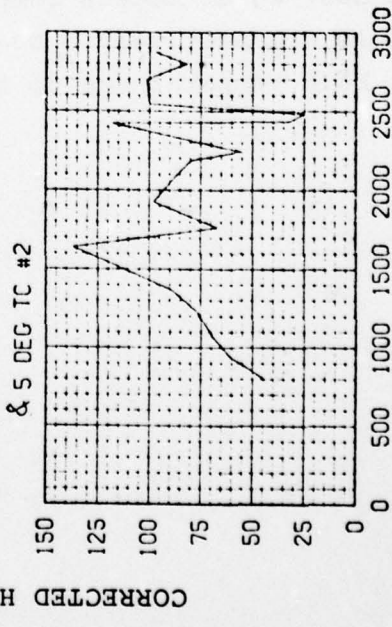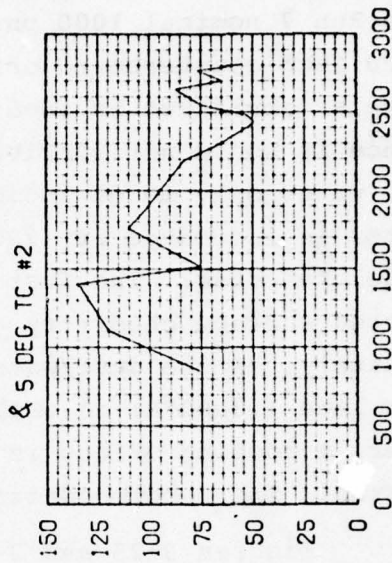
FIGURE 3-22. STAGNATION POINT (5° LOCATION) HEAT TRANSFER FOR RUN 6

Figures 3-23 and 3-24 present the stagnation point backface temperature and surface heat transfer results for the Run 7 nominal 1000 psia, 1800 Btu/lb conditions. The .020 inch counterbored orifice design was used. The gas sampler could not be used to confirm the presence of water since it would not survive the high temperature conditions. The water only model indicates a net cooling effect when water is initiated at $\sim$2500°R compared to the clear air model response. The dust only model illustrates the expected surface chemistry effects above $\sim$2200°R. Unfortunately, on the dust/water model, the water was injected too late ($\sim$3000°R) to obtain extensive information. However, a cooling effect is suggested at these high temperatures. The recommendation was to repeat this run.

Figures 3-25 and 3-26 present the Run 8 nominal 1000 psia, 1800 Btu/lb results for the repeat of Run 7. Test conditions were essentially identical to Run 7 except that 2.0 inch models were used. Again, the gas sampler could not be used. The results show the same increased surface chemistry from dust above $\sim$2200°R. A decreased heat transfer effect of water is shown in Figure 3-26 for both the water and dust/water models compared to the clear air and dust models, respectively. No increased effect of water is shown for bulk temperatures up to $\sim$3000°R.

STAGNATION POINT THERMOCOUPLE

⊙ Ti-22 (.039") CLEAR AIR
▣ Ti-23 (.047") H_2O
△ Ti-54 (.065") DUST
◇ Ti-53 (.079") DUST/H_2O

OPEN: CLEAR AIR
SOLID: DUST ON
FLAG: H_2O ON

RUN 7 MODIFIED NOZZLE
3-INCH DIAMETER MODELS

P_{STAG} = 8.43 psia (P_O = 1002 psia)
T_{STAG} = 5440°F (H_O = 1806 Btu/lb)
$\dot{M}_{AIR}$ = 1.71 lb/sec
$\dot{M}_{H_2O}$ = .058 lb/sec

ρ_{DUST} = 26.6 (10^{-8}) gm/cc

(100μMgO, V=5530 fps)

.020" COUNTERBORED ORIFICE DESIGN

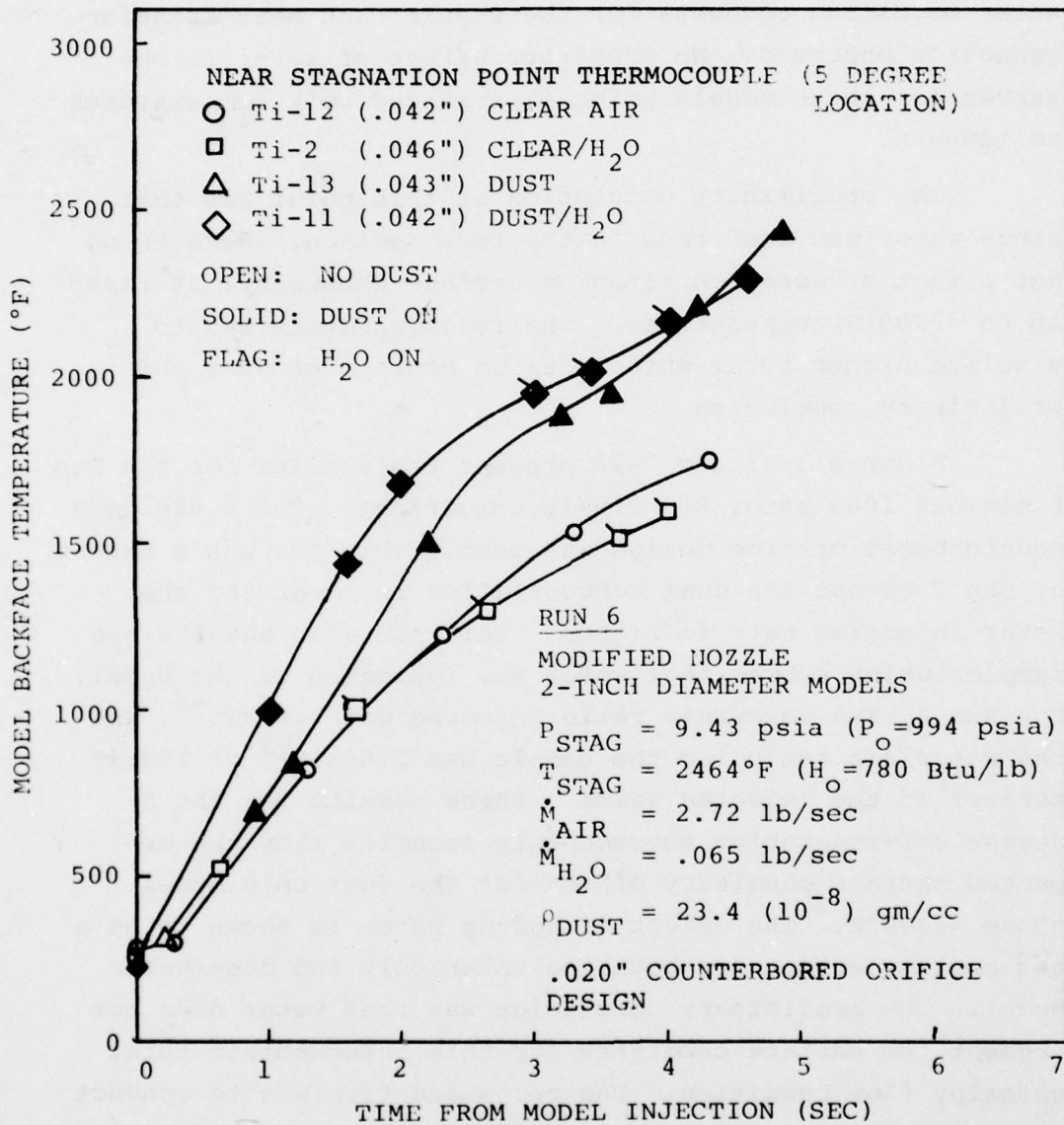MODEL BACKFACE TEMPERATURE (°F)

TIME FROM MODEL INJECTION (SEC)

FIGURE 3-23. STAGNATION POINT RESULTS FOR AEDC DET RUN 7

3-49

MODEL TI-23 WATER

Time = 32.65 to 38.50 Sec

& 0 DEG TC #1

MODEL TI-53 DUST AND WATER

Time = 26.01 to 29.70 Sec

& 5 DEG TC #2

MODEL TI-22 CLEAR

Time = 9.43 to 15.60 Sec

& 0 DEG TC #1
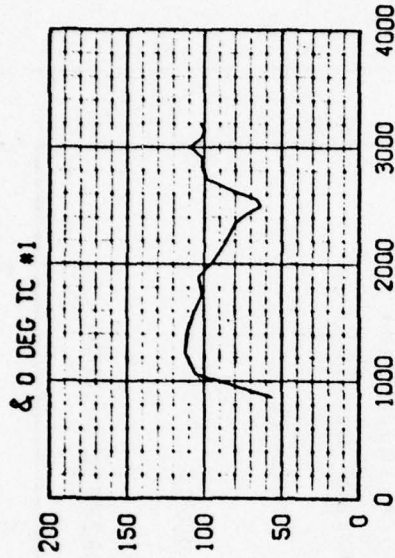
MODEL TI-54 DUST

Time = 20.96 to 23.50 Sec

& 5 DEG TC #2

MODEL SURFACE TEMPERATURE (°R)

CORRECTED HEAT TRANSFER, BTU/FT² SEC
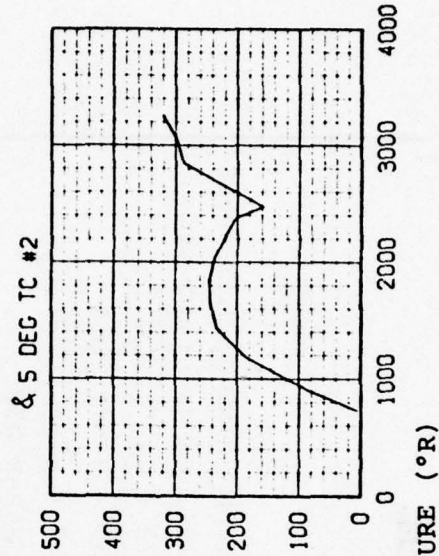
FIGURE 3-24. STAGNATION POINT HEAT TRANSFER FOR RUN 7

FIGURE 3-25.   STAGNATION POINT RESULTS FOR AEDC DET RUN 8
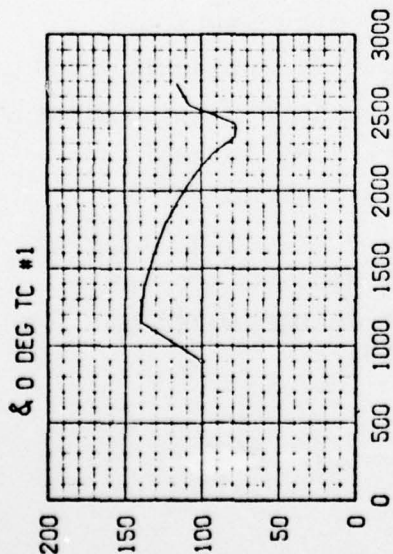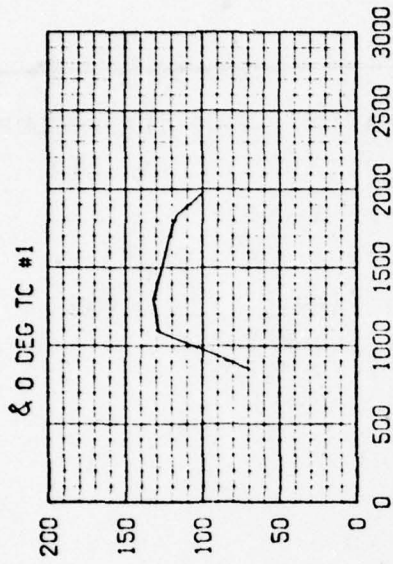
3-51
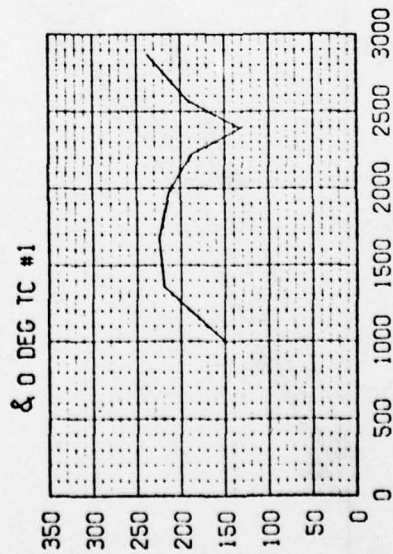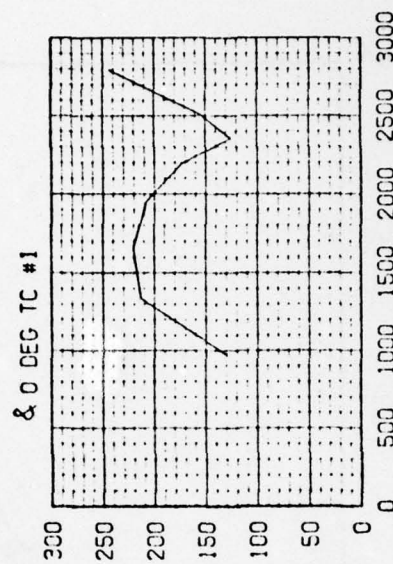
FIGURE 3-26. STAGNATION POINT HEAT TRANSFER FOR RUN 8
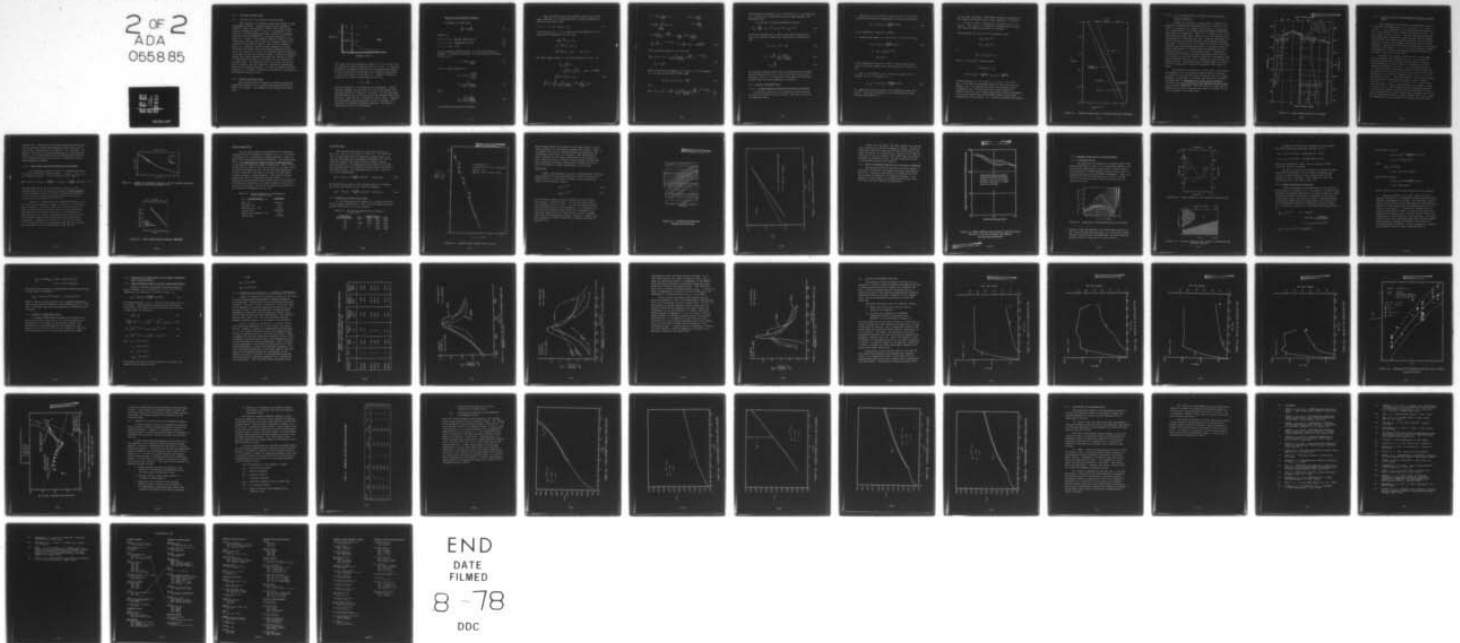
4.0 TITANIUM RESPONSE MODEL

4.1 Formulation of the Titanium Oxidation Model

The oxidation of titanium has been the subject of many experimental studies. Earlier work has been reviewed by Hauffe[8] (1965) and Kofstad[9] (1966); more recent work is briefly discussed by Wolf[10] (1975). At pressures of the order of 1 atm and temperatures above 600-700°C, experiment has shown that the oxidation is initially parabolic, i.e., mass gain $\sim$ (time)$^{\frac{1}{2}}$. The parabolic behavior regime is relatively long; the duration is about 500 minutes at 800°C, decreasing to 8 minutes at 1200°C. Thus for the problem at hand, i.e., modeling titanium nosetip response to nuclear cloud particle impact, where the surface obscuration times are of the order 0.1 to 1 sec, the oxidation can be considered to be wholly within the parabolic regime. During the parabolic regime, two oxygen consuming processes are observed to occur: (a) dissolution of oxygen in the metal, and (b) formation of an oxide scale. Our objective here is to review the literature to assemble the data required to develop an engineering model of the oxidation process. In order to identify the data required, it is helpful to present an introductory discussion of the proposed oxidation model.

4.1.1 Proposed Oxidation Model

The proposed model for parabolic oxidation postulates simultaneous formation of a compact scale and dissolution of oxygen in the metal. The schematic below depicts the situation.

$$\mathcal{D}_1 \qquad\qquad \mathcal{D}_2$$

C
MASS/VOL.

C_a

C_s

SCALE 1

C_u

METAL 2

ε

C_o

0

MATERIAL DEPTH - X
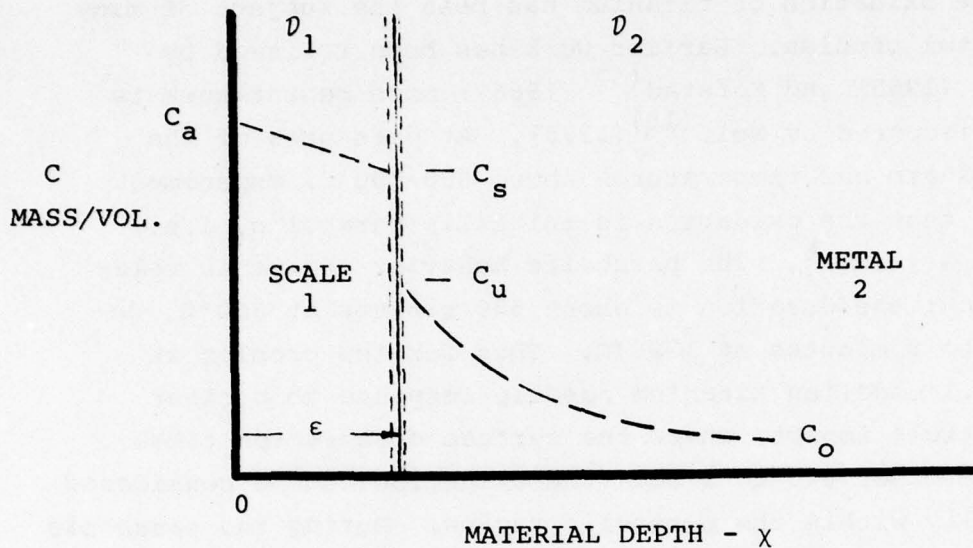
This model was first proposed by Wagner[11], and has been used to interpret zirconium oxidation data in (12,13). In these applications the model as been used in a semi-empirical fashion to avoid requiring the knowledge of the oxygen concentration at the outer surface of the scale, C_a. Instead a parabolic growth law for scale is postulated in the form

$$\varepsilon = 2\,\gamma\,\sqrt{\mathcal{D}_1 t}$$

where the constant γ is determined from experiment. Following this approach the next step is to solve the species conservation equation in region 2, the metal. In our final model for engineering use, this solution will be obtained numerically since $\mathcal{D}_2 = \mathcal{D}_2(T)$ and T is a function of both x and t. However, for the purpose of evaluating data in the literature, it is sufficient to consider isothermal oxidation, for which an analytical solution can be obtained.

Solution for Isothermal Oxidation

In Region 2 we must solve

$$\frac{\partial c}{\partial t} = \mathcal{D}_2 \frac{\partial^2 c}{\partial t^2} \tag{2}$$

subject to

$t = 0$, $c = c_o$,   assumed constant here $\tag{3}$

$x = \epsilon$, $c = c_u$,   independent of time $\tag{4}$

$x \to \infty$, $c = c_o = 0$ say $\tag{5}$

For this moving boundary problem, we follow the method of Neumann. A solution to Equation (2) which satisfies Equations (3) and (5) is

$$c = A \ \text{erfc} \ \frac{x}{2\sqrt{\mathcal{D}_2 t}} \tag{6}$$

at $x = \epsilon$, using Equation (4),

$$c_u = A \ \text{erfc} \ \frac{2\gamma\sqrt{\mathcal{D}_1 t}}{2 \ \sqrt{\mathcal{D}_2 t}}$$

$$A = \frac{c_u}{\text{erfc} \ \gamma \ \sqrt{\mathcal{D}_1 / \mathcal{D}_2}} \tag{7}$$

Thus

$$\frac{c}{c_u} = \frac{\text{erfc} \ \dfrac{x}{2\sqrt{\mathcal{D}_2 t}}}{\text{erfc} \ \gamma\sqrt{\mathcal{D}_1 / \mathcal{D}_2}} \tag{8}$$

is the desired concentration profile.

Next we postulate that the parabolic growth law for the scale, Equation (1) is associated with a linear concentration profile in the scale, then

$$0 < x < \varepsilon, \quad c = c_a - \frac{x}{\varepsilon} (c_a - c_s) \tag{9}$$

In the limit of $\mathcal{D}_2 \to 0$ it is easy to see that Equation (5) is consistent with Equation (1), for then

$$\rho \frac{d\varepsilon}{dt} = \frac{\mathcal{D}_1}{\varepsilon} (c_a - c_s)$$

$$\varepsilon d\varepsilon = \frac{\mathcal{D}_1}{\rho} (c_a - c_s) \, dt$$

$$\frac{\varepsilon^2}{2} = \frac{\mathcal{D}_1}{\rho} (c_a - c_s) t \qquad \text{or } \varepsilon \, \alpha \, \sqrt{t}$$

The total oxygen present in the scale and metal at time t is

$$M_{O_2} = \int_0^\infty c \, dx$$

$$= \int_0^\varepsilon c \, dx + \int_\varepsilon^\infty c \, dx \qquad \text{with } \varepsilon = 2\gamma \sqrt{\mathcal{D}_1 t}$$

$$\int_0^\varepsilon c \, dx = \frac{1}{2} (c_a + c_s) \varepsilon \tag{10}$$

$$\int_\varepsilon^\infty c \, dx = \int_\varepsilon^\infty \left\{ \frac{c_u}{\operatorname{erfc} \gamma \sqrt{\mathcal{D}_1/\mathcal{D}_2}} \quad \operatorname{erfc} \frac{x}{2\sqrt{\mathcal{D}_2 t}} \right\} dx$$

$$= A \quad \text{erfc} \frac{x}{2\sqrt{\mathcal{D}_2 t}} \quad dx \qquad\qquad \text{Let } \eta = \frac{x}{2\sqrt{\mathcal{D}_2 t}}$$

$$= A \; 2\sqrt{\mathcal{D}_2 t} \int_{\frac{\varepsilon}{2\sqrt{\mathcal{D}_2 t}}}^{\infty} \text{erfc } \eta \; d\eta \qquad\qquad d\eta = \frac{dx}{2\sqrt{\mathcal{D}_2 t}}$$

$$= A \; 2\sqrt{\mathcal{D}_2 t} \left[\frac{1}{\sqrt{\pi}} \, e^{-\frac{\varepsilon^2}{4\mathcal{D}_2 t}} - \frac{\varepsilon}{2\sqrt{\mathcal{D}_2 t}} \; \text{erfc} \; \frac{\varepsilon}{2\sqrt{\mathcal{D}_2 t}} \right]$$

$$= A \left[2 \; \frac{\mathcal{D}_2 t}{\pi} \, e^{-\gamma^2 \mathcal{D}_1/\mathcal{D}_2} - 2\gamma \sqrt{\mathcal{D}_1 t} \; \text{erfc} \; \gamma \sqrt{\mathcal{D}_1/\mathcal{D}_2} \right] \tag{11}$$

Thus, combining Equations (10) and (11),

$$M_{O_2} = \frac{1}{2}(c_a + c_s) + \frac{c_u}{\text{erfc } \gamma \sqrt{\mathcal{D}_1/\mathcal{D}_2}} \; 2\sqrt{\frac{\mathcal{D}_2 t}{\pi}} \; e^{-\gamma^2 \mathcal{D}_1/\mathcal{D}_2}$$

$$- c_u \, 2\gamma \sqrt{\mathcal{D}_1 t} \tag{12}$$

Next we eliminate the unknown c_a in favor of γ; if we assume $c_a \simeq c_s$ this is particularly easy, then

$$\frac{1}{2}(c_a + c_s)\varepsilon = c_s \, 2\gamma \sqrt{\mathcal{D}_1 t} \tag{13}$$

and

$$M_{O_2} = (c_s - c_u) \, 2\gamma \sqrt{\mathcal{D}_1 t} + \frac{c_u}{\text{erfc } \gamma \sqrt{\mathcal{D}_1/\mathcal{D}_2}} \; 2\sqrt{\frac{\mathcal{D}_2 t}{\pi}} \; e^{-\gamma^2 \mathcal{D}_1/\mathcal{D}_2} \tag{14}$$

4-5

which agrees with Equation (21) in Reference (9). The assumption $c_a \simeq c_s$ proves to be sufficiently good to make Equation (12) generally valid.

For the rate of oxygen consumption we write

$$\dot{M}_{O2} = \frac{dM_{O2}}{dt} = K_o \ t^{-1/2} = K_f \ t^{-1/2} + K_s \ t^{-1/2} \tag{15}$$

where rate constants K_o, K_f and K_s have been introduced for the total oxidation, oxide film, and solution, respectively. Thus

$$K_f = (c_s - c_u) \ \gamma \ \sqrt{\mathcal{D}_1} \tag{16}$$

$$K_s = c_u \sqrt{\frac{\mathcal{D}_2}{\pi}} \ \frac{e^{- \gamma^2 \mathcal{D}_1/\mathcal{D}_2}}{erfc \ \gamma \ \sqrt{\mathcal{D}_1/\mathcal{D}_2}} \tag{17}$$

$$\simeq c_u \ \sqrt{\frac{\mathcal{D}_2}{\pi}} \tag{18}$$

The preceding analysis shows that the parameters of the model are the concentrations c_a, c_s and c_u and the diffusion coefficients $\mathcal{D}_1$ and $\mathcal{D}_2$. In order to use the model for engineering analysis data for these parameters is required.

4.1.2 Survey of Available Data

4.1.2.1 $\mathcal{D}_2$ The Diffusion Coefficient of Oxygen in Titanium

Considerable data for $\mathcal{D}_2$ for unalloyed titanium exists, but data for titanium alloys is sparse. The most useful data is summarized below.

1. Kofstad et al (14) derived a value for $\mathcal{D}_2$ for unalloyed titanium neglecting the consequences of oxide film formation,

$$\mathcal{D}_2 = 0.5 \exp\left(-\frac{51,000}{RT}\right) \text{ cm}^2/\text{s} \tag{19}$$

in the temperature range 800 - 1200°c.

2. Shamblen and Redden (15) obtained for Ti-6Al-2Sn-4Zr-2M$_o$

$$\mathcal{D}_2 = \mathcal{D}_o \exp\left(-\frac{48,000}{RT}\right) \text{ cm}^2/\text{s} \tag{20}$$

$$\mathcal{D}_o = 147 \, [O_2 \text{ ppm}]^{-0.742}$$

$$\simeq 062 \text{ cm}^2/\text{s}$$

in the temperature range 300 - 870°C. These authors found that O_2 increases somewhat with substitutional alloying content.

3. Rosa (9) determined $\mathcal{D}_2$ for α-titanium from the rate of movement of the α-β interface as

$$\mathcal{D}_{2(\alpha)} = 0.778 \exp\left(-\frac{48,600}{RT}\right) \text{ cm}^2/\text{s} \tag{21}$$

for commerically pure titanium in the temperature range 932 - 1142°C. Rosa also determined $\mathcal{D}_2$ for β-titanium from micro-hardness measurements as

for the same conditions. Rosa makes favorable comparisons of his results with earlier data in the literature, (17,18,19).

Figure 4-1 shows a comparison of Equations (18, 19, 20 and 21). Also shown is a "corrected" Kofstad equation rederived from his oxidation rate data, as follows:

From Equations (13) and (17), for dissolution only.

$$\dot{M}_{O_2} = K_s \, t^{-1/2}$$

$$M_{O_2} = 2K_s \, t^{1/2}$$

or

$$M_{O_2}^2 = \frac{4}{\pi} \, c_u^{\,2} \, \mathcal{D}_2 t \equiv K_p \, t$$

For $c_u = 0.641$ gm/cm^3 (derived below)

$$0.523 \, K_p \, \mathcal{D}_2 = K_p$$

$$0.523 \, \mathcal{D}_o \, \exp \, (- \frac{51,000}{RT}) = A_p \, \exp \, (- \frac{51,000}{RT})$$

Kofstad obtained $A_p = 3.2$, thus $\mathcal{D}_o = 3.2/5.23 = 6.12$ cm^2/s which is an order of magnitude higher than the value given by Equation (19). We conclude that there is a numerical error in Equation (19). We also note that we would expect the Kofstad value of $\mathcal{D}_2$ to be higher than those of Rosa and Shamblen since in the former case it was assumed that all the oxygen consumed went into solution, i.e., the TiO_2 formation was ignored.
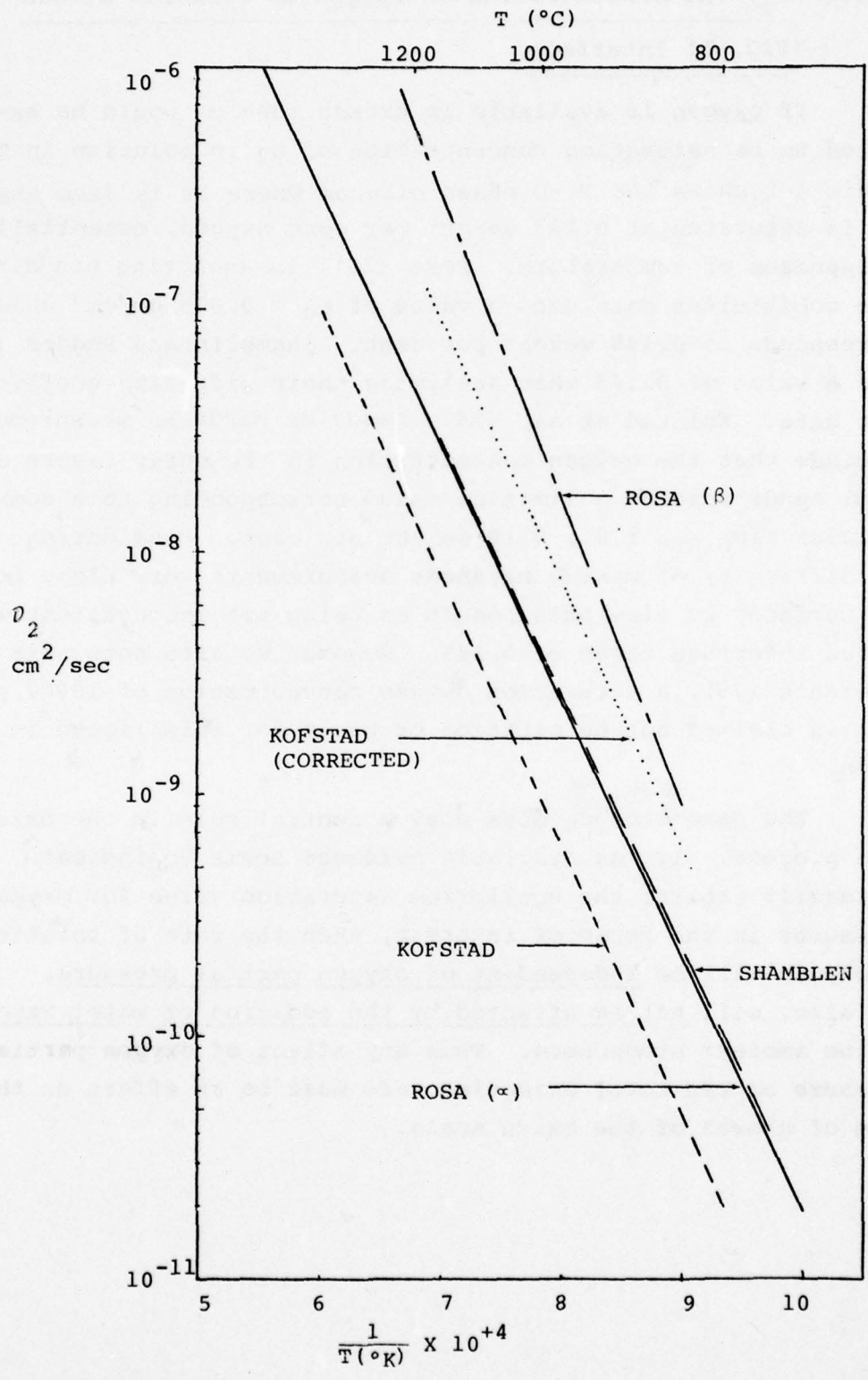
FIGURE 4-1.   DIFFUSION COEFFICIENT IN TITANIUM FROM THE LITERATURE

4-9

4.1.2.2 c_u, The Concentration of Oxygen in Titanium at the TiO$_2$-Ti Interface

If oxygen is available in excess then c_u would be expected to be saturation concentration of O_2 in solution in Ti. Figure 4-2 shows the Ti-O phase diagram where it is seen that αTi is saturated at 0.143 weight per cent oxygen, essentially independent of temperature. Rosa [16], in analyzing his diffusion coefficient data used a value of $c_u = 0.665$ gm/cm^3 which corresponds to 0.148 weight per cent. Shamblin and Redden [15] used a value of 0.143 when analyzing their diffusion coefficient data. Kofstad et al. [14], based on hardness measurements, conclude that the oxygen concentration in the outer layers of metal tends towards a limiting value corresponding to a composition TiO$_{0.35}$, i.e., 0.10 weight per cent. Considering the difficulty of making hardness measurements very close to the surface, we view this result as being not inconsistent with a true interface value of 0.143. However we also note that in Reference [20], a saturation oxygen concentration of 10.02 per cent is claimed but no citation or basis for this figure is given.

The parameter c_u does play a central role in the oxidation process. If, as available evidence seems to indicate, c_u readily attains the equilbrium saturation value for oxygen pressures in the range of interest, then the rate of solution of oxygen will be <u>independent of oxygen partial pressure</u>, and also, will <u>not be affected by the addition of water vapor</u> to the ambient atmosphere. Thus any affect of oxygen partial pressure on the total oxidation rate must be an effect on the rate of growth of the oxide scale.
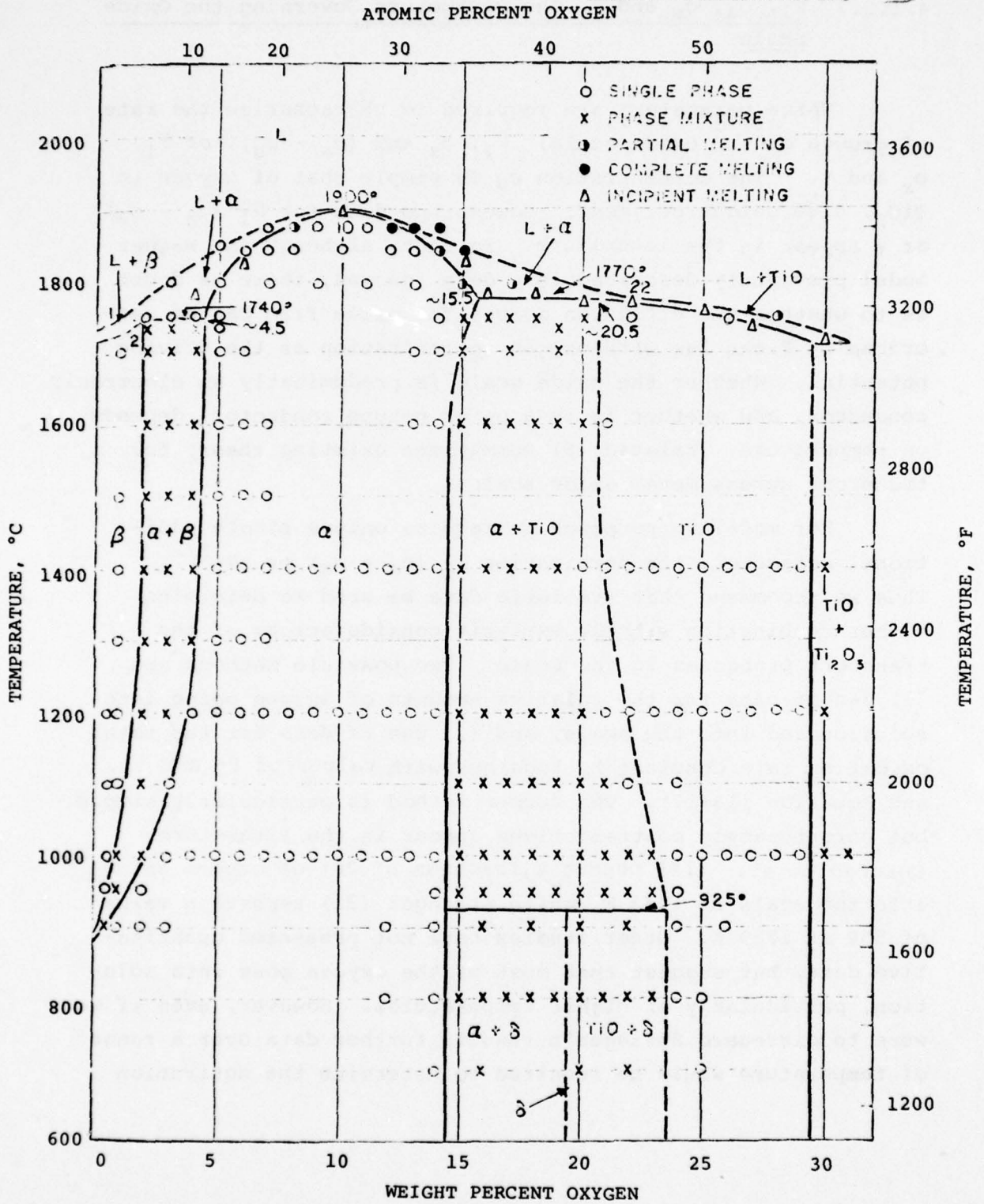
FIGURE 4-2.   PHASE DIAGRAM FOR THE TI-O SYSTEM

4.1.2.3 $\mathcal{D}_1$, c_a, c_s and γ, The Parameters Governing the Oxide Scale

Three parameters are required to characterize the rate of growth of the oxide scale: $\mathcal{D}_1$, c_s and $(c_a - c_s)$, or $\mathcal{D}_1$, c_s and γ. The concentration c_s is simply that of oxygen in TiO_2, 0.40 weight per cent. However no data for $\mathcal{D}_1 (c_a - c_s)$ or γ appear in the literature. In fact, although the Wagner model previously described is widely ignored, there is doubt as to whether the diffusion across the oxide film can be described by Ficks law with oxygen concentration as the driving potential. Whether the oxide scale is predominatly an electronic conductor, and whether it is a p- or n-type conductor, depends on temperature. Kofstad (9) summarizes existing theory for transport across metal oxide scales.

For modeling purposes we require only a single additional parameter, the combination $\mathcal{D}_1 (c_a - c_s)$ or $\gamma \mathcal{D}_1^{1/2}$. Thus we recommend that available data be used to determine either combination without explicit considerations of the transport processes in the scale. Two possible methods are (1) use of data for the relative amounts of oxygen going into solution and into the scale, and (2) use of data for the total oxidation rate constant K_0 together with values of $\mathcal{D}_2$ and c_u, and Equation (13-17). The former method is particularly simple but unfortunately contradictions appear in the literature. Kofstad et al. (14) report a fraction of 20% of oxygen going into the scale at 1173 K, while Stringer (21) reports a value of 55% at 1223 K. Other studies have not presented quantitative data, but suggest that most of the oxygen goes into solution, particularly at higher temperatures. However, even if we were to disregard Stringer's result, further data over a range of temperature would be required to determine the activation

energy of D_1. Application of the latter method requires selection of the most reliable and appropriate data for K_O and D_2 since, again, contradictions do appear in the literature. For example, if we were to use the Kofstad data for K_O and Rosa's data for D_2, we would deduce that considerably more than 20% of the oxygen was going to form scale, in variance with the value reported by Kofstad.

4.1.2.4 Data for K_O, The Total Oxidation Rate Constant

For unalloyed titanium Stringer [21] compared the data of his own and several previous studies. Figure 4-3 taken from [21] shows his result. His correlation for K_P^2 $(=4K_O^2)$ is

$$4K_O^2 = 1.007 \times 10^{-6} \exp\left(-\frac{25,400}{RT}\right) + 320 \exp\left(-\frac{61,800}{RT}\right) \text{ gm}^2/\text{cm}^4\text{s} \qquad (23)$$

and concluded that D_1 has an activation energy of 25,400 cal/mole while D_2 has an activation energy of 61,800 cal/mole. It is of interest to note that K_f/K_O calculated from Equation (23) at 1223 K is close to unity and not 55% as quoted by Kofstad [9] as being obtained by Stringer.

Kofstad [9] compared the data obtained by Kofstad et al. [14] with previous studies, as shown in Figure 4-4: good agreement is apparent. The more recent data is that of Wolf [10]. Figure 4-5 shows Wolf's data for "Type 1" unalloyed titanium with Stringer's correlation, Equation (22) and the data of Kofstad et al. [14]. Within experimental error there is excellent agreement between Wolf's data points and the Stringer correlation. Comparison of Figures 4-3, 4-4 and 4-5 leads to the conclusion that the experimental data for K_O is reasonably consistent and well represented by Equation (23).
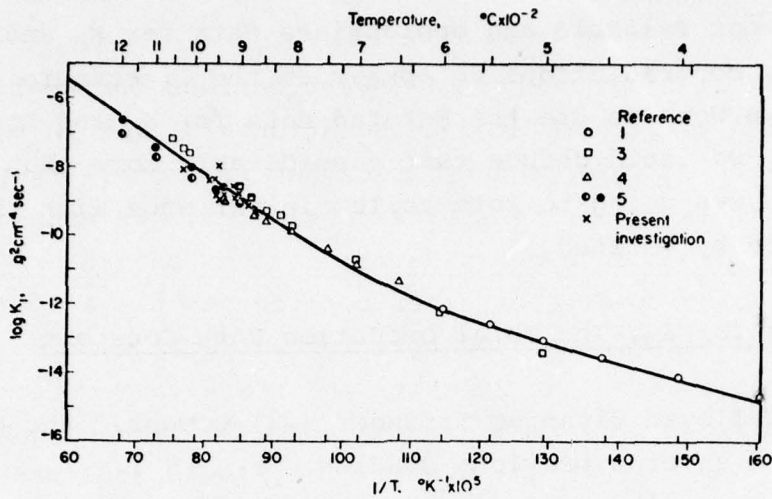
TABLE 4-3. SUMMARY OF SPECIMENS (TI6AL-4V) USED TO COMPARE PREDICTED
REACTION RATE WITH EXPERIMENT (10)
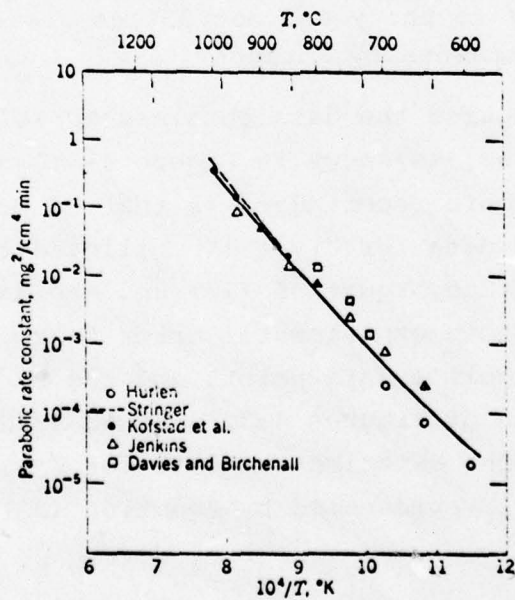
FIGURE 4-4. TOTAL OXIDATION RATE CONSTANT [KOFSTAD]

Pressure Dependence

Since a large number of investigations for unalloyed titanium are well correlated by Equation (23), it is possible to discern if K_O is dependent on oxygen pressure. Table 4-1 below lists the oxygen pressures considered. We conclude that there is <u>no dependence of oxidation rate on oxygen pressure</u> in the range of conditions under consideration. Wolf (10) obtained one data point at 400 torr for which K_p was about twice the value be obtained at 200 torr and the same temperature. He thus claims that "the degree of reaction is very nearly linearly related to oxygen pressure. This speaks strongly against any type of solid-state reaction control..". It seems quite unwarranted for Wolf to make such a claim based on one data point, when there is so much evidence in the literature to the contrary: we are of the opinion that Wolf's result should be disregarded at this time.

Table 4-1. Oxygen Pressures in Investigations
of Unalloyed Titanium

INVESTIGATION	PRESSURES
Wolf (10)	200 torr
Stringer (21)	1 atm
Kofstad et al. (14)	1 atm
Jenkins (22)	40-700 mm
Davies and Birchenall (23)	1 atm
Hurlen (24)	1-760 mm

Ti-6Al-4V Alloy

The only data available for this alloy is that of Wolf (10), which is also shown in Figure 4-5. The oxidation rate is higher than that for unalloyed titanium which is in line with the conclusion of Shambler and Redden (15) that $\mathcal{D}_2$ increases somewhat with substitutional alloying content. Given the scatter in the experimental data there is no basis for concluding that the activation energy differs from that of unalloyed titanium. For temperatures above 1000 C Equation (23) can be approximated

$$4K_O^2 \cong 320 \exp\left(-\frac{61,800}{RT}\right) \text{ gm}^2/\text{cm}^2\text{s} \quad \text{(unalloyed)} \tag{24}$$

For Ti-6Al-4V the values of K_O^2 measured were on an average 60% higher than Equation (23), thus we recommend

$$4K_O^2 = 480 \exp\left(-\frac{61,800}{RT}\right) \text{ gm}^2/\text{cm}^2\text{s} \quad \text{(Ti-6Al-4V)} \tag{25}$$

4.1.3 Oxidation of Titanium by Steam

At the temperatures and pressures of interest steam will be only slightly dissociated. Table 4-2 below tabulates equilibrium compositions at 0.3 atm pressure.

Table 4-2. Equilibrium Compositions of Steam at
0.3 atm (25).

COMPOSITION (MOLE FRACTIONS)	TEMPERATURE° K			
	1200	1400	1500	1700
H_2	0	.0001	.0003	.0007
H_2O	1.0000	.9998	.9995	.0089
O_2	0	0	.0001	.0003
OH	0	0	.0001	.0002
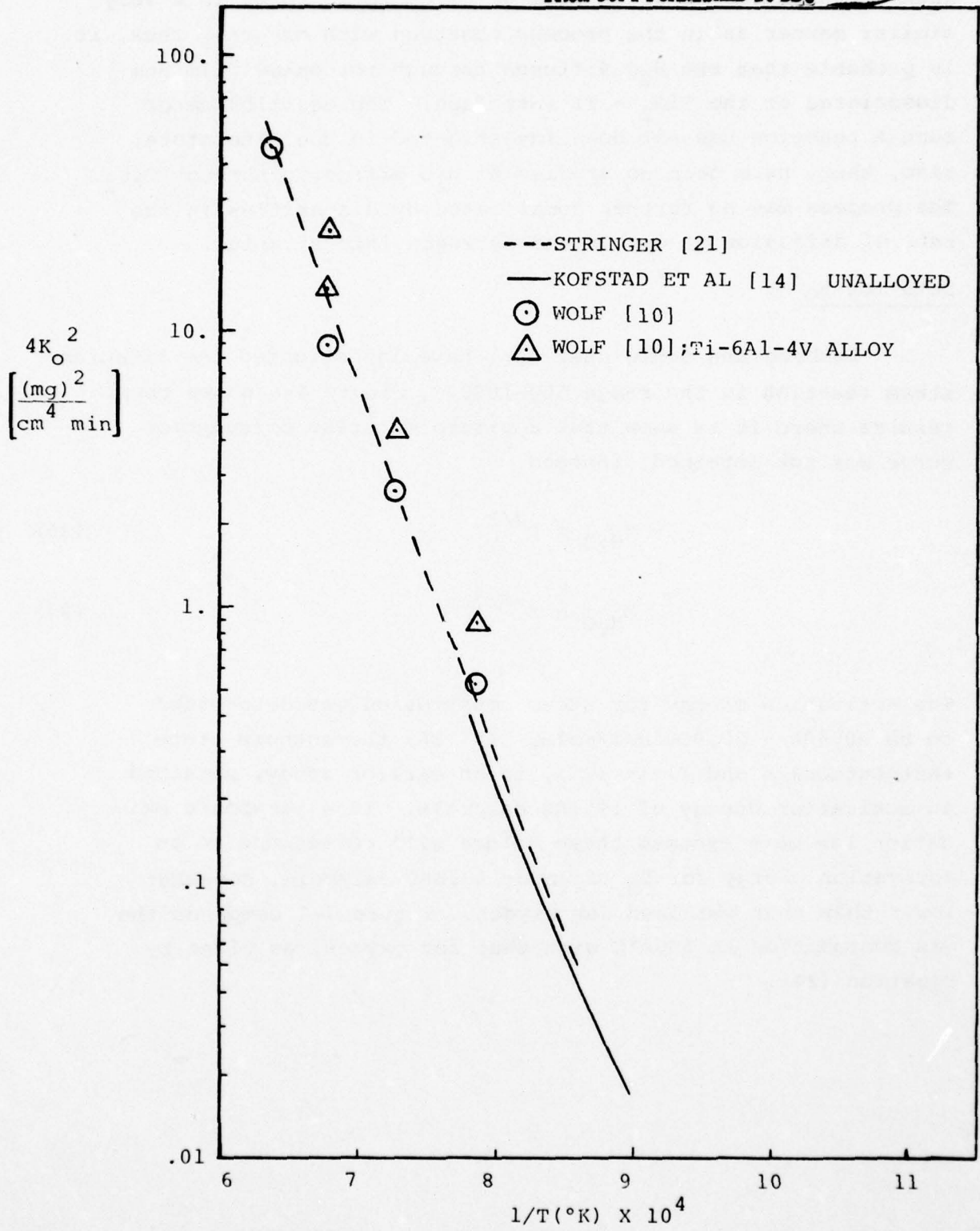
FIGURE 4-5.   OXIDATION RATE CONSTANT FOR TI-6AL-4V

When titanium reacts with steam an oxide layer forms in a very similar manner as in the process observed with oxygen; thus, it is probable that the H_2O diffuses through the oxide film and dissociates at the TiO_2 - Ti interface. The equilibrium of such a reaction has not been investigated in the literature; also, there have been no studies of H_2O diffusion through TiO_2. The process may be further complicated by disparities in the rate of diffusion of oxygen and hydrogen into titanium.

Data for K_O

Löhberg and Schleicher (26) have investigated the titanium-steam reaction in the range 600-1000 C. Figure 4-6 shows their results where it is seen that a parabolic steam consumption curve was not obtained, instead

$$M_{H_2O} \propto t^{2/3} \tag{26}$$

$$\dot{M}_{H_2O} \propto t^{-1/3} \tag{27}$$

The activation energy for steam consumption was determined to be 20,400 - 20,900 cal/mole. In (26) the authors state that Lutschkin and Iljin (27), in an earlier study, obtained an activation energy of 19,100 cal/mole. If a parabolic oxidation law were assumed these values will correspond to an activation energy for $\mathcal{D}_2$ of about 40,000 cal/mole, somewhat lower than that obtained for oxygen. Figure 4-7 compares the gas consumption at $1000^\circ C$ with that for oxygen, as given by Equation (24).
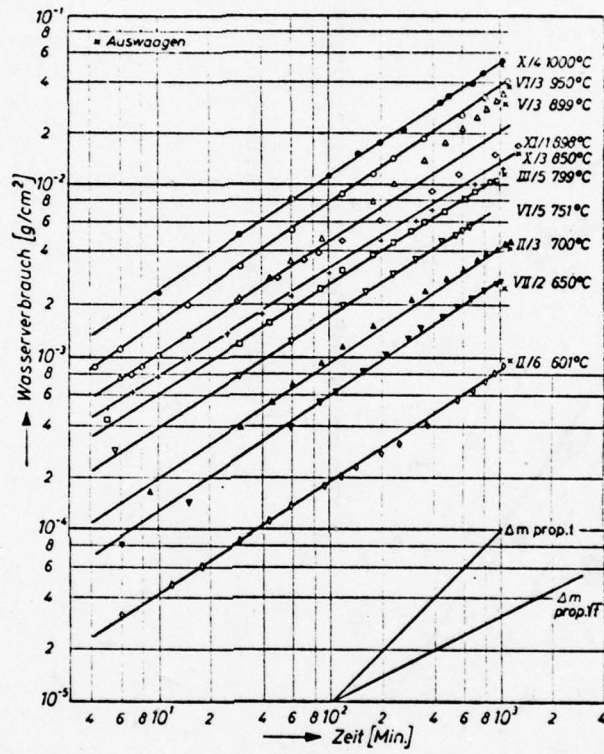
FIGURE 4-6. TITANIUM STEAM REACTION
LÖHBERG AND SCHLEICHER
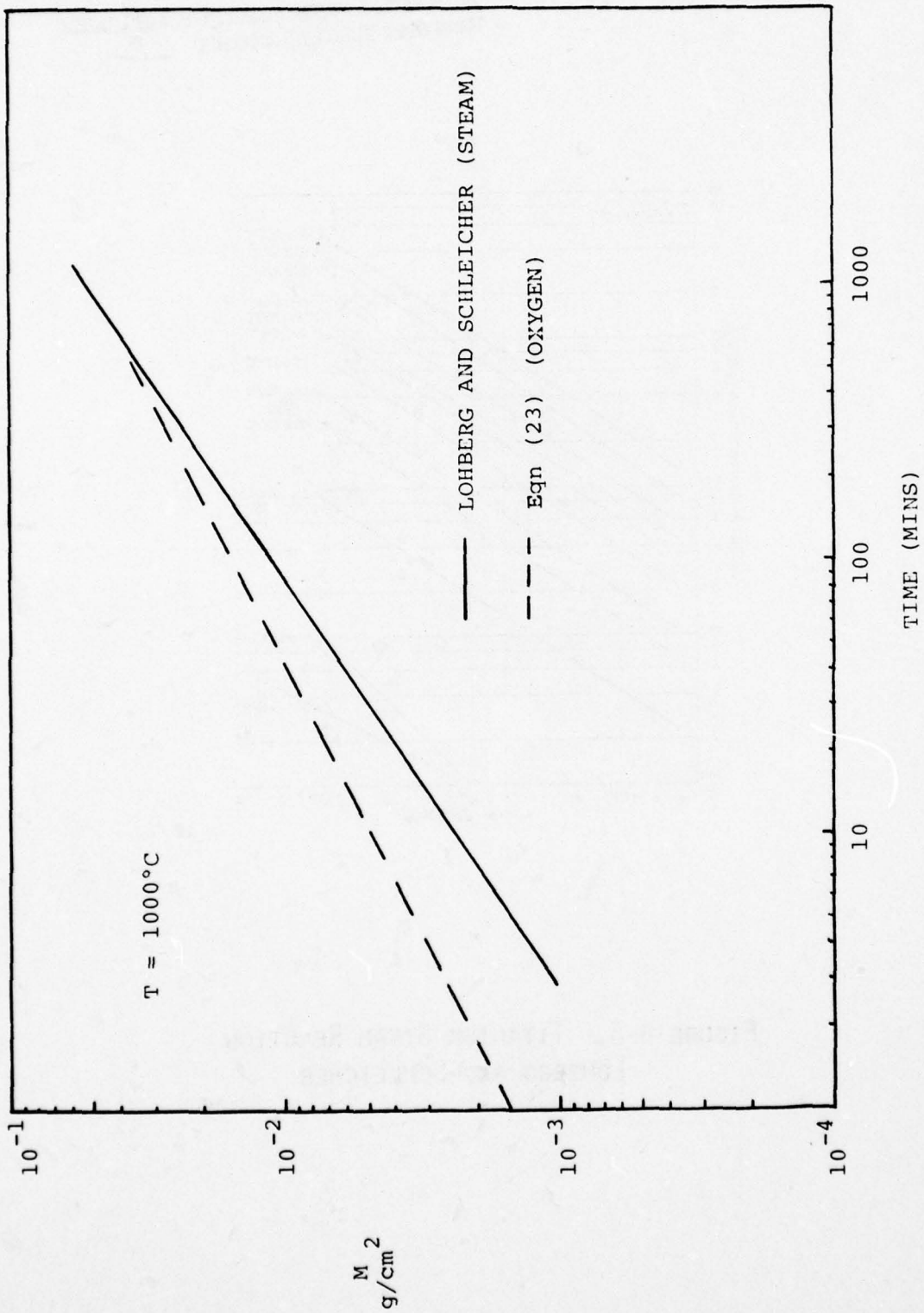
FIGURE 4-7. COMPARISON OF OXYGEN AND STEAM GAS CONSUMPTION

Lainer, Bai and Typsin (28) also studied the titanium-steam reactions but the data reported is sparse. Oxidation rates were correlated with the diffusion coefficient $\mathcal{D}_1$ for oxygen transport in a rutile scale. Values for $\mathcal{D}_1$ formed by oxidation in H_2O are claimed to be 40-600 times the values obtained for oxidation in air. No rate constants for the titanium-steam reaction are reported.

4.1.4 Heats of Oxidation and Solution of Oxygen in Titanium

The energy evolved per gm atom of reacting oxygen in titanium for different end products has been calculated by Mah et.al. (Bureau of Mines Report of Investigation 5316) and is shown in Figure 4-8. For modeling purposes, it is adequate to use as heats of oxidation and solution, 12024 Btu/lb O_2 and 15,575 Btu/lb O_2 respectively.
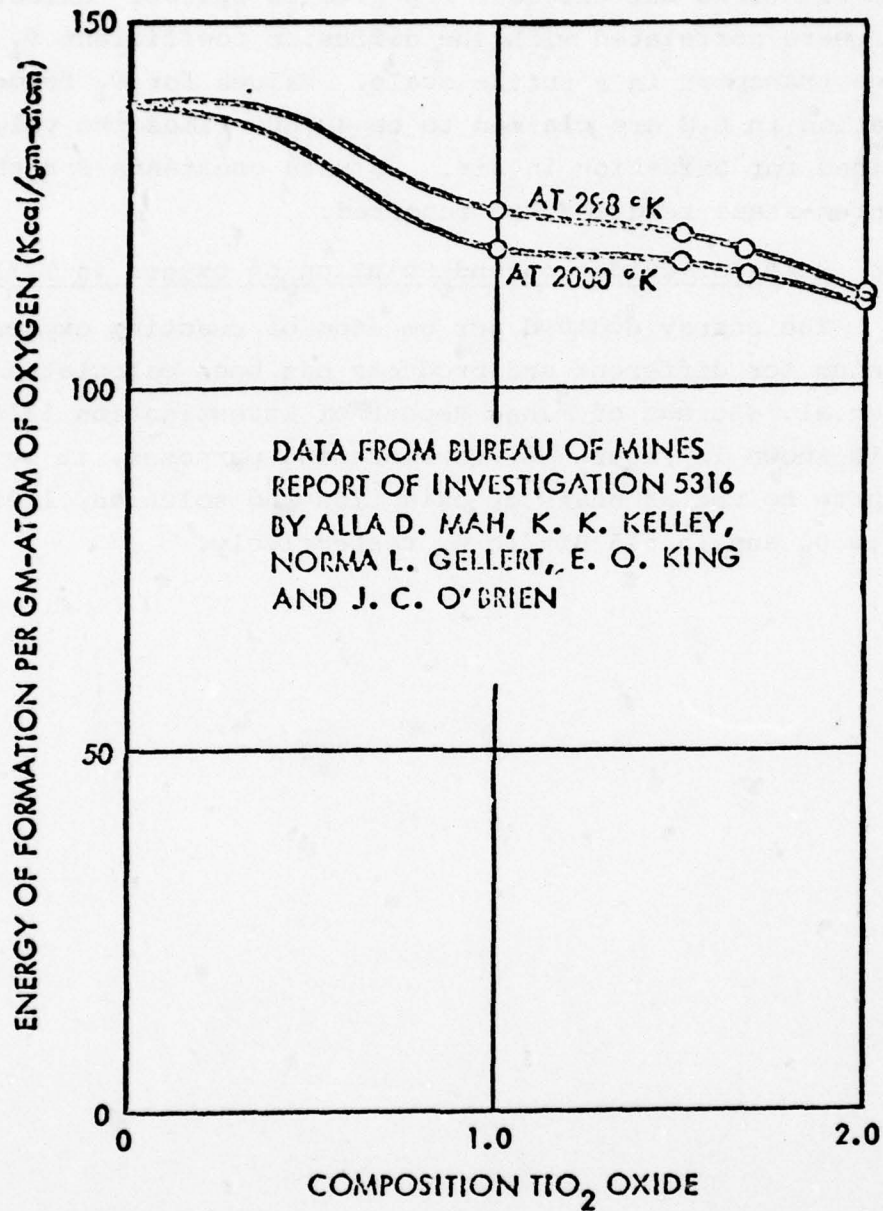
FIGURE 4-8. ENERGY PRODUCED PER GM-ATOM OF REACTING OXYGEN
(16 GM O) IN TI FOR DIFFERENT END PRODUCTS
AND REACTION TEMPERATURE

4.1.5 Hydrogen Dissolution in Titanium Review

4.1.5.1 Literature Survey

The dissolution of hydrogen in titanium differs from oxygen dissolution in that it is a reversible reaction, and provided the temperature is high enough to permit finite rate processes, titanium-hydrogen alloys can only exist in equilibrium with a gaseous hydrogen atmosphere. Figure 4-9 shows the equilibrium concentrations for pure titanium. Figure 4-10 shows the phase diagram and Figure 4-11 is deduced from 4-10.
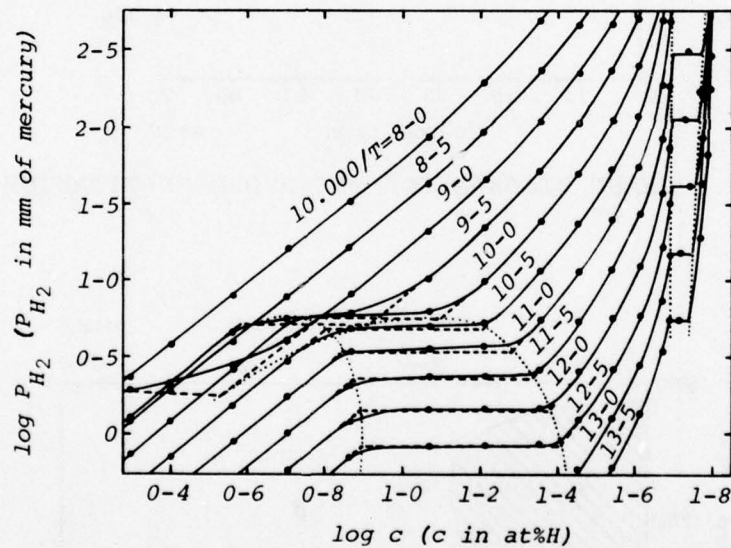
FIGURE 4-9.   EQUILIBRIUM CONCENTRATIONS FOR PURE TITANIUM

Waisman, Sines and Robinson (29) investigated equilibrium for Ti-6Al-4V alloy and found that, at a given solid phase hydrogen concentration and temperature, the equilibrum gas pressure was 2.31 times that for pure titanium.
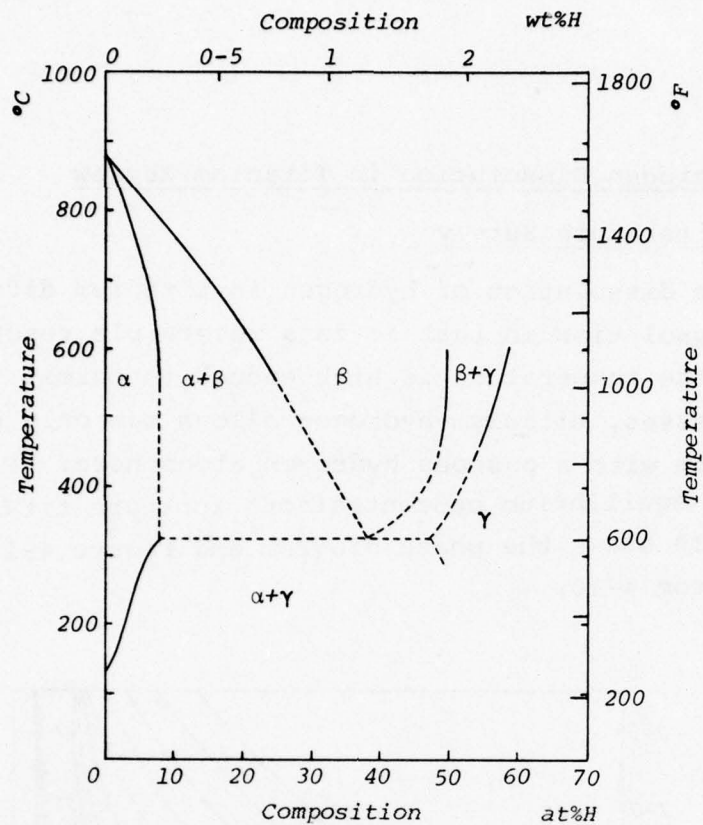
FIGURE 4-10.   PHASE DIAGRAM FOR THE HYDROGEN-TITANIUM SYSTEM
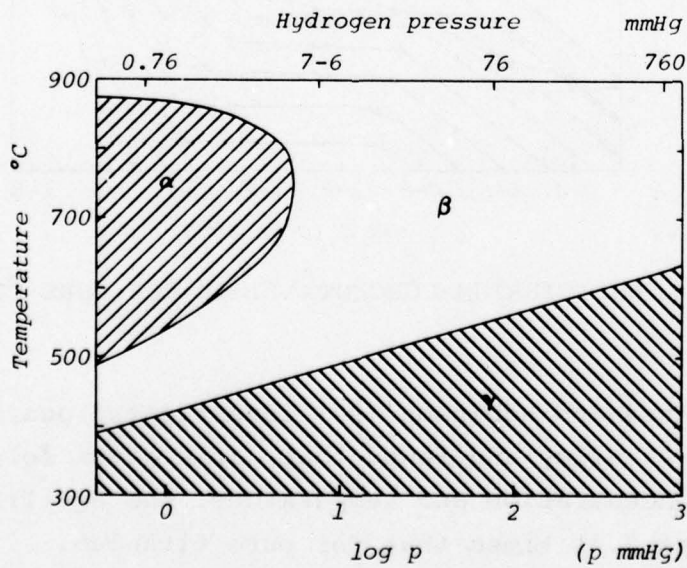
FIGURE 4-11.   TITANIUM PHASES AS THEY DEPEND ON TEMPERATURE AND
HYDROGEN PRESSURE

4-24

Diffusion coefficients of hydrogen in pure titanium
have been measured by Wasilewski and Kehl (30) as

$$\mathcal{D}_\beta = 1.95 \times 10^{-3} \exp \; \{(-6640 \pm 500)/RT\} \;\; cm^2/s$$

$$\mathcal{D}_\alpha = 1.8 \;\; \times 10^{-2} \exp \; \{(-12380 \pm 680)/RT\} \; cm^2/s$$

which are considerably larger than the diffusion coeffi-
cients for oxygen in titanium.

The heat of solution of hydrogen in titanium has been
calculated by McQuillan, and is reported by Skinner et.al.
(31) as -21,600 cal/mole to form α solution and -27,800
cal/mole to form β solution. These values are valid for
dilute solutions (less than 10 atom % H).

4.1.5.2 Sample Numerical Calculations

Since the mechanism and equilibrium of the titanium-
steam reaction is unknown, it is only possible to obtain rough
estimates of hydrogen dissolution in titanium exposed to steam.
Since the diffusion coefficient for hydrogen in titanium is
considerably larger than that for oxygen, a possible approach
is to simply assume that the hydrogen goes into solution in
the stoichiometric proportion indicated by the H_2O formula,
i.e., 1 lb H for 8 lbs O_2. At 1200K the oxygen reaction rate
is

$$\dot{M}_{O_2} = K_o t^{-1/2} \qquad K_o = (4K_p)^{1/2}$$

$$= 22.4 \exp \left(\frac{-30,900}{(1.987)(1200)}\right)$$

$$= 5.27 \times 10^{-5} \; lb/ft^2 s^{1/2}$$

$$\dot{M}_{O_2} = 5.27 \times 10^{-5} t^{-1/2} \; lb/ft^2 s^{1/2}$$

Heat evolved $= \dot{M}_{O_2} \, \Delta H$

$$= (5.27 \times 10^{-5}) \, \left(\frac{280,000}{32}\right) (1.8) \, t^{-1/2}$$

$$= 0.83 \; t^{-1/2} \; \text{Btu/ft}^2 s^{1/2}$$

Then

$$\dot{M}_{H_2} = 0.125 \; \dot{M}_{O_2}$$

$$= 0.659 \times 10^{-5} t^{-\frac{1}{2}} \; \text{lb/ft}^2 s^{\frac{1}{2}}$$

Heat evolved $= \dot{M}_{H_2} \, \Delta H$

$$= (0.659 \times 10^{-5}) \left(\frac{27,800}{2}\right) (1.8) \, t^{-\frac{1}{2}}$$

$$= 0.165 \; t^{-\frac{1}{2}} \text{Btu} /\text{ft}^2 s^{\frac{1}{2}}$$

which is about 20% of the heat evolved by the O_2 reaction.

However, McQuillan (32) states that the rate of hydrogen absorption is considerably reduced when the surface has been "contaminated" by oxygen. No quantitative information on the effect has been published, but Gulbransen and Andrew (33) have examined the corresponding effect in Zirconium in some detail. A further and, perhaps, more important consideration is that the bulk of the water vapor available for reaction with a titanium shroud results from evaporation of water droplets or ice particles. Let us now calculate the latent heat associated with a droplet evaporation process to produce the hydrogen dissolution rate calculated above. The amount of water evaporated to sustain the hydrogen dissolution rate calculated above is

$$\dot{M}_{H_2} = (81/2)\dot{M}_{H_2} = (18/2) \ (.659 \times 10^{-5})t^{-\frac{1}{2}}$$

$$= 5.93 \times 10^{-5}t^{-\frac{1}{2}} \ \text{lb/ft}^2\text{s}^{\frac{1}{2}}$$

and since the latent heat is approximately 1000 Btu/lb the rate at which heat is absorbed is

$$Q_{vap} = (5.93 \times 10^{-5})(1000)t^{-\frac{1}{2}} = .059t^{-\frac{1}{2}} \ \text{Btu/ft}^2$$

which is 36% of the heat evolved by the hydrogen dissolution. Thus, at most the net increase in heat liberation is (1 - 0.36) (20) = 12.8% more than the value obtained for oxidation in air or oxygen.

4.1.5.3 Effect of Temperature Level

At higher temperatures the degree of dissociation of H_2O will be greater (see Table 4-2), and the diffusion co-efficient of H in titanium is also higher; however, the solubility of H decreases rapidly with temperature (see Figure 4-9) and the net effect is, for example, at 1500K the rate of dissolution of H is about 40% less than at 1200K.

4.1.6 Evaluation of Clemson Data (3) for Oxygen Consumption Rate: Ti-6Al-4V Alloy

4.1.6.1 Model Parameters Based on Weight Change Measurements

Based on the long time weight change measurements made at Clemson (10) we proposed Eq. (24) to give the rate constant K_p for oxidation of Ti-6Al-4V alloy, viz.

$$K_p^2 = 480 \exp\left(\frac{-61,800}{RT}\right) \ gm^2/cm^2 s \tag{24}$$

Our model parameters $\mathcal{D}_1$, $\mathcal{D}_2$, γ and K_o be calculated from K_p as follows. Ignoring moving boundary effects and postulating 80% of the oxygen goes into solution while 20% goes to form oxide, we can derive

$$4K_o^2 = K_p^2 \tag{25}$$

$$\frac{\rho_{TiO_2}}{3.33} \ \mathcal{D}_1^{1/2} \ \gamma^2 + C_u \left(\frac{\mathcal{D}_2}{\pi}\right)^{1/2} \gamma - \frac{\mathcal{D}_1^{1/2}}{2} (C_a - C_s) = 0 \tag{26}$$

$$2C_u \left(\frac{\mathcal{D}_2}{\pi}\right)^{1/2} t^{1/2} = (0.8) \ (4K_o^2)^{1/2} \ t^{1/2} \tag{27}$$

$$2C_u \left(\frac{\mathcal{D}_2}{\pi}\right)^{1/2} t^{1/2} = 4 \left(\frac{C_a + C_s}{2}\right) 2 \ \gamma (\mathcal{D}_1 t)^{1/2} \tag{28}$$

with $\quad C_u = 40.2 \ lb/ft^3$

$$C_s = 106.3 \ lb/ft^3$$

$$C_a = 107.2 \ lb/ft^3$$

$$\rho_{TiO_2} = 281 \ lb/ft^3$$

and assuming the same actiation energy for $\mathcal{D}_1$ and $\mathcal{D}_2$, the equations may be solved to give

$$\gamma = .0297$$

$$\mathcal{D}_{10} = 2.03 \ ft^2/s$$

$$\mathcal{D}_{20} = 0.676 \ ft^2/s$$

4.1.6.2 Comparison with Volumetric O_2 Consumption Measurements

Table 4-3 summarizes the pertinent details of the tests for which satisfactory measurements of oxygen consumption rate were made. Turning first to the low heating rate tests (0.5°C/s), Figure 4-12 shows a comparison of the predictions of our computer code with the experimental data for $\dot{M}_{O_2}$ as a function of time. Since the prediction lies between the experimental results for the two types of Ti-6Al-4V alloy, we view the prediction as quite satisfactory. For these low heating rates, Wolf et.al. (34) also concluded that the parabolic kinetics implicit in the model are satisfactory.

Figure 4-13 shows a comparison at a heating rate of 8°C/s where the comparison is, at first sight, less satisfactory. However, a number of considerations are pertinent. (i) In the Clemson experiments, there were apparent difficulties in recording the zero time point accurately. Table 3 compares the time that should have elapsed to reach 1100°C (calculated) with the actual time; the discrepancies are 40, 45 and 30 seconds for the three specimens. Thus, in Figure 13 the experimental curves have been adjusted by the above time displacements, a rather unsatisfactory procedure. (ii) Since the three specimens are of the same type of Ti-6Al-4V alloy, the differences between the experimental curves indicate the lack of precision in the experiments and possible variability of physical phenomena (e.g., cracking of the oxide scale). (iii) The data points indicated on the

TABLE 4-3. SUMMARY OF SPECIMENS (Ti6Al-4V) USED TO COMPARE PREDICTED
REACTION RATE WITH EXPERIMENT (10)

Specimen No.	Type	Final Temp. °C	Heating Rate °C/s	Calculated Time to 1100°C (sec)	Actual Time to 1100°C (sec)	Actual Time to M_{max} (sec)
401161	1	1100	0.5	2150	2280	2190
402042	2	1100	0.5	2150	2220	2070
405071	1	1100	8	134.4	174.0	174.0
405072	1	1100	8	134.4	180.0	192.0
11202	1	1100	8	134.4	165.0	135.0
402043	2	1100	22	48.9	67.8	60.0
401092	1	1100	22	48.9	81.0	45.0
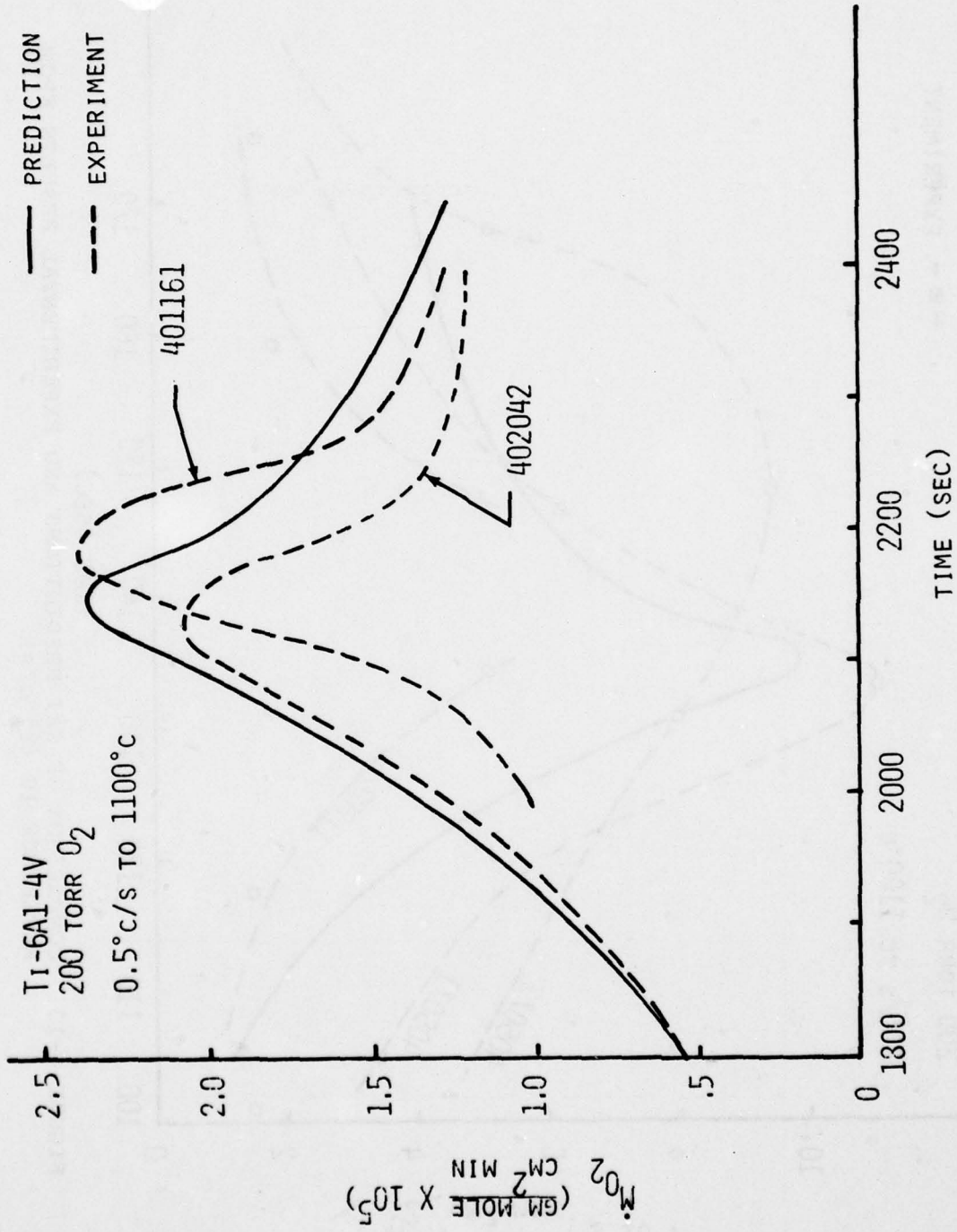
FIGURE 4-12. COMPARISON OF SAI PREDICTIONS AND EXPERIMENTAL RESULTS FROM REFERENCE 10 (0.5°c/s)
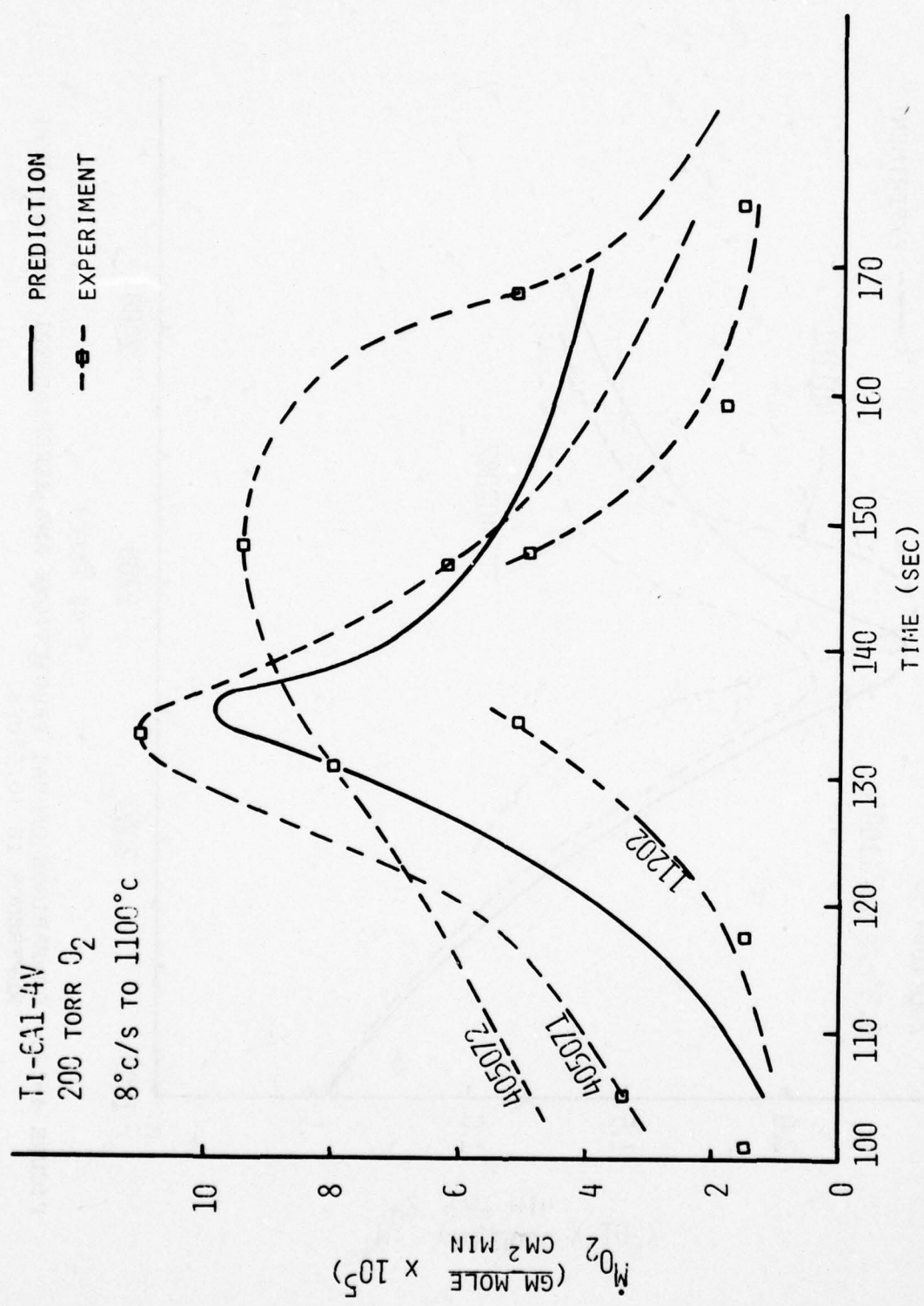
FIGURE 4-13. COMPARISON OF SAI PREDICTIONS AND EXPERIMENTAL RESULTS FROM REFERENCE 10 (8° c/s)

experimental curves are those actually recorded. It is clear that they are too sparse to record a peak in $\dot{M}_{O_2}$ as sharp as indicated by theory. Furthermore, in the experiments there were problems in preventing temperature over-shoots at the end of the heating period. Such overshoots would tend to broaden the observed peaks in $\dot{M}_{O_2}$. Figure 4-14 shows a comparison at a heating rate of 22°C/s; again, the sharpness of the predicted peak in $\dot{M}_{O_2}$ is in evidence.

In our review, the predictions at higher heating rates are adequate in view of the experimental uncertainties. Thus, we do not support the view of Wolf et.al. (34) that at high heating rates the parabolic kinetics should be dis-carded in favor of the asymptotic rate law of Evans (35). Furthermore, we are also doubtful if further corrections should be made as suggested in (10), for example, the sug-gested increase in effective reaction surface area during rapid heating. It is important to note that the intro-duction of an ad hoc kinetics expression such as the asymp-totic rate law would preclude rational modeling of the oxidation process: it would then not be possible to account for such features as spatial temperature variations, and mechanical removal of the oxide film.
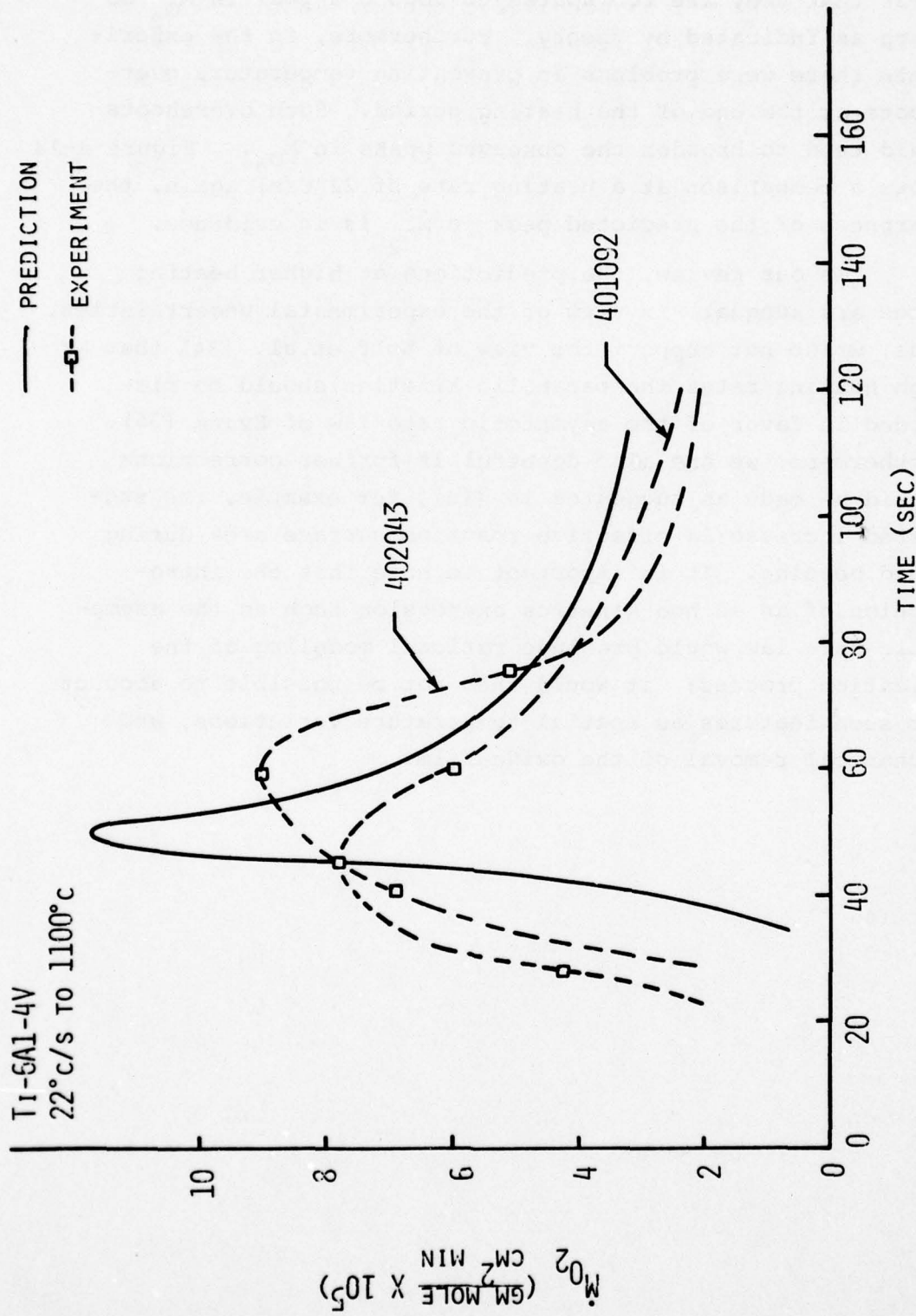
FIGURE 4-14. COMPARISON OF SAI PREDICTIONS AND EXPERIMENTAL RESULTS FROM REFERENCE 10 (22° c/s)

4.2   Analysis of Oxidation Test Data

The analytical model developed in Section 4.1 for oxidation of 6AL-4V titanium in oxygen environments was used to analyze the results of the Phase I SAI oxidation test data. Analytical predictions for the weight gain as a function of time for the indicated experimentally measured temperature history are shown in Figure 4-15 for typical runs. The final experimental weight gain is shown for comparison.

Important conclusions from this analysis include:

1) weight gain during the transient heat-up period is not important

2) the tests were essentially isothermal temperature oxidation governed by the parabolic law as developed in Section 4.1.

The total experimental data base is shown in Figure 4-16 in terms of weight gain (ΔW) normalized by square root of time (reflecting the parabolic law) in comparison with the analytical model and uncertainty bands based on information in the literature. The Phase I SAI data falls within the uncertainty bounds of the model and generally supports the parabolic oxidation rate law. Within the context of this evaluation, an increased oxidation in H_2O vapor is shown up to 1700°K. A pressure effect is also apparent, especially at 1400°K, although the 1400°K data appear anomalous compared to the other data points.

Application of the oxidation model to the AEDC DET data shows good agreement with measured heat transfer. Figure 4-17 illustrates the Run 7 ti-22 model clear air response stagnation point heat transfer data in comparison with predictions. The dominant convective heating trend
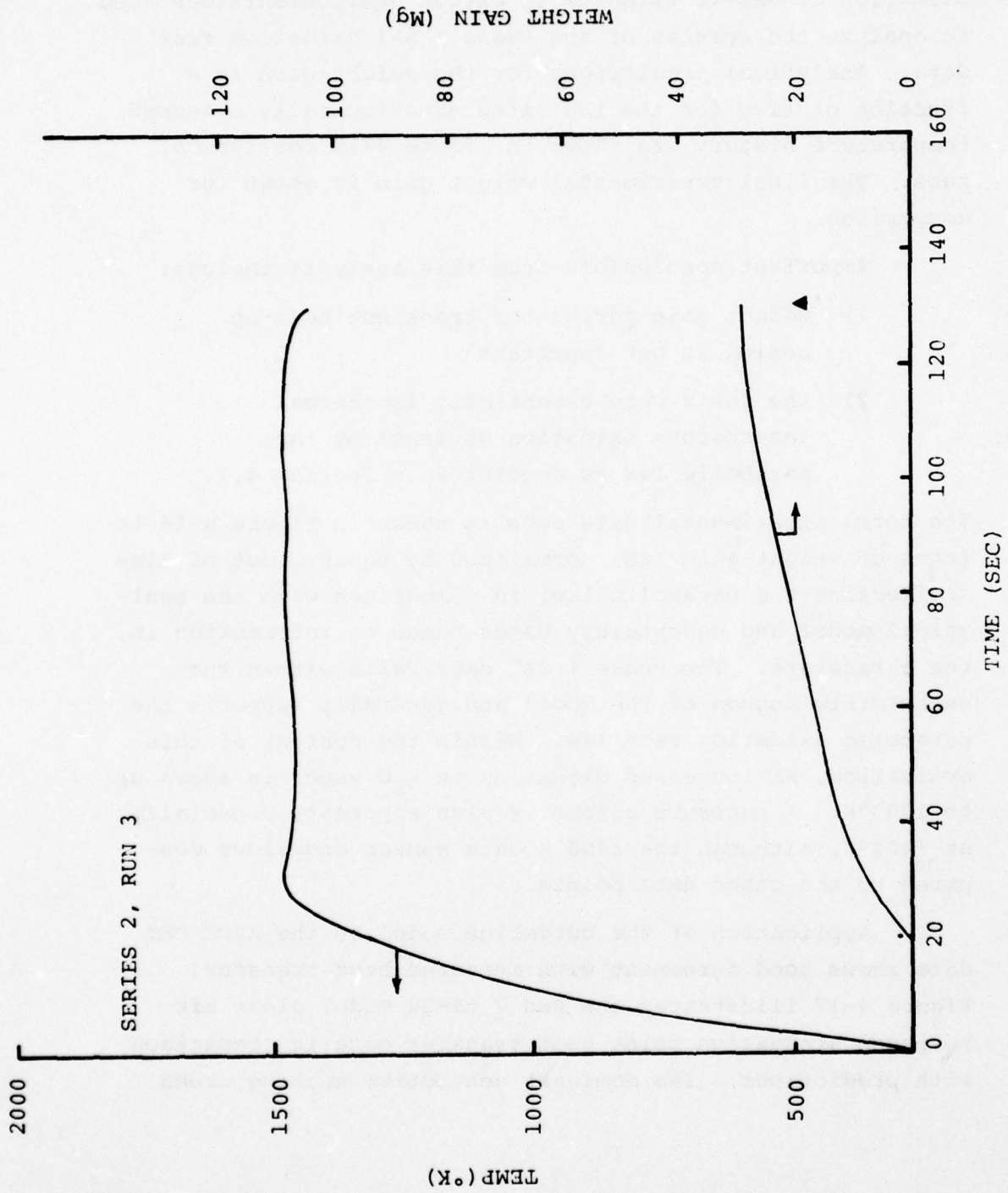
FIGURE 4-15A. ANALYSIS OF SAI OXIDATION DATA RUNS

SERIES 2, RUN 4
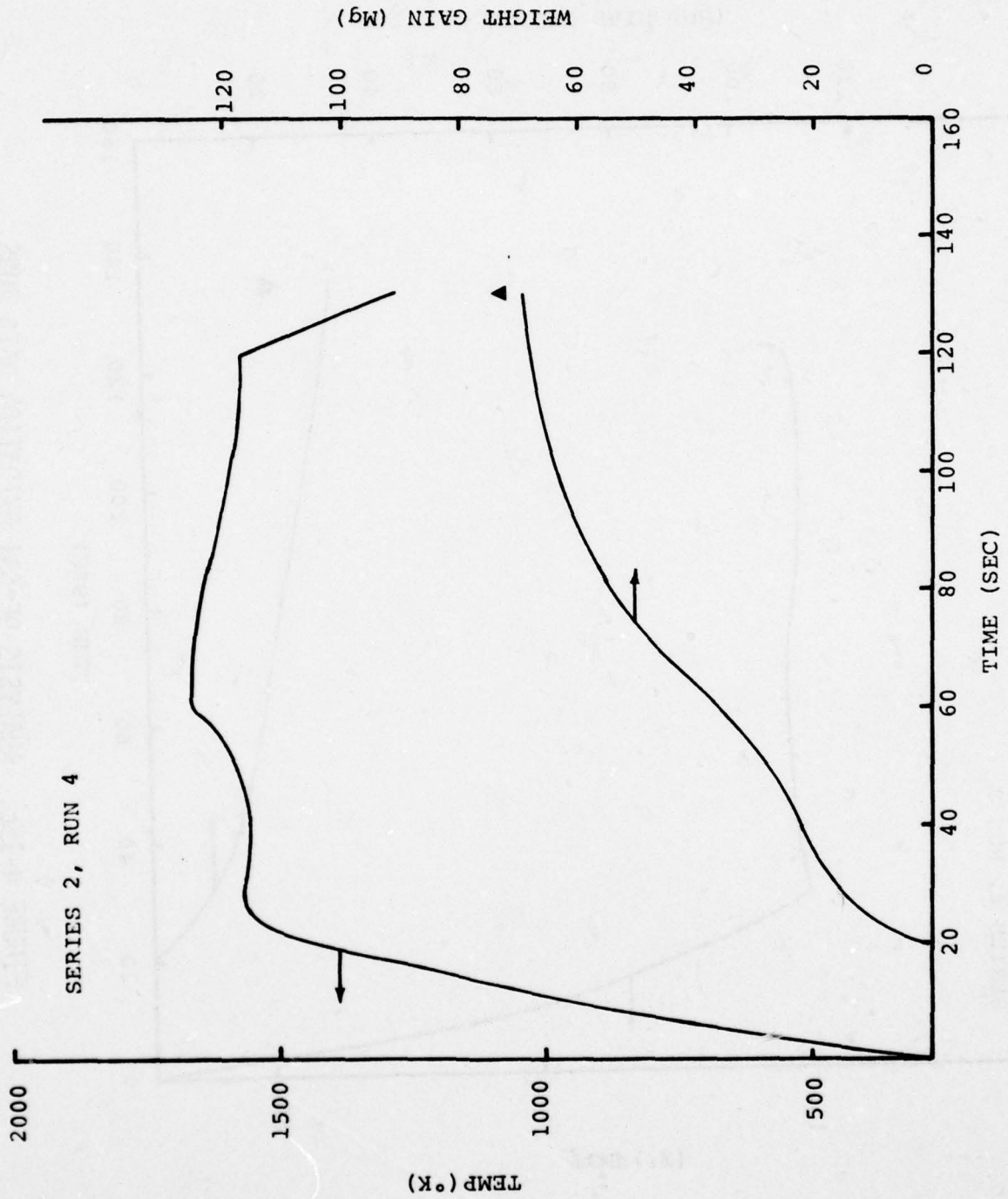
FIGURE 4-15B. ANALYSIS OF SAI OXIDATION DATA RUNS
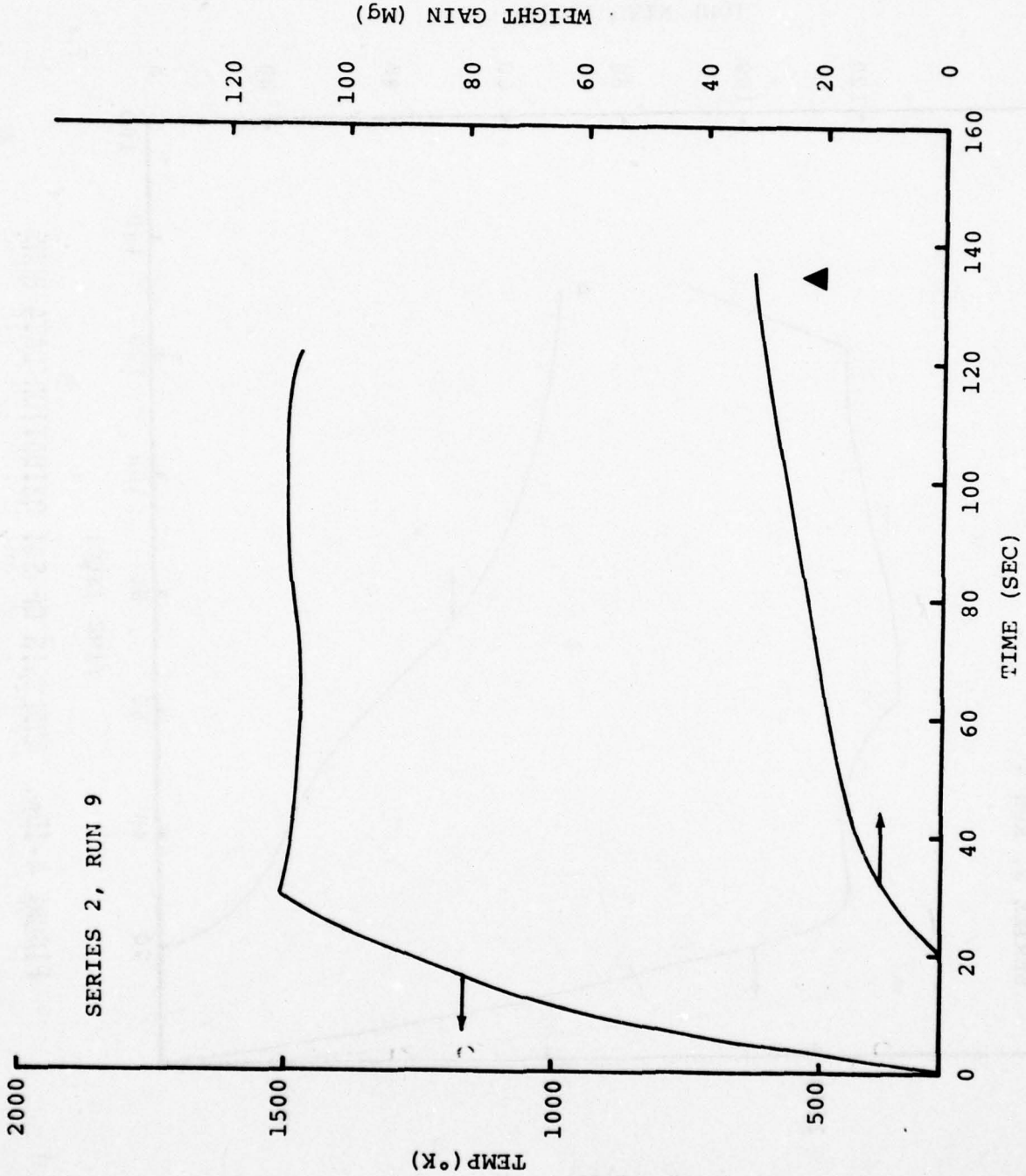
FIGURE 4-15c. ANALYSIS OF SAI OXIDATION DATA RUNS
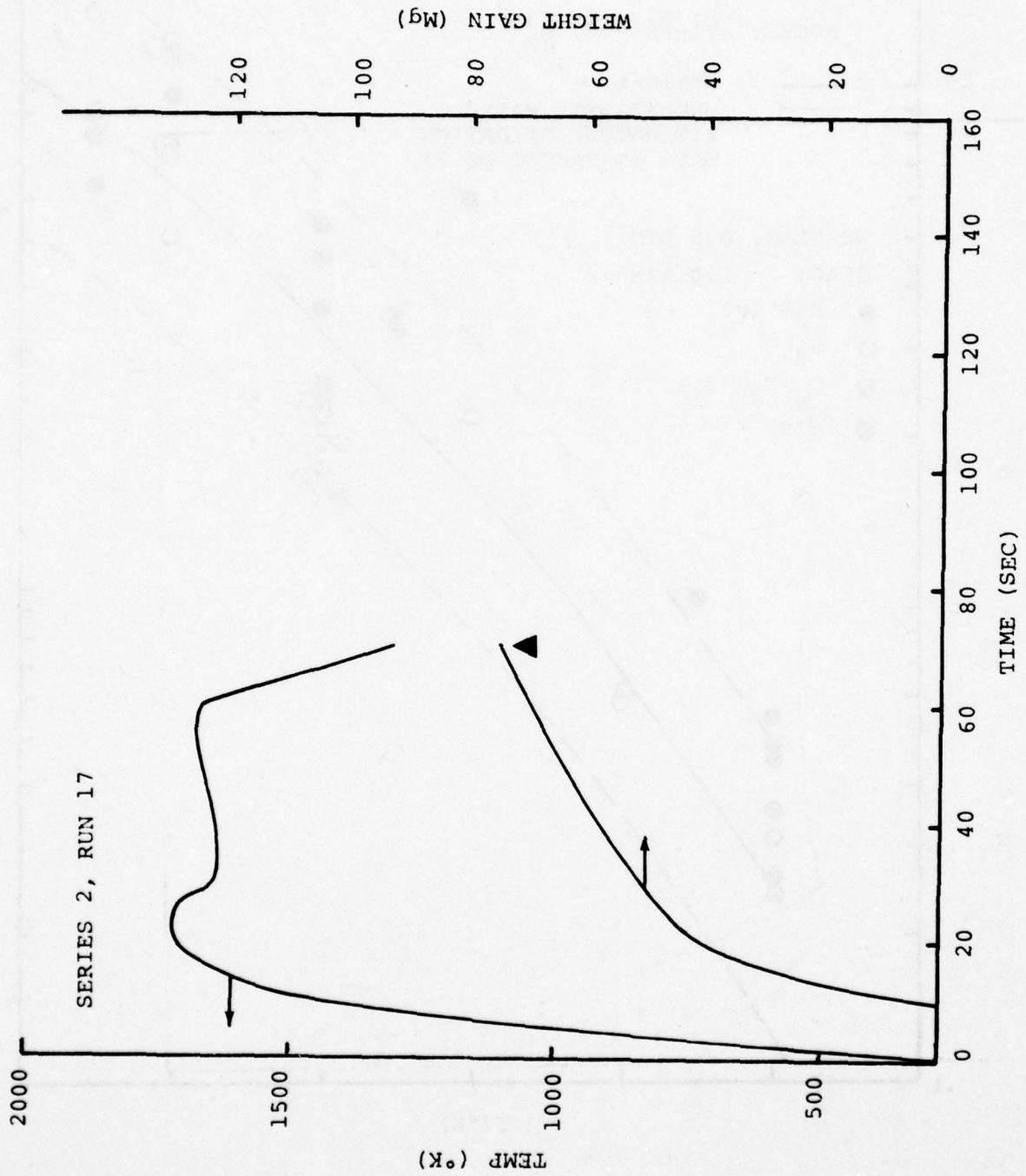
FIGURE 4-15D. ANALYSIS OF SAI OXIDATION DATA RUNS
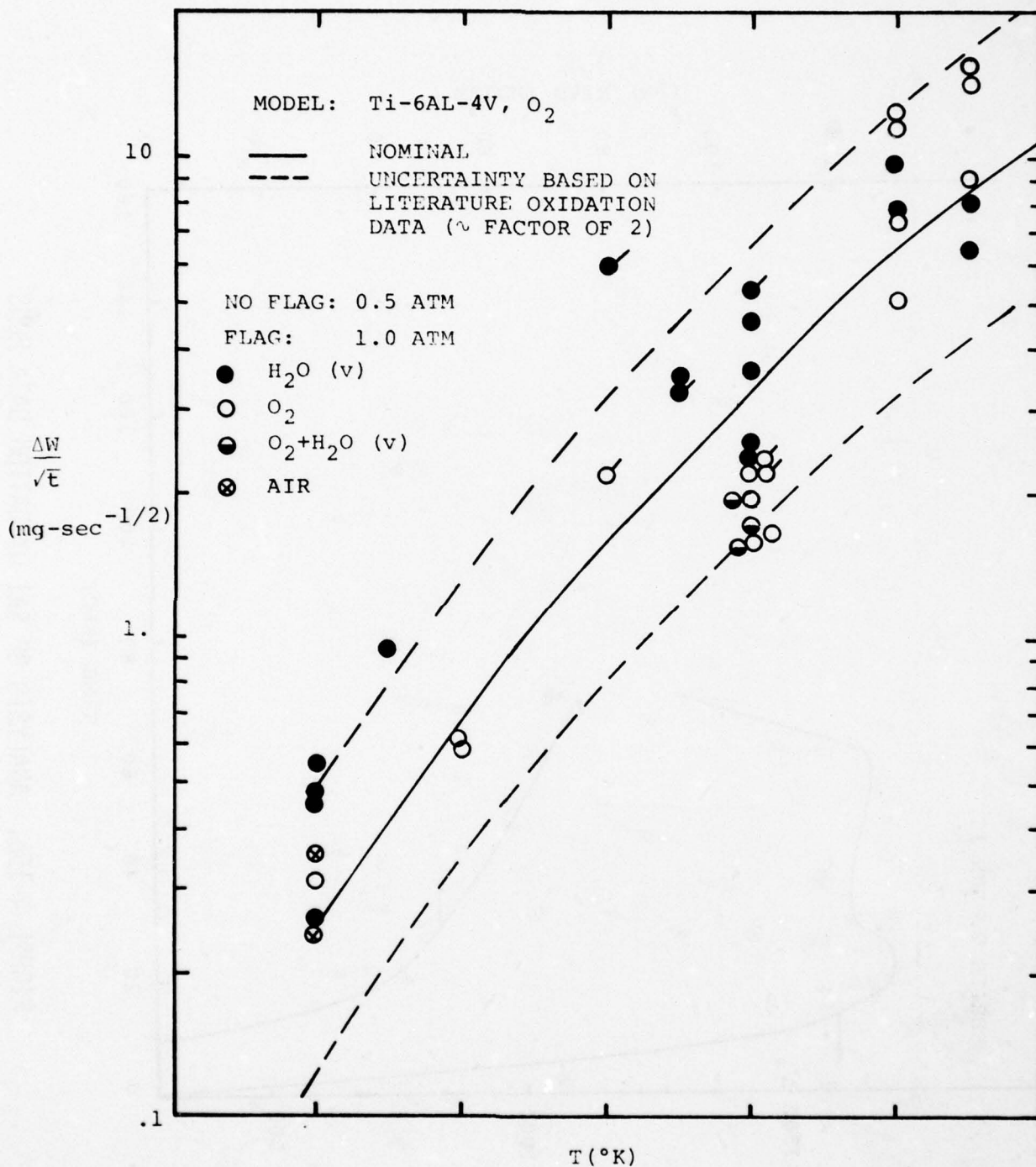
FIGURE 4-16. COMPARISON OF EXPERIMENTAL AND ANALYTICAL TITANIUM
OXIDATION RESULTS
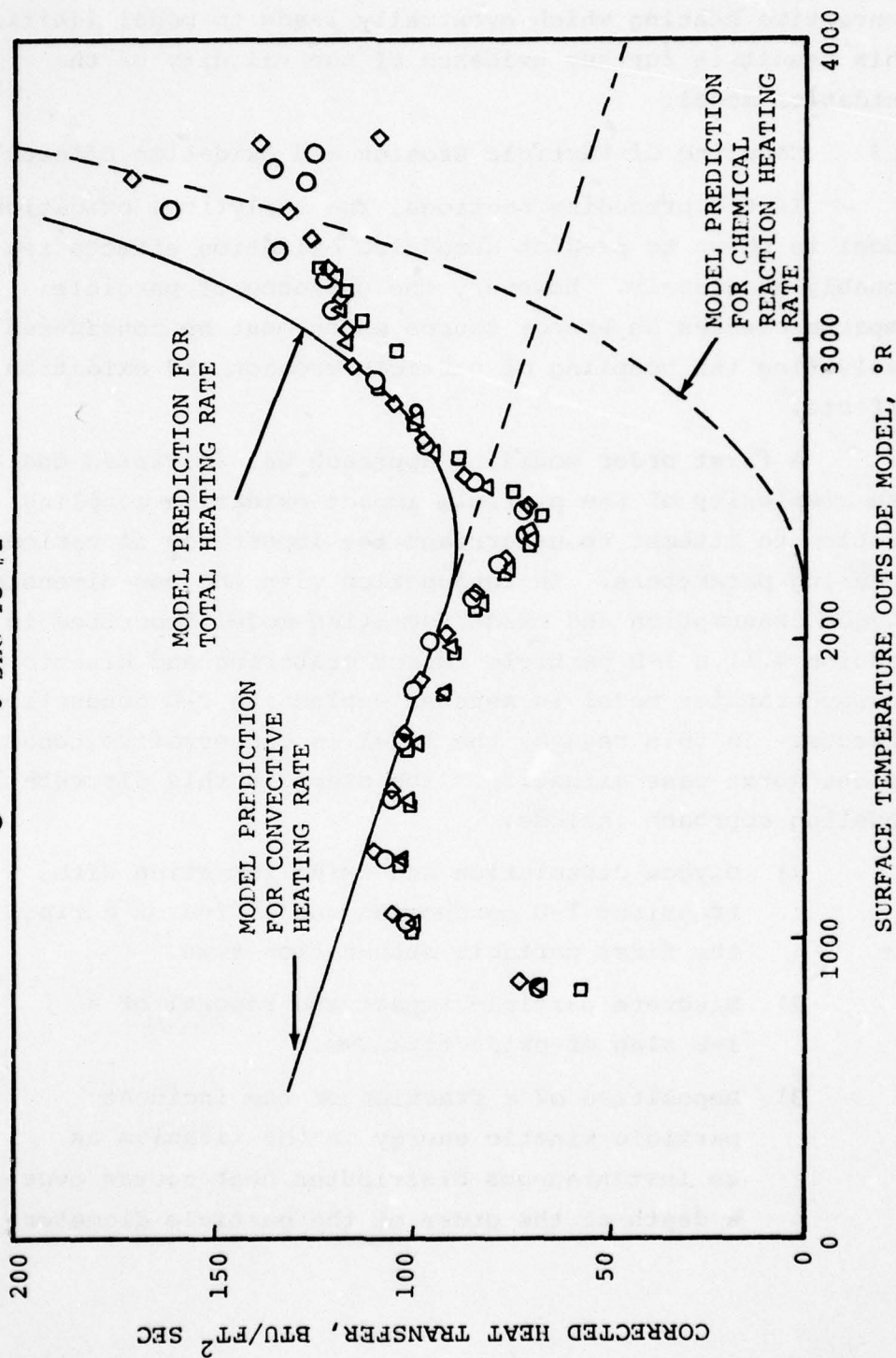
FIGURE 4-17. COMPARISON OF MODEL WITH EXPERIMENT FOR
RUN 7, MODEL TI-22, CLEAR AIR

occurs until 2200°R where surface oxidation heating becomes evident. Above 3000°R, the chemistry effect exceeds the convective heating which eventually leads to model ignition. This result is further evidence of the validity of the oxidation model.

4.3   Coupling of Particle Erosion and Oxidation Effects

In the preceding sections, the analytical oxidation model is shown to predict uncoupled oxidation effects reasonably accurately. However, the presence of particle impacts creates an energy source which must be considered in evaluating the coupling of particle erosion and oxidation effects.

A first order modeling approach was initiated due to the complexity of the particle impact-oxidation coupling problem to attempt to understand the importance of various modeling parameters. In conjunction with the one-dimensional oxygen consumption and oxide formation model described in Section 4.1, a 1-D particle impact cratering and kinetic energy transfer model is assumed neglecting 2-D conduction effects. In this regard, the model is conservative tending to the worst case situation. The steps in this discrete 1-D modeling approach include:

1)   Oxygen dissolution and oxide formation with transient 1-D conduction and diffusion during the first particle obscuration time.

2)   Discrete particle impact and removal of a 1-D slab of oxide/titanium.

3)   Deposition of a fraction of the incident particle kinetic energy in the titanium as an instantaneous distributed heat source over a depth of the order of the particle diameter.

4) Transient 1-D conduction and oxygen diffusion
with oxide re-formation over the next particle
obscuration time.

This discrete modeling approach results in local
crater hot spots due to kinetic energy deposition followed
by thermal diffusion (and thus crater cooling) over the time
between impacts. When the bulk temperature reaches a cri-
tical level, a subsequent impact causes a local ignition due
to the high local crater temperature and thus chemical heat
release locally. During this latter phase, the solid phase
oxidation and dissolution process becomes so large as to be
gas phase diffusion-limited. Thus, the boundary layer
transfer processes also become coupled to the overall solid
phase oxidation process.

It must be emphasized that the model presented herein
for this highly coupled particle erosion/oxidation ignition
process is intended to identify the key features involved.
In this respect, a number of adjustable parameters have been
introduced relating to the details of the particle kinetic
energy deposition process and to the gas phase diffusion
limited oxidation rates.

The key parameters in this modeling include:

$\rho_{p\infty}$ ≡ particle mass density

d_p ≡ particle diameter

V_p ≡ particle velocity

δ ≡ titanium thickness

Q_{cw} ≡ cold wall convective heat transfer rate

H_r ≡ BL recovery ethalpy

α_H ≡ depth of kinetic energy deposition as
fraction of d_p

TABLE 4-4. PARAMETERS FOR IMPACT-OXIDATION CALCULATION

Case	$\rho_{p\infty}$ (g/cc)	d_p (mm)	V_p (ft/sec)	δ (in.)	Q_{cw_2} (Btu/ft^2-sec)	H_r (Btu/lb)	α_H --	η --	$\dot{m}_{O_2}$
1	10^{-6}	.1	6000	.1	100	500	1	1	1,2
2	10^{-7}	.1	6000	.1	100	500	1	1	1,2
3	10^{-6}	1	6000	.1	100	500	1	1	1,2
4	10^{-6}	1	6000	.2	100	500	1	1	1,2
5	10^{-6}	1	6000	.5	100	500	1	1	1,2

η $\equiv$ fraction of particle kinetic energy transferred to thermal energy

$\dot{m}_{O_2}$ $\equiv$ augmented BL oxygen mass flux normalized by unaugmented value

Table 4-4 on the preceding page illustrates the representative values chosen for this parametric study. The results of the parametric calculations are shown in Figure 4-17. No local hot spot ignition is predicted except for case 3 with 1mm particles, 0.1 in. thick titanium, and an augmented BL oxygen mass flux by a factor of 2. For unaugmented mass flux, the problem is gas phase diffusion controlled which prevents an ignition in this case. Although case 3 predicts, qualitatively, ignition for larger particles, cases 4 and 5 illustrate that this can be alleviated using thicker titanium material. These results seem to indicate the importance of the gas phase oxygen mass flux diffusion limitations in preventing ignition at higher temperatures. The results also indicate an increased concern for ignition for higher dust densities and particle sizes, but ignition was not predicted for conditions of interest below approximately 2000°F bulk temperatures which still appears to be a reasonable design criteria.

FIGURE 4-18A. TITANIUM RESPONSE TO PARTICLE IMPACT-OXIDATION

FIGURE 4-18A. TITANIUM RESPONSE TO PARTICLE IMPACT-OXIDATION

$\rho_{p\infty} = 10^{-7}$ g/cc

$d_p = .1$mm

$\delta = 0.1''$

$\dot{m}_{O_2} = 1, 2$
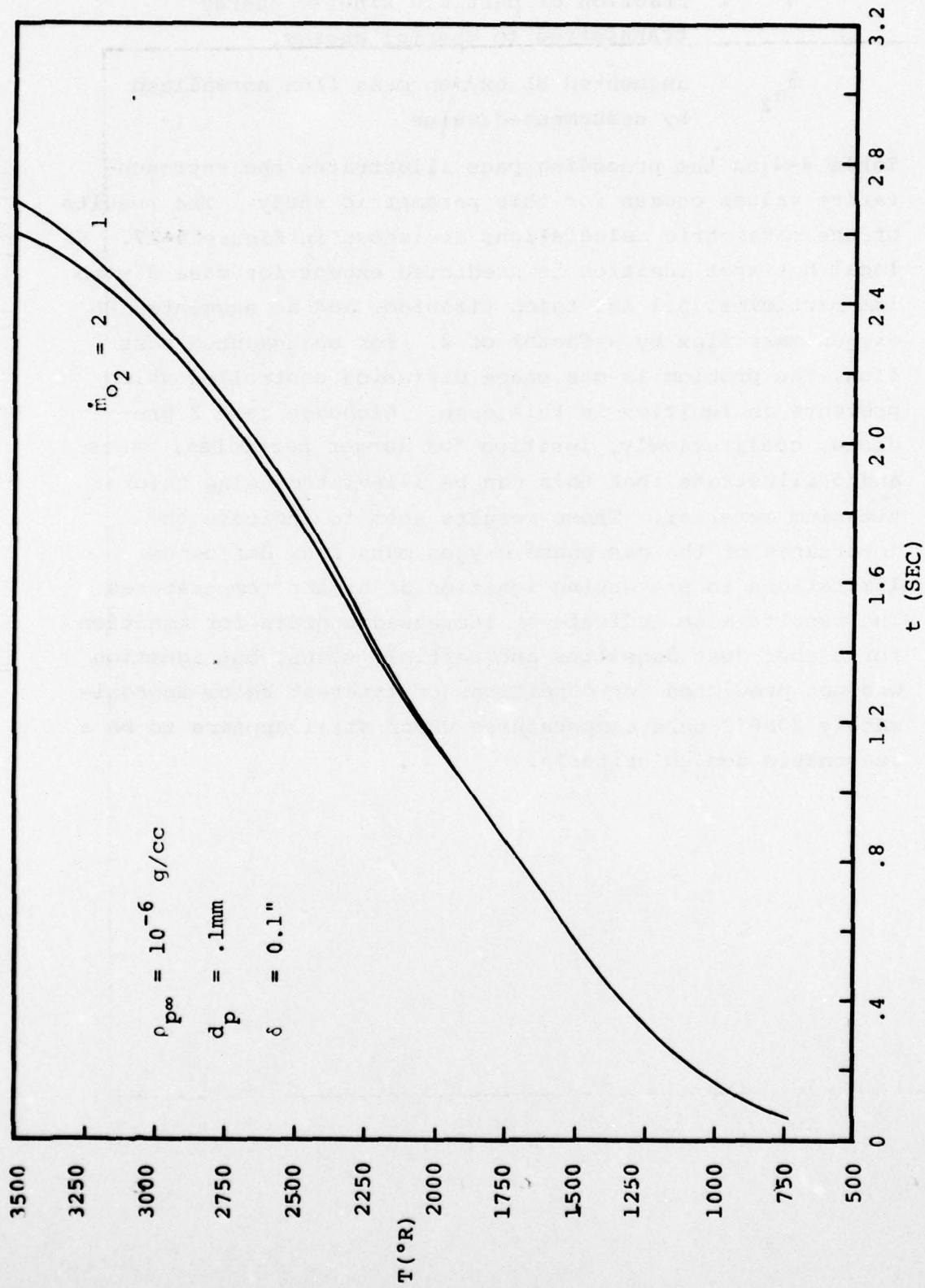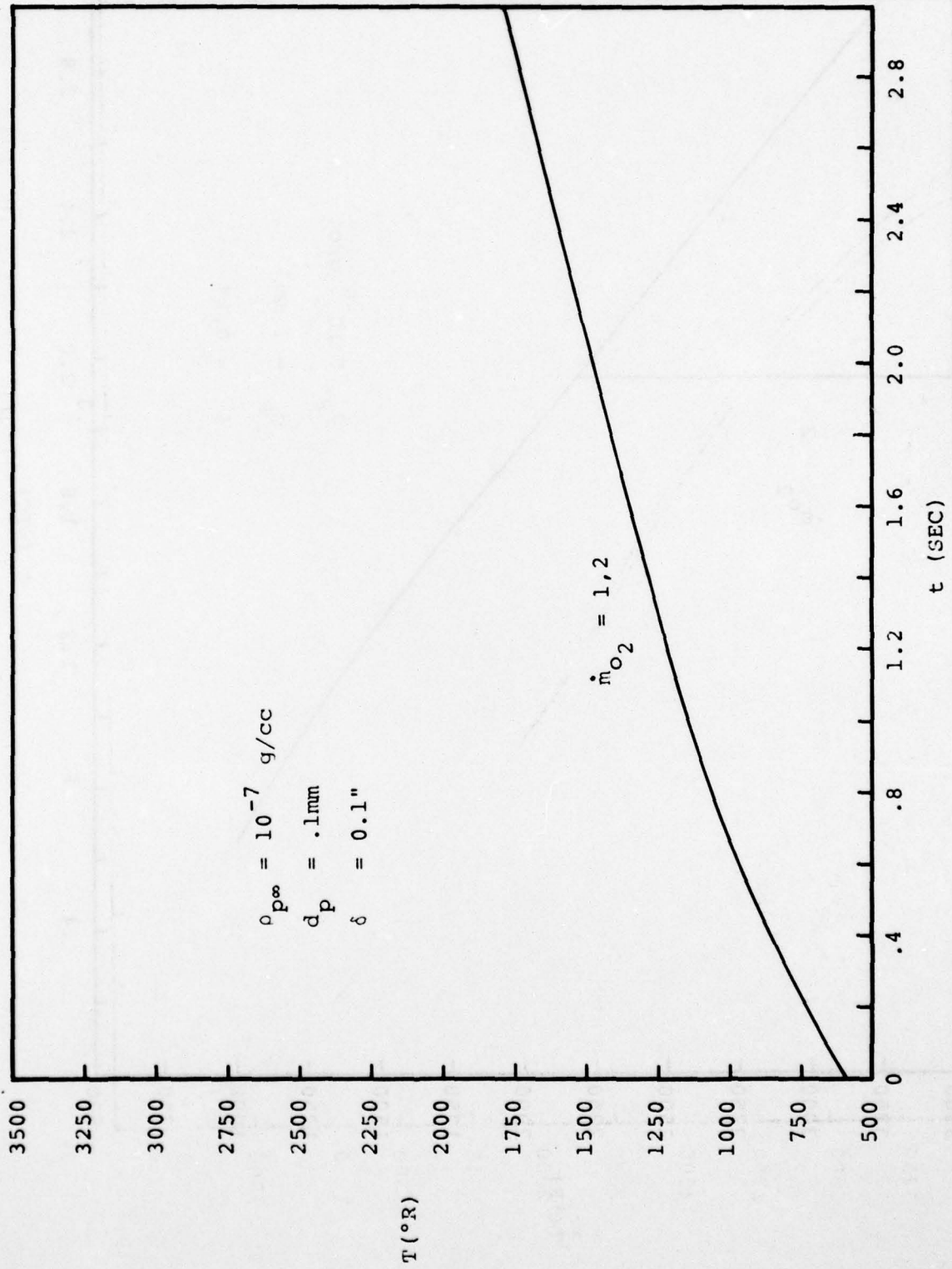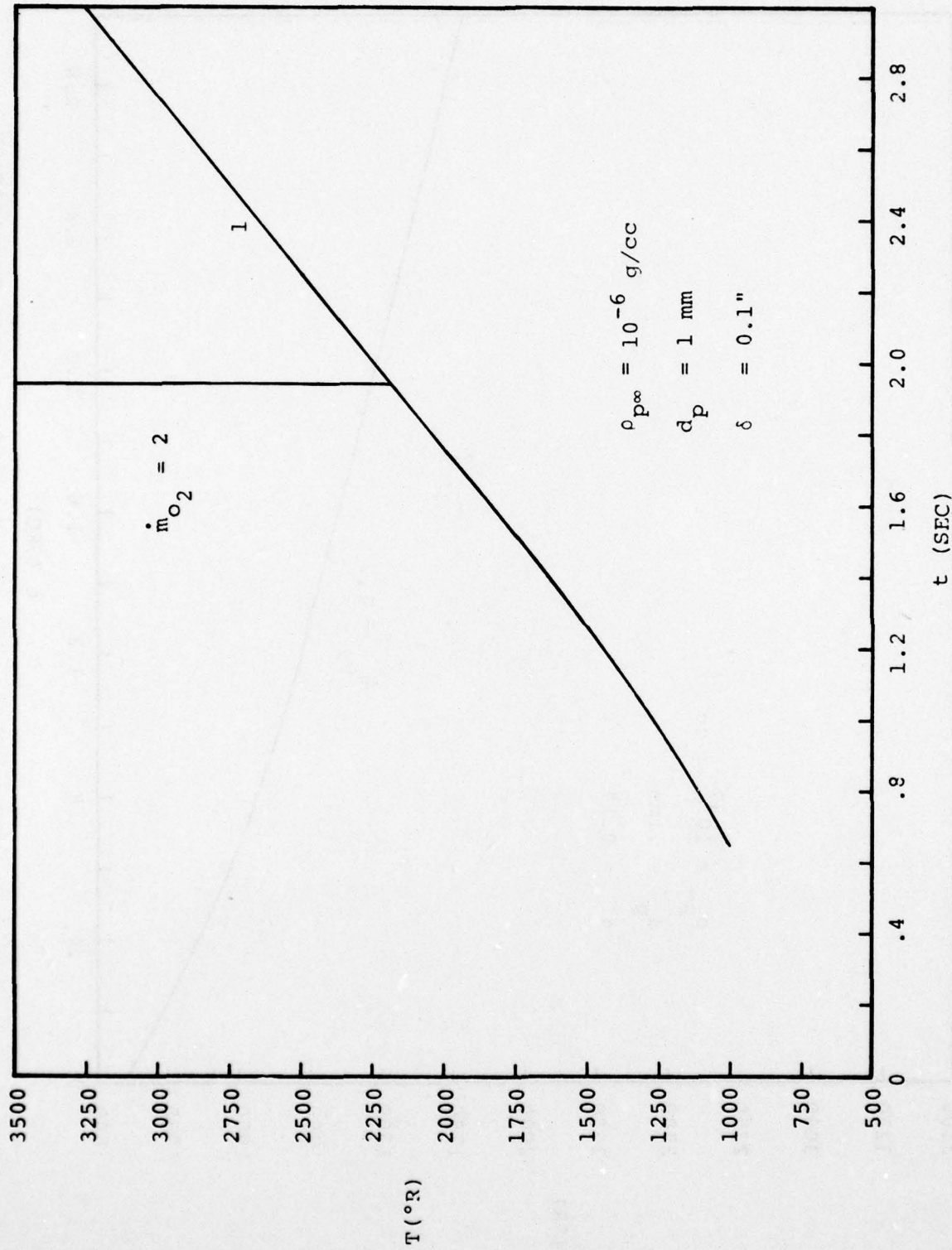
FIGURE 4-18c. TITANIUM RESPONSE TO PARTICLE IMPACT-OXIDATION
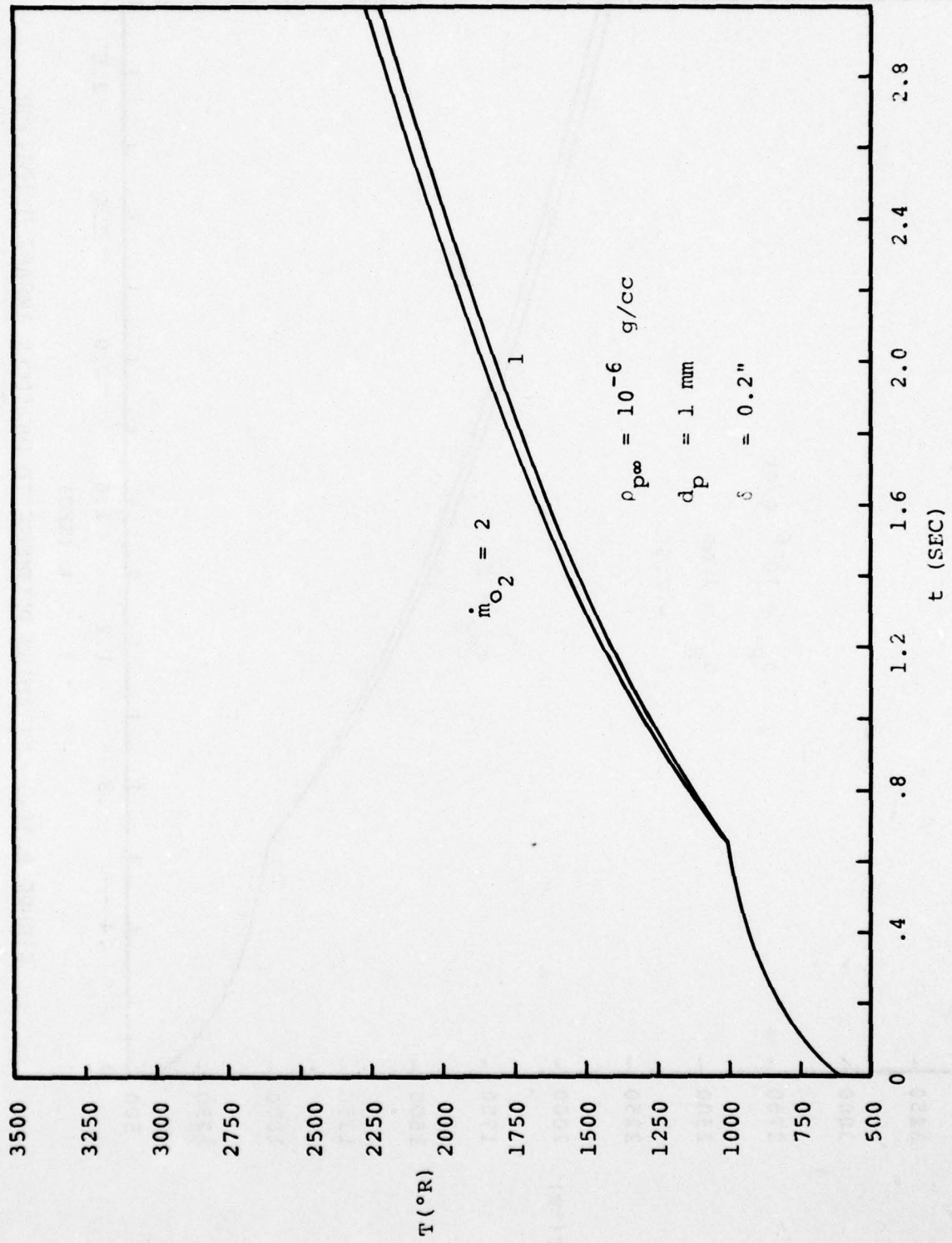
FIGURE 4-18D. TITANIUM RESPONSE TO PARTICLE IMPACT-OXIDATION

$\rho_{p\infty} = 10^{-6}$ g/cc

$d_p = 1$ mm

$\delta = 0.2"$

$\dot{m}_{O_2} = 2$

1
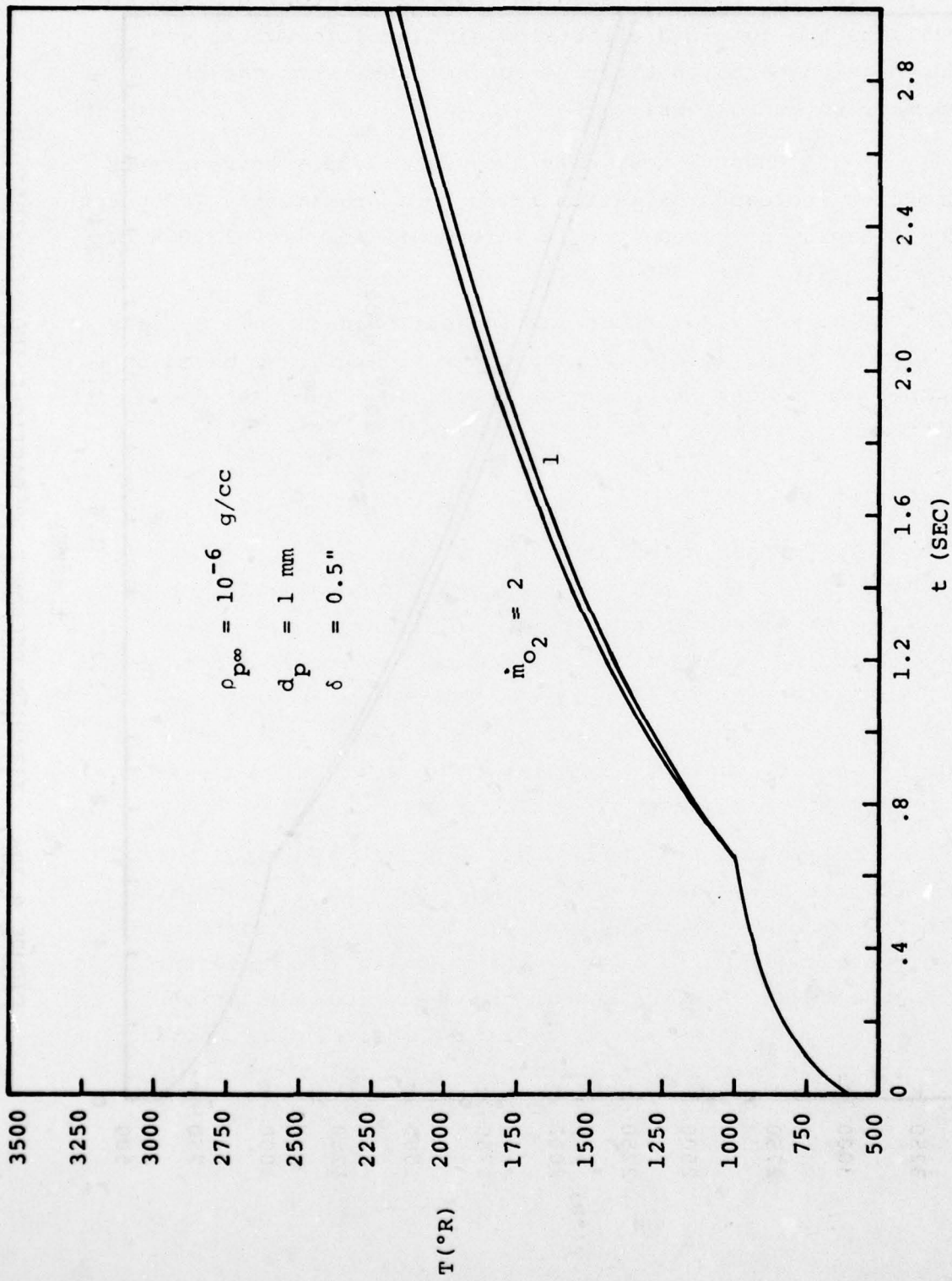
FIGURE 4-18e. TITANIUM RESPONSE TO PARTICLE IMPACT-OXIDATION

$\rho_{p\infty} = 10^{-6}$ g/cc

$d_p = 1$ mm

$\delta = 0.5$"

$\dot{m}_{O_2} = 2$

$T(°R)$

t (SEC)

5.0 CONCLUSIONS AND RECOMMENDATIONS

The conclusions based on this exploratory program to evaluate the combined effects of simulated ice/water and dust environments on titanium surface chemistry can be summarized as follows:

(1) Phase I test data show water vapor environments produced increased oxidation rates by approximately 100 percent for titanium compared to O_2 environments for 1200-1500°K but similar rates for 1700°K.

Analytical calculations suggest changes in H_2O vapor oxidation rates with temperature may be explained based on competing effects of diffusion coefficient (increased H_2 diffusion coefficient with temperature in titanium) and solubility (decreased H_2 solubility with increasing temperature).

(2) Phase I test data shows apparent pressure effect on oxidation rate. Analytical modeling where oxidation is solid-phase diffusion-controlled contradicts this experimental result. Assessment of literature data also contradicts this experimental result. The possibility of gas-phase rate-limiting processes in the Phase I test results may be an explanation. However, the overall evidence from the literature suggests <u>no</u> pressure effect.

(3) Phase II combined H_2O and dust data in the AEDC DET suggest a dominance of the heat absorbed in vaporizing the H_2O over any heat released due to surface oxidation. The overall effect is a <u>net</u> cooling due to the presence of condensed H_2O. Application of the analytical oxidation model to the DET test data shows good agreement predicting the on-set of significant oxidation heat release at approximately 2000°F with ignition occurring at temperatures in excess of 2500°F.

(4)   Phase III tests comparing ice and glass single impacts on titanium in oxidizing environments showed no ignition for a bulk temperature of $1700^{\circ}F$ ($\sim1200^{\circ}K$). The ice produced a smaller crater than the glass, but similar oxide coating spallation.

The overall conclusion from this exploratory program is that nuclear cloud ice/water will not significantly affect titanium oxidation response. Design criteria developed from extensive dust environment studies are still valid. No ignition is expected if titanium bulk temperatures remain below approximately 2000°F. Ignition can be expected above approximately 2500°F.

6.0   REFERENCES

1.   Patton, J. B., et al., "SAMSO Material Evaluation, Block I," AEDC Letter Report Project PE 0265, April 1972.

2.   Dunbar, L. E., et al., "Minuteman Hot Structures Heating Augmentation Study - Coupled Effects Test and Analyses," SAI-73-539-LA, July 1973.

3.   Dunbar, L. E., et al., "Minuteman Hot Structure Heating Augmentation Study - Volume I - Mechanisms and Analyses," SAMSO TR-73-272, August 1973.

4.   Dunbar, L. E., et al., "Minuteman Hot Structure Heating Augmentation Study - Volume II - Coupled Effects Modeling," SAMSO TR-73-272, August 1973.

5.   Dunbar, L. E., et al., "Heating Augmentation in Erosion Hypersonic Environments," AIAA Journal, Vol. 13, No. 7, July 1975.

6.   Lewis, H. I., et al., "Description and Calibration Results of the AEDC Dust Erosion Tunnel," AEDC-TR-73-74, May 1973.

7.   Lewis, H. F., "DNA Titanium Dust/Water Erosion Test," AEDC-DR-77-19, 11 March 1977.

8.   Hauffe, K., "Oxidation of Metals," Plenum Press, N.Y. 1965.

9.   Kofstad, P., "High-Temperature Oxidation of Metals," J. Wiley, N.Y., 1966.

10. Wolf, J., "Exploratory Development on Oxidation Behavior of Titanium Alloys Under High Heating Rates," Technical Report AFML-TR-74-265, April 1975.

11. Jost, W., "Diffusion in Solids, Liquids and Gases," Academic Press, N.Y., 1960.

12. Wallwork, G. R., W. W. Smeltzer and C. J. Rosa, Acta Metallurgica, 12, 409, (1964).

13. Rosa, C. J., J. Less-Common Metals, 16, 173, (1968).

14. Kofstad, P., P. B. Anderson, and O. J. Krudtaa, J. Less-Common Metals, 3, 89, (1961).

15. Shamblen, C. E., and T. K. Redden, "Air Contamination and Embrittlement of Titanium Alloys," in the Science and Technology of Titanium, ed., R. I. Jafee and N. E. Promisel, Pergamon Press, 1966.

16. Rosa, C. J., Metallurgical Trans. 1, 2517, (1970).

17. Roe, W. P., H. R. Palmer and W. R. Opie, Trans. ASM, 52, 191 (1960).

18. Reuyakin, A. V., Izu. Akad, Nauk Met i Tupliuo, 113 (1961).

19. Wasilewski, R. J., and G. L. Kehl, J. Inst, Metals, 83, 94 (1954).

20. "Minuteman Hot Structures Heating Augmentation Study, Final Summary Report," Report No. 14504-6151-RO-00, TRW Systems Group, October 1972.

21. Stringer, J. Acta Metallurgica, 8, 758 (1960).

22. Jenkins, A. E., J. Inst. Metals, 84, 1 (1955-56).

23. Davies, M. H., and C. E. Birchenall, J. Metals, 3, 877 (1951).

24. Hurlen, T., J. Inst. Metals, 89, 128 (1900-61).

25. Svehla, R. A., "Thermodynamic and Transport Properties for the Hydrogen-Oxygen System," NASA SP-3011 (1964).

26. Löhberg, K. and H. Schleicher, A. Phy. Chem. N.F., 15, 23 (1958).

27. Lutschkin, G. P., and G. G. Jljin, Fisiha Metallow i Metallowedenije 2, 1956, 521.

28. Lainer, D. I., A. S. Bai, and M. I. Tsypin, Fiz. Metal, i Metalloved 16 (2), 225 (1963).

29. Waisman, J. L., G. Sines, and L. B. Robinson, "Diffusion of Hydrogen in Titanium Alloys Due to Composition, Temperature and Stress Gradients," Metallurgical Trans., 4, 291-302 (1973).

30. Wasilewski, R. J., and G. L. Kehl, Metallwgica, 50, 225-30 (1954).

31. Skinner, G., H. L. Johnston, and C. Beckett, "Titanium and Its Compounds," Herrick L. Johnston Enterprises, Columbus, Ohio, 1954.

32. McQuillan, A. D., and M. K. McQuillan, "Titanium"
     Butterworths, London, 1956.

33. Gulbransen, E. A., and K. F. Andrew, Rev. Metall,
     15, 101 (1954).

34. Wolf, J. S., D. D. Moyle, A. B. Pruitt, and J. H.
     Bader, "Anisothermal Oxidation of Titanium: Initial
     Reactivity and Ignition," presented at the 150th
     meeting of the Electrochemical Society, Las Vegas,
     Nevada, 19th October 1976.

35. Evans, U. R., "The Corrosion and Oxidation of Metals,"
     p. 834, Edward Arnold Ltd., London, 1960.

DISTRIBUTION LIST

DEPARTMENT OF DEFENSE

Director
Defense Advanced Rsch. Proj. Agency
    ATTN: Strategic Tech. Office

Defense Documentation Center
Cameron Station
12 cy ATTN: TC

Director
Defense Intelligence Agency
    ATTN: DI-7D
    ATTN: DT-1C, Nuc. Eng. Branch
    ATTN: DT-2, Wpns. & Sys. Div.

Director
Defense Nuclear Agency
    ATTN: SPSS
    ATTN: SPTD
    ATTN: STSP
    ATTN: SPAS
    ATTN: DDST
    ATTN: TISI, Archives
 3 cy ATTN: TITL, Tech. Library

Under Secretary of Def. for Rsch. & Engrg.
Department of Defense
    ATTN: AD/ET, J. Persh
    ATTN: S&SS (OS)

Commander, Field Command
Defense Nuclear Agency
    ATTN: FCTMD
    ATTN: FCPR
    ATTN: FCTMOF
    ATTN: FCTMOT

Director
Joint Strat. Tgt. Planning Staff, JCS
    ATTN: JLTW-2
    ATTN: JPTM

Chief
Livermore Division, Field Command, DNA
Lawrence Livermore Laboratory
    ATTN: FCPRL

Studies Analysis and Gaming Agency
    ATTN: SDEB

DEPARTMENT OF THE ARMY

Director
BMD Advanced Tech. Ctr.
Huntsville Office
    ATTN: Marcus Whitfield
    ATTN: ATC-T, Melvin T. Capps

Program Manager
BMD Program Office
    ATTN: DACS-BMZ-D, Julian Davidson
    ATTN: DACS-BMZ
    ATTN: DACS-BMT, Clifford E. McLain
    ATTN: DACS-BMT, John Shea

DEPARTMENT OF THE ARMY (Continued)

Commander
BMD System Command
    ATTN: BDMSC-TEN, Noah J. Hurst

Dep. Chief of Staff for Rsch. Dev. & Acq.
Department of the Army
    ATTN: NCB Division

Commander
Harry Diamond Laboratories
    ATTN: DELHD-NP

Commander
Picatinny Arsenal
    ATTN: Al Loeb
    ATTN: Louis Avrami, SARPA-FR-E
    ATTN: Henry Opat, SMUPA-MD
    ATTN: Donald Miller, SARPA-ND-C-T

Director
TRASANA
    ATTN: R. E. Dekinder, Jr.

Director
U.S. Army Ballistic Research Labs.
    ATTN: DRXRD-BVL, William J. Schuman, Jr.
    ATTN: DRXBR-X, Julius J. Meszaros
    ATTN: Robert E. Eichelberger
    ATTN: Richard Vitali
    ATTN: DRXBR-TB, J. T. Frasier
    ATTN: DRDAR-BLE, J. H. Keefer

Commander
U.S. Army Mat. & Mechanics Rsch. Ctr.
    ATTN: DRXMR-HH, John F. Dignam

Commander
U.S. Army Materiel Dev. & Readiness Cmd.
    ATTN: DRCDE-D, Lawrence Flynn

Commander
U.S. Army Missile Command
    ATTN: DRS-RKP, W. B. Thomas
    ATTN: DRSMI-RRR, Bud Gibson
    ATTN: DRSMI-XS, Chief Scientist

Commander
U.S. Army Nuclear Agency
    ATTN: CDC-NVA
    ATTN: ATCA-NAW
    ATTN: MONA-SA
    ATTN: MONA-WE

DEPARTMENT OF THE NAVY

Chief of Naval Operations
Navy Department
    ATTN: Code 604C3, Robert Piacesi

Chief of Naval Research
Navy Department
    ATTN: Code 464, Thomas P. Quinn

DEPARTMENT OF THE NAVY (Continued)

Director
Naval Research Laboratory
    ATTN: Gerald Cooperstein, Code 7770
    ATTN: Mario A. Persechino, Code 5180
    ATTN: Code 2600, Tech. Lib.

Commander
Naval Sea Systems Command
Navy Department
    ATTN: 0333A, Marlin A. Kinna

Officer-In-Charge
Naval Surface Weapons Center
    ATTN: Code WA07, W. Carson Lyons
    ATTN: Code WA501, Navy Nuc. Prgms. Off.
    ATTN: Code WR10, Joseph Petes

Commanding Officer
Naval Weapons Evaluation Facility
    ATTN: Lawrence R. Oliver

Director
Strategic Systems Project Office
Navy Department
    ATTN: NSP-272

DEPARTMENT OF THE AIR FORCE

Commandant
AF Flight Dynamics Laboratory, AFSC
    ATTN: FXG

AF Geophysics Laboratory, AFSC
    ATTN: Chan Touart

AF Materials Laboratory, AFSC
    ATTN: MBC, Donald L. Schmidt
    ATTN: MBE, George F. Schmitt

AF Weapons Laboratory, AFSC
    ATTN: SUL

Headquarters
Air Force Systems Command
    ATTN: SOSS
    ATTN: XRTO

Commander
Arnold Engineering Development Center
    ATTN: XOA

Commander
ASD
 4 cy ATTN: EWFS, D. Ward

Commander
Foreign Technology Division, AFSC
    ATTN: TDFBD, J. D. Pumphrey

Hq. USAF/XO
    ATTN: XOOSS

SAMSO/DY
    ATTN: DYS

SAMSO/MN
    ATTN: MNNR
    ATTN: MNNH

DEPARTMENT OF THE AIR FORCE (Continued)

SAMSO/RS
    ATTN: RSSE
    ATTN: RST
    ATTN: RSS

Commander in Chief
Strategic Air Command
    ATTN: DOXT
    ATTN: XOBM
    ATTN: XPQM
    ATTN: XPFS

DEPARTMENT OF ENERGY

Division of Military Application
    ATTN: Doc. Con. for Res. & Dev. Branch

University of California
Lawrence Livermore Laboratory
    ATTN: Joseph E. Keller, Jr., L-125
    ATTN: G. Staihle, L-24
    ATTN: C. Joseph Taylor, L-92
    ATTN: Joseph B. Knox, L-216

Los Alamos Scientific Laboratory
    ATTN: Doc. Con for R. S. Thurston
    ATTN: Doc. Con. for R. Dingus
    ATTN: Doc. Con. for J. W. Taylor
    ATTN: Doc. Con. for John McQueen
    ATTN: Doc. Con. for Robert Skaggs

Sandia Laboratories
Livermore Laboratory
    ATTN: Technical Library
    ATTN: Doc. Con. for 8131, H. F. Norris, Jr.

Sandia Laboratories
    ATTN: Doc. Con. for Thomas B. Cook
    ATTN: Doc. Con. for Albert Chabai
    ATTN: Doc. Con. for M. Cowen
    ATTN: Doc. Con. R. R. Boade

DEPARTMENT OF DEFENSE CONTRACTORS

Acurex Corporation
    ATTN: C. Nardo

Aerospace Corporation
    ATTN: D. Glenn
    ATTN: W. Barry
    ATTN: Robert L. Strickler
    ATTN: R. Mortensen

Analytic Services, Inc.
    ATTN: Jack Selig

Avco Research & Systems Group
    ATTN: George Weber, J230
    ATTN: William Broding
    ATTN: Doc. Control

Battelle Memorial Institute
    ATTN: Technical Library
    ATTN: Merwyn R. Vanderlind
    ATTN: F. Unger

The Boeing Company
    ATTN: Brian Lempriere
    ATTN: Robert Holmes

California Research & Technology, Inc.
    ATTN: M. Rosenblatt

University of Dayton
    ATTN: Hallock F. Swift
    ATTN: D. Gerdiman

Effects Technology, Inc.
    ATTN: Richard Parise
    ATTN: Robert Wengler

General Electric Company
Space Division
    ATTN: Carl Anderson
    ATTN: Daniel Edelman
    ATTN: Phillip Cline

General Electric Company
TEMPO-Center for Advanced Studies
    ATTN: DASIAC

Institute for Defense Analyses
    ATTN: IDA Librarian, Ruth S. Smith
    ATTN: Joel Bengston

Kaman Sciences Corporation
    ATTN: Thomas Meagher

Lockheed Missiles & Space Co., Inc.
    ATTN: R. Walz, Dept 81-14

Lockheed Missiles & Space Co.
    ATTN: T. R. Fortune

Lockheed Missiles & Space Co., Inc.
    ATTN: F. G. Borgardt

Martin Marietta Aerospace
Orlando Division
    ATTN: Gene Aiello

McDonnell Douglas Corporation
    ATTN: L. Cohen

National Academy of Sciences
National Materials Advisory Board
    ATTN: Donald G. Groves

Pacific-Sierra Research Corp.
    ATTN: Gary Lang

Physics International Company
    ATTN: Doc. Con. for James Shea

Prototype Development Associates, Inc.
    ATTN: M. Sherman
    ATTN: John McDonald

R&D Associates
    ATTN: F. A. Field
    ATTN: Cyrus P. Knowles

Science Applications, Inc.
    ATTN: John Warner
    ATTN: Dwane Hove

Science Applications, Inc.
    ATTN: B. Blows
    ATTN: Lyle Dunbar
    ATTN: G. Burghart
    ATTN: R. M. Clever
    ATTN: A. F. Mills

Science Applications, Inc.
    ATTN: J. McGohan
    ATTN: William R. Seebaugh
    ATTN: William M. Layson

SRI International
    ATTN: George R. Abrahamson
    ATTN: Herbert E. Lindberg
    ATTN: Donald Curran
    ATTN: D. L. Huestis
    ATTN: Philip J. Dolan

Systems, Science and Software, Inc.
    ATTN: G. A. Gurtman

Terra Tek, Inc.
    ATTN: Sidney Green

TRW Defense & Space Sys. Group
    ATTN: W. W. Wood
    ATTN: D. H. Baer, R1-2136
    ATTN: A. Zimmerman
    ATTN: Peter Brandt, E1-2006
    ATTN: R. Myer

TRW Defense & Space Sys. Group
San Bernardino Operations
    ATTN: L. Berger
    ATTN: William Polich